Arch Comput Methods Eng (2007) 14: 47–91
DOI 10.1007/s11831-006-9001-3

Computational Modelling of Diarthrodial Joints. Physiological, Pathological and Pos-Surgery Simulations

E. Peña · A. Pérez del Palomar · B. Calvo · M.A. Martínez · M. Doblaré

Received: 1 March 2006 / Accepted: 1 March 2006 / Published online: 8 March 2007

Abstract This paper provides a critical review of past and current techniques for the computational modelling of diarthrodial joints. The objective of the paper is to describe strategies for addressing the computational modelling of joint mechanics using the finite element (FE) method, differentiating between geometry, constitutive modelling of the components, computational aspects and applications. The structure and function of the main components of the joints are reviewed, with emphasis on the relationship of tissue microstructure with its continuum mechanical behavior. Applications to two diarthrodial joints (human knee and temporomandibular joint) in physiological, pathological and pos-surgery situations are presented and discussed. The paper concludes with a discussion of future research directions.

1 Introduction

Biomechanics is defined as the development, extension and application of mechanics with the purposes of a better understanding of Physiology and Pathophysiology and helping in the diagnosis and treatment of disease and injury. That is, the overall goal of Biomechanics is, and must remain, the general improvement of human condition [92].

In particular, a proper understanding of joints biomechanics is essential to improve the prevention and treatment of their disorders and injuries. Despite the many investigations developed in this field, the exact mechanical behavior of the different human joints and the causes of many of their injuries are not completely known yet. This is partially due to inherent limitations of experimental studies such as their high cost, difficulties associated with the obtention of accurate measures of strain and stress and, especially, the difficult and sometimes impossible reproduction of certain natural, pathological or degenerative situations. Computational models of diarthrodial joints provide therefore a powerful tool for the study of joint function, prosthesis design, and the effects of joint reconstruction. Computers models also provide a standardized framework for parameter studies, such as evaluation of clinical treatments, stress distributions for different geometries and kinematics, evaluation of surgical procedures, injury assessment, surgery planning and the effects of ageing, disease and drugs [201].

It is important to note that reliability of these models strongly depends on a precise geometrical reconstruction and on an accurate mathematical description of the behavior of the biological tissues involved, and their interactions with the surrounding environment.

The acquisition of an accurate geometry of the joint is a fundamental requirement for the construction of three-dimensional FE models. Both magnetic resonance imaging (MRI) and computerized tomography (CT) are used to acquire joint geometry. MRI provides detailed images of soft tissues in diarthrodial joints while CT provides excellent images of the bones around the joint [203]. Extraction of the geometry from CT or MRI data is performed by first identifying the boundary of the structure (process known as segmentation). For that purpose, it is still generally necessary to perform manual (or semi-automatic) segmentation of the boundaries, followed by a semiautomatic reconstruction of the 3D bodies involved. Usually, some additional manual

E. Peña · A. Pérez del Palomar · B. Calvo · M.A. Martínez · M. Doblaré (✉)
Group of Structural Mechanics and Materials Modeling, Aragón Institute of Engineering Research, University of Zaragoza, María de Luna, 3, 50018, Zaragoza, Spain
e-mail: mdoblare@unizar.es

edition is needed to remove underjoined image artifacts or non-interesting organs, to smooth surfaces or to separate different components wrongly joined, among other usual operations.

Once the geometrical model has been reconstructed from the 3D image dataset, it is necessary to generate the FE mesh. For accurate solutions, it is recommended the use of hexahedral elements (quadratic and linear tetrahedra are also very much used), although this is not always necessary. For example, some ligaments are very thin, being reasonable the use of shell elements. In many cases, when the interest is focussed on soft tissues, bones are modelled as rigid bodies due to their much higher stiffness (several orders of magnitude). In these cases, bone surfaces can be modelled using rigid shell elements. Usually, the high complexity of the geometries involved implies that the development of a specific finite element model takes a large amount of user time. Other alternative, although not much extended yet, is the family of numerical methods globally coined as meshless or mesh-free methods [39]. Their main characteristic is the no need of a mesh in the traditional sense. Instead, the connectivity between nodes is generated in a process transparent to the user, thus alleviating the burden associated to the mesh generation [40]. However, their computational cost is higher than the one of FEM.

Constitutive equations are used to describe the mechanical behavior of ideal materials through the establishment of the dependence of the stress on different variables, such as the deformation gradient, rate of deformation or temperature. In this paper, we emphasize that constitutive relations describe the behavior of a material under certain conditions of interest, but not the material itself. That is, although we would prefer an equation that describes the behavior of a specific material under every condition, we have generally to accept relations that hold only under specific conditions discarding or approximating important, but on the other hand marginal for the purposes of the study, aspects like for instance individual cell behavior. Five different theoretical frameworks have proved to be of considerable utility in continuum biomechanics of hard and soft tissues: finite elasticity, damage mechanics, viscoelasticity, mixture theory and growth and remodelling [92], this is, the adaptive evolution process, typical of living tissues, that consists on the modification of their internal architecture according to the specific mechanical and biological environments. Most of the available models characterize the relation between continuum behaviour and internal microstructure by means of macroscopic internal variables like the apparent density, fabric or other structural tensors.

The main characteristic of biological tissues is their high flexibility (they usually undergo large strains) and their nonlinear, anisotropic, inhomogeneous and viscoelastic behavior determined by the concentration and structural arrangement of their principal constituents: collagen, elastin and proteoglycans. Examples of connective tissues are bone (a special tissue partially mineralized), tendons, ligaments or cartilage, among many others. Numerous material models have been used to model them: hyperelastic [206], viscoelastic [160] and poroelastic [188] among others. In addition, biological tissues are usually exposed to a complex distribution of "in vivo" residual stresses as a consequence of the continuous growth, remodelling, damage and viscoelastic strains that they suffer along their whole life.

Finally, many soft tissues are quasi-incompressible. Failure to satisfy this assumption can result in a considerable drift of the numerical solution from the theoretical one. A single-field variational approach with the displacement **u** as the only field variable is often used together with the so-called penalty method, based on the simple idea of modeling an incompressible material as slightly compressible by using a large value of the bulk modulus. However, this method exhibits rather poor numerical performance due to the penalty sensitivity and ill-conditioning of the stiffness matrix. To eliminate these difficulties, multi-field variational principles as Lagrangian-multipliers, Augmented Lagrangian, Simo–Taylor–Pister or Hu–Washizu variational principles may be used [90].

Another important aspect in joint modelling is the evaluation of the constitutive parameters. Material coefficients may be based on subject-specific measurements or on population averages. In the former, uncertainty is related to inherent errors in experimental measurements and their extension to other individuals. In the latter, coefficients represent a population average, and thus, have some well-defined variance. In both cases, it is desirable to characterize the sensitivity of the numerical results to variations in the material coefficients [203].

During deformation, two or more bodies may contact. The analysis of contact using the FE method can be a very difficult, nonlinear problem. In a FE context, contact may be enforced as an additional nonlinear kinematic constraint. Contact implementation must be able to handle both static and dynamic situations, with and without frictional sliding. Three of the most common approaches for implementing contact in a FE context are the penalty method, the Lagrange multiplier method, and the Augmented Lagrangian method [212].

The comparison of model predictions to experimental measurements, or clinical evidences constitutes the validation process. There is no way to completely validate a model. Therefore, one must pose specific hypotheses about model predictions along with tolerable errors. Validation is the most challenging aspect of the FE modelling of joint mechanics, as it requires accurate experimental measurements

of quantities that are difficult to obtain. We can use experimental data available in the literature, but this is also insufficient in subject-specific joint models.

With all the above in mind, the objective of the paper is to describe strategies for addressing the computational modelling of joint mechanics using the finite element (FE) method, differentiating between geometry, constitutive modelling of the components, computational aspects and applications. The paper is organized as follows: Sect. 2 describes the basic structure, composition and constitutive models of the main hard and soft tissues that compose diarthroidal joints; Sect. 3 discusses technical aspects of the finite element formulation and finally, examples of physiological, pathological and pos-surgery simulations of knee and temporomandibular joints are presented in Sect. 4. Finally, in Sect. 5 some conclusions are summarized.

2 Constitutive Models for Joint Tissues

In this section, a revision of the constitutive models that have been developed for joint tissues is presented. Joint tissues can be divided in soft and hard tissues. In the following, a brief description of hard tissues model is presented, and a more detailed one is done for soft tissues. Apart from this, the muscle tissue has a special behaviour related to its capacity of natural contraction and this aspect will be described in a separate section. In addition, these tissues are usually exposed to a complex distribution of *in vivo* initial strains and this characteristic will be described in the last section. However, the composition of all of them is quite similar.

In general, joint tissues are mainly composed of specialized cells (chondrocytes, osteoblasts, ...) and extracellular matrix that includes interstitial fluid (water and electrolytes) and different proportions of the following components: fibers of collagen and elastin and ground substance.

Collagen is a fibrous protein [60]. It is a basic structural element for hard and soft tissues in animals. It gives mechanical integrity and strength. It is present in a variety of structural forms in different tissues and organs. The stiffness of the collagen network is highly influenced by the amount of cross-links among fibers. Collagen also has the ability to form covalent molecular cross-links with the ground substance matrix. These cross-links are responsible for the high stiffness and tensile strength of collagen and its resistance to chemical and enzymatic attack [195].

On the other hand, the behavior of elastin is responsible for a small part of a soft tissues's tensile resistance and its elastic recoverability. The insoluble protein elastin takes on a complex coiled arrangement when unstressed. When elastin is stressed, the coiled arrangement stretches into a more ordered configuration. Ligaments with a high elastin content have shown to be less stiff and to undergo larger strains before failure when compared to cartilage with a lower elastin content [60, 201].

Finally, the connective tissue surrounding the fibers is referred to as the ground substance matrix. This tissue is partly responsible for holding the fibers together. The composition of the ground substance varies with the tissue. The ground substance matrix is composed of proteoglycans, glycolipids, and fibroblasts and holds large amounts of water [60]. Proteoglycans have a very important role: the hydration of collagen. Water typically comprises 60 to 70% of the total weight of normal soft tissues. Water and proteoglycans provide lubrication. The interaction of water with the ground substance matrix and collagen is responsible for most of the time- and history-dependent viscoelastic behavior observed in soft tissues [60, 195].

2.1 Structure and Properties of Joint Tissues

2.1.1 Bone

Bone is a complex, living, constantly changing tissue. The architecture and composition of cancellous and cortical bone allow the skeleton to perform its essential mechanical functions. The bone matrix has an organic component, primarily type I collagen, which gives it tensile strength and an inorganic component, primarily hydroxyapatite, which gives it stiffness to compression. This tissue has different levels of porosity, a macroporosity that defines the trabeculae and a microporosity of the intrinsic solid bone tissue. Besides, specialized populations of bone cells form, maintain and remodel this matrix.

Bone tissue for instance has very interesting structural properties. While its compression strength is similar to that of steel, it is three times lighter and ten times more flexible, essentially due to its special heterogeneous microstructure. In addition, bone tissue is under permanent change in response to different signals such as external loads, hormonal influence, etc. This process of microstructural change is known as bone remodelling [36, 42, 95].

2.1.2 Tendons and Ligaments

Tendons and ligaments are soft tissues composed of closely packed, parallel collagen fiber bundles oriented to provide motion and stability to the musculoskeletal system. Under macroscopic examination, ground substance is observed in the interfibrillar spaces. Although ligaments are considered as a composite material consisting of a ground substance matrix reinforced by collagen and elastin, collagen is the primary component that resists the tensile stress in ligaments. Figure 1 illustrates the hierarchy proposed by Kastelic and Galeski [98] for the type I collagen in a rat tail tendon.

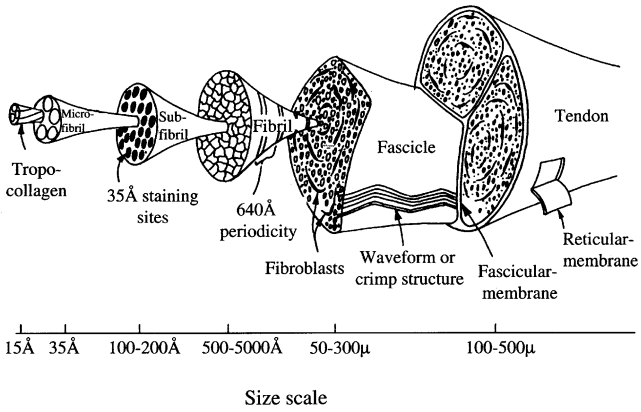

Fig. 1 Hierarchy of the structure of a tendon adapted from Kastelic and Galeski [98]

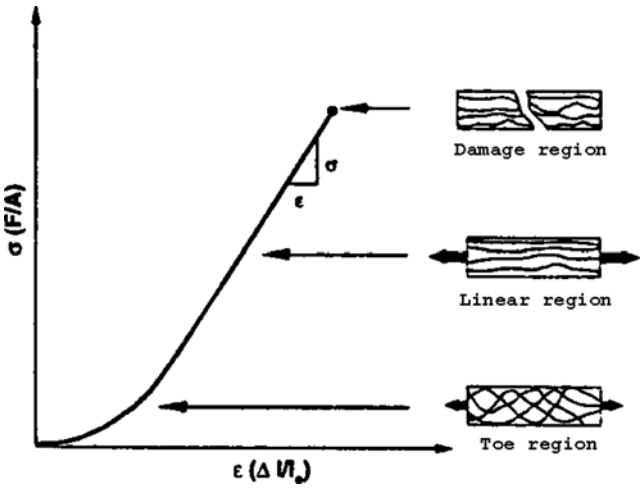

Fig. 2 Schematic diagram of a uniaxial tensile test where fibers orient in the direction of the load as it increases

The tensile modulus of the ligament depends on the collagen fibril density, fibril orientation and the amount of collagen cross-linking. When this tissue is tested in tension, the collagen fibrils are aligned and stretched along the axis of loading. For small deformations, when the tensile stress in the specimen is relatively small, a nonlinear toe-region is seen in the stress-strain curve, due to realignment of the collagen fibres, rather than stretching of these fibers. For larger deformations, and after realignment, the collagen fibrils are stretched and therefore generate a larger tensile stress due to the intrinsic stiffness of the collagen fibrils themselves. Due to this phenomenon, the tensile stiffness of ligaments is highly strain dependent (see Fig. 2).

2.1.3 Cartilage

Articular cartilage forms a thin tissue layer that lines the articulating ends of all diarthrodial joints in the body. The primary functions of these cartilage layers are to minimize contact stresses generated during joint loading and to contribute to lubricate the joint [133, 134]. A healthy joint is able to withstand the large forces associated with weight-bearing and joint motion over the lifetime of an individual.

Articular cartilage can be considered a composite, organic solid matrix that is saturated with water and mobile ions. The solid matrix consists of cartilage cells (chondrocytes) embedded in an extracellular matrix. The major components of the extracellular matrix are collagen molecules and negatively charged proteoglycans (PGs). The water phase of cartilage constitutes averages from 65 to 80% of the total weight for normal tissue and determines the behaviour of this tissue. This interstitial water is distributed non-uniformly with depth from the surface and is an important constituent in controlling many physical properties.

Collagen, on average, constitutes nearly 75% of the dry tissue weight. As it happens with water, the distribution of collagen is stratified throughout the depth. Collagen fibers do not offer significant resistance to pressure, but are stiff and strong in tension as mentioned for ligaments and tendons (Sect. 2.1.2). Hence, they provide resistance against swelling and tensile strains.

The response of the tissue to an applied load varies with time, giving rise to well-known viscoelastic behaviors as creep and stress relaxation. There are two distinct dissipative mechanisms in response to loading: (a) the frictional drag force of interstitial fluid flow through the porous-permeable solid matrix (i.e. the flow-dependent mechanism); and (b) the time-dependent deformations of the solid macromolecules (i.e. the flow-independent mechanism).

When the load is applied, the interstitial fluid flows outside the porous-permeable matrix. The load makes the solid matrix to compact, increasing the interstitial pressure and forcing the fluid to squeeze out of the matrix. The rate of fluid flow is controlled by the drag forces generated by the flux. In general, the load transmission between solid and fluid phases is related with the volume fraction of each phase. Besides, the rate of fluid exudation is related with the tissue's permeability. This variable decreases in a non linear form with the compressive load. This effect acts as a regulation mechanism, avoiding a fast exudation of the fluid and making possible that the cartilage can support more load.

2.1.4 Skeletal Muscle

Skeletal muscle makes up a major part of the animal body. It is the prime mover of animal locomotion and it is controlled by voluntary nerves. When stimulated, it can generate tension that produce a contracting mechanism [60]. The skeletal muscles have a complex structure with a well defined hierarchy which can be distinguished when observed at various levels of magnification. At the lowest level of magnification, it is observed that muscles are surrounded by a fibrous

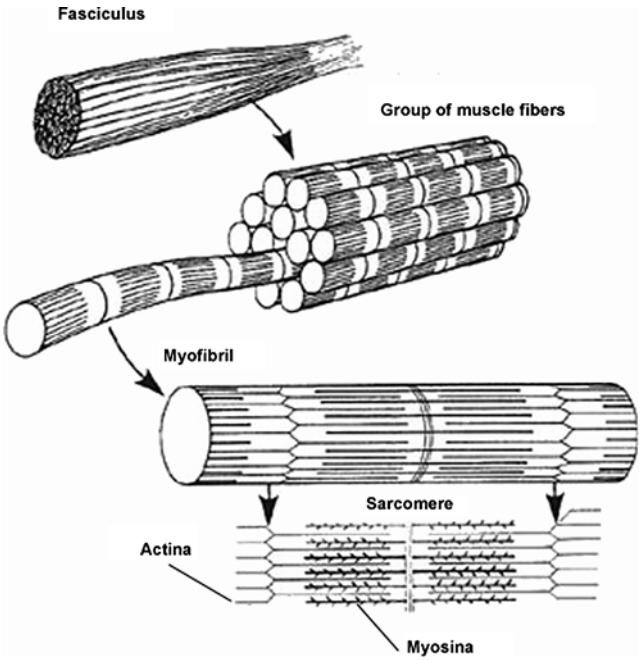

Fig. 3 Hierarchy of the structure of a muscle adapted from Fung [60]

connective tissue, the epimysium, and composed of many bundles, or fascicles, which are in turn encased in a dense connective tissue, the perimysium (Fig. 3).

Due to its special composition, skeletal muscle presents two different behaviors. As connective tissue, muscle presents a passive behavior similar to tendon and ligaments. In addition, a muscle can contract independently. This phenomenon is known as active behavior [79, 93]. A motor unit is composed of a neuron and the muscle fibers stimulated by it. In large muscles each motor unit may have 1000 to 2000 muscle fibers. The degree of activation of a muscle is a result of the number of activated (recruited) motor units. Note that the fibers of each motor unit are not contiguous but are dispersed throughout the muscle; thus, even if a single motor unit was stimulated, a large portion of the muscle would appear to contract [60].

2.2 Constitutive Models for Hard Tissues

Bone tissue, like most biological materials, has very interesting structural properties. This is essentially due to its heterogeneous microstructure, composed of an organic part (mainly collagen, which provides traction capacity) and a mineral part (which provides strength and stiffness under compression). Bone is an inhomogeneous, anisotropic, viscoelastic and porous material. Moreover, its mechanical properties are not constant with time, since its composition changes permanently in terms of the mechanical environment, ageing, disease, nutrition and other biological factors.

The first proposed models were elastic but they were early replaced by models that try to correlate mechanical properties with composition [26]. Vose and Kubala [198] were possibly the first to quantify how much mechanical properties depend on composition, obtaining a correlation between ultimate bending strength and mineral content.

One of the most cited works belongs to Carter and Hayes [25], who found that the elastic modulus and the strength of trabecular and cortical bone are closely related to the cube and square of the apparent wet bone density, respectively. Although these preliminary models only took into account the apparent density, several authors [37] have shown that the mechanical properties of cortical and cancellous bone depend both on the apparent density and the mineral content. So, Hernández et al. [76] express the elastic modulus and compressive strength, independently, as a function of the bone volume fraction and ash fraction.

Although all these correlations can predict the main mechanical properties, they do not consider the influence of structural and microstructural features or the different behaviours in each direction that is the well known anisotropy of bone tissue. This aspect has been considered by many authors. For instance, Lotz et al. [118] determined the Young's modulus and the compressive strength of cortical and trabecular femoral bone in the axial and transversal directions using the apparent density as a control variable.

The way to overcome this limitation is to employ anisotropic internal bone remodelling models that are able to predict density and anisotropy distribution, and some of them [41] with sufficient accuracy. Another assumption of most FE analyses in the literature is the linearity of the constitutive behaviour of bone tissue. This is usually accurate enough, but some authors have also used nonlinear material properties for cortical and trabecular bone [100].

Finally, when the interest is focussed on the surrounding soft tissues, many authors [17, 43, 63, 144] assume that bone tissue can be treated as a rigid element (taking into account that its stiffness is much higher than the one of soft tissue). This assumption involves a coarse simplification of the behaviour of bone tissue but helps in the treatment of complex joint models.

2.3 Constitutive Models for Soft Tissues

As mentioned before the components of soft tissues are quite similar. Usually, modelling of these tissues has been divided in two types depending on the influence of fluid flow: hydrated tissues and non-hydrated ones. Ligaments, tendons and muscles are treated as non-hydrated tissues, while cartilage as hydrated. However, except for the contribution of the fluid phase inside the tissue, the behaviour of the solid matrix in all these tissues is similar and therefore, the constitutive models that have been used follow also the same trend. In the following, a review of the classical and current constitutive models that have been developed for this kind of

tissues is presented. A complete description of these models is done for ligaments and cartilage, while the active response of muscles is briefly described in a separate section. Finally, the consideration of the initial stress state of these tissues will be briefly introduced.

2.3.1 Classical Models

The first mechanical models that were proposed in the literature used elastic models. For the ligaments, almost all the mathematical models that have been developed for joints, have used one-dimensional representations, since the primary function of ligaments is to resist tensile forces. A discrete element representation of ligaments requires a linear [47, 48] or quadratic function [20, 22, 75] to specify the force-elongation relationship for each element. A common approach has been to specify a reference length below which the element force was equal to zero [22]. Although one-dimensional representations can be used to predict ligament forces, they are unable to predict stress distributions throughout the ligament.

A more accurate approach is to consider the tissue as a three-dimensional continuum body. This is the case of the linear elastic models early proposed for cartilage. The first mechanical analysis for this tissue can be attributed to Hirsch [82], who used the solution of Hertz in the contact between two elastic spheres to determine the Young modulus of articular cartilage from an indentation experiment. In 1944, this researcher observed that the deformations increased under a constant load (creep) and that the tissue did not recover its shape completely after deformation. Thus, he suggested a new term called *imperfect elasticity*, effect that was studied posteriorly by Elmore et al. [50]. Timoshenko and Goodier [194] derived the following expression for the Young modulus for an incompressible material in an indentation experiment:

$$E = \frac{P}{2{,}67\omega_0 a} \tag{1}$$

where P was the applied load, a the radius of the cylindrical indentor, ω_0 the depth of the indentation, and $\nu = 0.5$. In the same way, another expression for the Young modulus was suggested by Hayes and Mokros [71]:

$$E = \frac{P(1-\nu^2)}{2\omega_0 a k(a/h, \nu)} \tag{2}$$

where k was defined in integral form, h was the thickness of the tissue, and P, ω_0, a and ν had the same meaning as in (1).

However, these models were not able to describe the finite deformations that these tissues support. Hyperelastic models were introduced to take into account this fact. For the case of ligaments, Pioletti et al. [157, 159] developed an isotropic hyperelastic model of the human anterior cruciate ligament. They proposed an incompressible isotropic model defined by the following strain energy function:

$$\Psi = \alpha e^{\beta(I_1-3)} + C_1(I_2 - 3) \tag{3}$$

Although this model was able to predict experimentally observed trends, it is known that the assumption of isotropy can introduce large errors in fiber-reinforced structures such as ligaments. These models do not take into account either the time dependent behaviour. Thus, viscoelastic models both for the intrinsic rate dependent response of the solid matrix and for the contribution of water inside tissues are necessary to simulate the overall behaviour of these tissues.

The first viscoelastic models for cartilage were composed only by a spring and a dashpot to take into account the creep phenomenon in the indentation experiment [34, 71, 130]. Parsons and Black [143] used a generalized Kelvin model consisting of several pairs of springs and dashpots connected in parallel with another spring in series. These authors introduced the concept of stiffness in *tight* and *relaxed* situations to describe the instantaneous and equilibrium modulus, and a *delay spectrum* to describe the creep response.

Barbenel et al. [13] generalized these spring and dashpot models by incorporating a logarithmic relaxation spectrum for ligaments. Sanjeevi [168] described the viscoelastic behavior of biological soft tissues with an equation similar to that of a Voigt-type spring and dashpot model. As with the elastic models, one-dimensional viscoelastic representations for ligaments can describe one-dimensional behavior, but are incapable of describing and predicting complex three-dimensional behavior. Continuum viscoelasticity theory can be applied to circumvent this shortcoming of one-dimensional approaches. In addition, continuum hyperelastic models can be readily extended to continuum viscoelasticity [201].

Fung [60] introduced a viscoelasticity theory that has become the most widely used in soft tissue biomechanics. This is referred to as Quasi Linear Viscoelasticity (QLV). The basis of this theory is that the stress at a given time can be described by a convolution integral representation, separating the elastic response and the relaxation function; the relaxation function has a specific continuous spectrum. It is assumed therefore that the stress relaxation function can be expressed as a convolution of a relaxation function with an elastic response

$$\mathbf{S}(t) = \mathbb{G}(t)\mathbf{S}^e(\mathbf{C}) \tag{4}$$

where $\mathbf{S}^e(\mathbf{C})$ is the elastic response and $\mathbb{G}(t)$ is a fourth-order tensor providing direction-dependent relaxation phenomena named as *reduced relaxation function*. One of the advantages of QLV theory is that it decouples the elastic contribution to the stress from the rate-dependent contributions. This makes it relatively easy to use any hyperelastic

model for the elastic contribution since the viscoelastic portion will remain unaffected. This model has however an important drawback, such as the information must be saved at every previous time step in order to compute the stress response at the current one.

Puso and Weiss [164] formulated a time discretization algorithm of the convolution integral in which the relaxation function and the elastic constitutive behaviour were split by means of a multiplicative decomposition, thus reducing the non-linear response of the tissue to the latter, maintaining the viscous behaviour within the framework of linear viscoelasticity. They developed a FE implementation of QLV using a discrete spectrum approximation. This approach was used to reduce the large amount of storage required for a continuous relaxation function. Their implementation used an exponential series approximation to $\mathbb{G}(t)$.

2.3.2 Current Models

The current models comprise the different aspects that, as mentioned before, the classical models did not take into account. The main characteristics of these models are the treatment of the anisotropy and the incorporation of three dimensional viscoelasticity. They have been applied to ligaments and tendons [81, 206], muscles [126] and the solid matrix of the cartilage [2, 97, 99, 211].

As mentioned before, biological soft tissues are subjected to large deformations with negligible volume changes, that is, only quasi-isochoric ($J \approx 1$) motions are possible. When these tissues are reinforced by only one family of fibers, they have a single preferred direction and are usually modelled as a *transversely isotropic hyperelastic material* [201] while in the case of two families of fibers they are modelled as an *anisotropic hyperelastic material* [84]. The formulation of finite strain hyperelasticity is usually expressed in terms of invariants with uncoupled volumetric/deviatoric responses, first suggested in [54], generalized in [179] and employed for anisotropic soft biological tissues in Weiss et al. [206], Holzapfel et al. [85], Peña et al. [150], Alastrue et al. [3], Pérez del Palomar and Doblaré [188] and [153].

Let $\mathbf{x} = \varphi(\mathbf{X}, t) : \Omega_0 \times \mathbb{R} \to \mathbb{R}^3$ denote the motion mapping and let $\mathbf{F}$ be the associated deformation gradient. Here $\mathbf{X}$ and $\mathbf{x}$ define the respective positions of a particle in the reference Ω_0 and current Ω configurations such as $\mathbf{F} = \mathrm{d}\mathbf{x}/\mathrm{d}\mathbf{X}$. Further, let $J \equiv \det \mathbf{F}$ be the Jacobian of the motion. To properly define volumetric and deviatoric responses in the non-linear range, we introduce the following kinematic decomposition [54]:

$$\mathbf{F} = J^{\frac{1}{3}}\bar{\mathbf{F}}, \qquad \bar{\mathbf{F}} = J^{-\frac{1}{3}}\mathbf{F} \tag{5}$$

$$\mathbf{C} = \mathbf{F}^T\mathbf{F}, \qquad \bar{\mathbf{C}} = J^{-\frac{2}{3}}\mathbf{C} = \bar{\mathbf{F}}^T\bar{\mathbf{F}} \tag{6}$$

The term $J^{\frac{1}{3}}\mathbf{I}$ is associated with volume-changing deformations, while $\bar{\mathbf{F}}$ is associated with volume-preserving deformations. We shall call $\bar{\mathbf{F}}$ and $\bar{\mathbf{C}}$ the modified deformation gradient and the modified right Cauchy–Green tensors, respectively.

The direction of a fiber at a point $\mathbf{X} \in \Omega_0$ is defined by a unit vector field $\mathbf{m}_0(\mathbf{X})$, $|\mathbf{m}_0| = 1$. It is usually assumed that, under deformation, the fiber moves with the material points of the continuum body. Therefore, the stretch λ of the fiber defined as the ratio between its length at the deformed and reference configurations can be expressed as

$$\begin{aligned} \lambda\mathbf{m}(\mathbf{x}, t) &= \mathbf{F}(X, t)\mathbf{m}_0(\mathbf{X}) \\ \lambda^2 &= \mathbf{m}_0 \cdot \mathbf{F}^T\mathbf{F} \cdot \mathbf{m}_0 = \mathbf{m}_0 \cdot \mathbf{C} \cdot \mathbf{m}_0 \end{aligned} \tag{7}$$

where $\mathbf{m}$ is the unit vector of the fiber in the deformed configuration.

The introduced kinematics for one family of fibers may be applied to other in an analogous manner. We will denote the second preferred direction by the unit vector field $\mathbf{n}_0(\mathbf{X})$.

To characterize isothermal processes, we postulate the existence of a unique decoupled representation of the strain-energy density function Ψ [178]. Based on the kinematic assumption (5) and following Spencer [185] it can be shown that eight modified invariants are necessary to form the integrity bases of the tensors $\bar{\mathbf{C}}, \mathbf{m}_0 \otimes \mathbf{m}_0, \mathbf{n}_0 \otimes \mathbf{n}_0$. Then, the free energy can be written in a decoupled form as

$$\begin{aligned} \Psi &= \Psi_{\mathrm{vol}}(J) + \bar{\Psi}\big(\bar{\mathbf{C}}, \mathbf{m}_0 \otimes \mathbf{m}_0, \mathbf{n}_0 \otimes \mathbf{n}_0\big) \\ &= \Psi_{\mathrm{vol}}(J) + \bar{\Psi}\big(\bar{I}_1, \bar{I}_2, \bar{I}_4, \bar{I}_5, \bar{I}_6, \bar{I}_7, \bar{I}_8, \bar{I}_9\big) \end{aligned} \tag{8}$$

with

$$\begin{aligned} &\bar{I}_1 = \mathrm{tr}\bar{\mathbf{C}}, \quad \bar{I}_2 = \frac{1}{2}\big(\mathrm{tr}(\bar{\mathbf{C}})^2 - \mathrm{tr}\bar{\mathbf{C}}^2\big), \\ &\bar{I}_4 = \mathbf{m}_0 \cdot \bar{\mathbf{C}} \cdot \mathbf{m}_0, \quad \bar{I}_5 = \mathbf{m}_0 \cdot \bar{\mathbf{C}}^2 \cdot \mathbf{m}_0, \\ &\bar{I}_6 = \mathbf{n}_0 \cdot \bar{\mathbf{C}} \cdot \mathbf{n}_0, \quad \bar{I}_7 = \mathbf{n}_0 \cdot \bar{\mathbf{C}}^2 \cdot \mathbf{n}_0, \\ &\bar{I}_8 = \mathbf{m}_0 \cdot \bar{\mathbf{C}} \cdot \mathbf{n}_0, \quad \bar{I}_9 = (\mathbf{n}_0 \cdot \mathbf{m}_0)^2 \end{aligned} \tag{9}$$

with $\bar{I}_1$ and $\bar{I}_2$ the first two strain invariants of the symmetric modified Cauchy–Green tensor, while the pseudo-invariants $\bar{I}_4, \ldots, \bar{I}_9$ characterize the anisotropic constitutive response of the fibers. $\bar{I}_4$ and $\bar{I}_6$ have a clear physical meaning, since they are the squares of the stretches along the two families of fibers. In order to reduce the number of material parameters and to work with physically motivated invariants, we shall omit the dependency of the free energy Ψ on $\bar{I}_5$, $\bar{I}_7$, $\bar{I}_8$ and $\bar{I}_9$. These invariants are usually not included in the formulations directly since most of their effects can be introduced in the strain energy density function through derivatives with respect to the invariants $\bar{I}_4$ and $\bar{I}_6$ [206]. Besides, the strong correlation of $\bar{I}_5$ and $\bar{I}_7$ with $\bar{I}_4$ and $\bar{I}_6$ leads to an ill posed

parameter estimation problem for most experiments. Finally, $\bar{I}_8$ is related to the interaction between both families of fibers that is usually discarded, and $\bar{I}_9$ is not strain dependent. This hypothesis is usually used in biomechanical modelling [87].

Materials which keep the volume constant throughout a motion are characterized by the incompressibility constraint $J = 1$. In order to derive general constitutive equations for incompressible hyperelastic materials, we can postulate the strain-energy function

$$\Psi_{\text{vol}}(J) = \frac{1}{D}(J-1)^2 \tag{10}$$

where $\Psi_{\text{vol}}(1) = 0$ and $\bar{\Psi}$ is defined for $J = 1$. The scalar p introduced in (10) serves as an indeterminate *Lagrangian multiplier*, which can be identified as the hydrostatic pressure. Note that the scalar p represents a workless reaction to the kinematic constraint on the deformation field and may only be determined from the equilibrium equations and boundary conditions [84].

The stress response is obtained from the derivatives of the stored-energy function, getting

$$\begin{aligned}\mathbf{S} &= 2\frac{\partial \Psi}{\partial \mathbf{C}} = \mathbf{S}_{\text{vol}} + \bar{\mathbf{S}} \\ &= Jp\mathbf{C}^{-1} + J^{-\frac{2}{3}}\left(\mathbb{I} - 1/3\mathbf{C}^{-1}\otimes\mathbf{C}\right) : \widetilde{\mathbf{S}}\end{aligned} \tag{11}$$

where $\mathbf{S}_{\text{vol}}$ and $\bar{\mathbf{S}}$ are the volumetric and deviatoric parts of the second Piola–Kirchhoff stress tensor, p is the hydrostatic pressure and $\widetilde{\mathbf{S}}$ the modified second Piola–Kirchhoff stress tensor

$$p = \frac{d\Psi_{\text{vol}}(J)}{dJ} \qquad \widetilde{\mathbf{S}} = 2\frac{\partial \bar{\Psi}(\bar{\mathbf{C}}, \mathbf{m}_0, \mathbf{n}_0)}{\partial \bar{\mathbf{C}}} \tag{12}$$

The explicit expressions for the second Piola–Kirchhoff stress tensor depending of the defined invariants is

$$\begin{aligned}\mathbf{S} = 2\frac{\partial \Psi}{\partial \mathbf{C}} &= Jp\mathbf{C}^{-1} + 2\Bigg[\left(\frac{\partial \bar{\Psi}}{\partial \bar{I}_1} + \bar{I}_1\frac{\partial \bar{\Psi}}{\partial \bar{I}_2}\right)\mathbf{1} - \frac{\partial \bar{\Psi}}{\partial \bar{I}_2}\bar{\mathbf{C}} \\ &+ \bar{I}_4\frac{\partial \bar{\Psi}}{\partial \bar{I}_4}\mathbf{m}_0\otimes\mathbf{m}_0 + \bar{I}_6\frac{\partial \bar{\Psi}}{\partial \bar{I}_6}\mathbf{n}_0\otimes\mathbf{n}_0 \\ &- \frac{1}{3}\left(\frac{\partial \bar{\Psi}}{\partial \bar{I}_1}\bar{I}_1 + 2\frac{\partial \bar{\Psi}}{\partial \bar{I}_2}\bar{I}_2 + \frac{\partial \bar{\Psi}}{\partial \bar{I}_4}\bar{I}_4 + \frac{\partial \bar{\Psi}}{\partial \bar{I}_6}\bar{I}_6\right)\mathbf{C}^{-1}\Bigg]\end{aligned} \tag{13}$$

The Cauchy stress tensor $\boldsymbol{\sigma}$ is $1/J$ times the push-forward of $\mathbf{S}$ ($\boldsymbol{\sigma} = J^{-1}\boldsymbol{\chi}_*(\boldsymbol{S})$), that is, $\sigma_{ij} = J^{-1}F_{iI}F_{jJ}S_{IJ}$, so, from (11), we obtain

$$\boldsymbol{\sigma} = p\mathbf{1} + \frac{2}{J}\text{dev}\left[\bar{\mathbf{F}}\frac{\partial \bar{\Psi}(\bar{\mathbf{C}}, \mathbf{m}_0, \mathbf{n}_0)}{\partial \bar{\mathbf{C}}}\bar{\mathbf{F}}^T\right] \tag{14}$$

with $\mathbf{1}$ the second-order identity tensor and dev the deviator operator in the spatial description [177].

From (13), we obtain

$$\begin{aligned}\boldsymbol{\sigma} = p\mathbf{1} + \frac{2}{J}\Bigg[&\left(\frac{\partial \bar{\Psi}}{\partial \bar{I}_1} + \bar{I}_1\frac{\partial \bar{\Psi}}{\partial \bar{I}_2}\right)\bar{\mathbf{b}} - \frac{\partial \bar{\Psi}}{\partial \bar{I}_2}\bar{\mathbf{b}}^2 \\ &+ \bar{I}_4\frac{\partial \bar{\Psi}}{\partial \bar{I}_4}\mathbf{m}\otimes\mathbf{m} + \bar{I}_6\frac{\partial \bar{\Psi}}{\partial \bar{I}_6}\mathbf{n}\otimes\mathbf{n} \\ &- \frac{1}{3}\left(\frac{\partial \bar{\Psi}}{\partial \bar{I}_1}\bar{I}_1 + 2\frac{\partial \bar{\Psi}}{\partial \bar{I}_2}\bar{I}_2 + \frac{\partial \bar{\Psi}}{\partial \bar{I}_4}\bar{I}_4 + \frac{\partial \bar{\Psi}}{\partial \bar{I}_6}\bar{I}_6\right)\mathbf{1}\Bigg]\end{aligned} \tag{15}$$

The development of uncoupled volumetric/deviatoric finite deformation elasticity with two families of fibers can be concluded by recording the explicit expressions for the elastic tangent moduli. The tangent modulus plays a crucial role in the numerical solution of the boundary value problem by Newton-type iterative methods [218]. The use of consistently linearized moduli is essential to preserve the quadratic rate of the asymptotic convergence that characterizes full Newton's method [90]. Consider the nonlinear second Piola–Kirchhoff stress tensor $\mathbf{S}$ at a certain point. Its variation with respect to the right Cauchy–Green tensor $\mathbf{C}$ is *the elasticity tensor* in the material description or *the referential tensor of elasticities* and may be written as

$$\mathbb{C} = 2\frac{\partial \mathbf{S}(\mathbf{C})}{\partial \mathbf{C}} = \mathbb{C}_{\text{vol}} + \bar{\mathbb{C}} = 2\frac{\partial \mathbf{S}_{\text{vol}}}{\partial \mathbf{C}} + 2\frac{\partial \bar{\mathbf{S}}}{\partial \mathbf{C}} \tag{16}$$

where $\mathbb{C}_{\text{vol}}$ and $\bar{\mathbb{C}}$ may be written as [177]

$$\begin{aligned}\mathbb{C}_{\text{vol}} &= 2\mathbf{C}^{-1}\otimes\left(p\frac{\partial J}{\partial \mathbf{C}} + J\frac{\partial p}{\partial \mathbf{C}} + 2Jp\frac{\partial \mathbf{C}^{-1}}{\partial \mathbf{C}}\right) \\ &= J\tilde{p}\mathbf{C}^{-1}\otimes\mathbf{C}^{-1} - 2Jp\mathbf{C}^{-1}\odot\mathbf{C}^{-1}\end{aligned} \tag{17}$$

$$\begin{aligned}\bar{\mathbb{C}} = &-\frac{4}{3}J^{-\frac{4}{3}}\left(\frac{\partial \bar{\Psi}}{\partial \bar{\mathbf{C}}}\otimes\bar{\mathbf{C}}^{-1} + \bar{\mathbf{C}}^{-1}\otimes\frac{\partial \bar{\Psi}}{\partial \bar{\mathbf{C}}}\right) \\ &+ \frac{4}{3}J^{-\frac{4}{3}}\left(\frac{\partial \bar{\Psi}}{\partial \bar{\mathbf{C}}} : \bar{\mathbf{C}}\right)\left(\mathbb{I}_C^{-1} + \frac{1}{3}\bar{\mathbf{C}}^{-1}\otimes\bar{\mathbf{C}}^{-1}\right) \\ &+ J^{-\frac{4}{3}}\bar{\mathbb{C}}_{\bar{w}}\end{aligned} \tag{18}$$

$$\begin{aligned}\bar{\mathbb{C}}_{\bar{w}} = &4\frac{\partial^2 \bar{\Psi}}{\partial \bar{\mathbf{C}}\partial \bar{\mathbf{C}}} - \frac{4}{3}\Bigg[\left(\frac{\partial^2 \bar{\Psi}}{\partial \bar{\mathbf{C}}\partial \bar{\mathbf{C}}} : \bar{\mathbf{C}}\right)\otimes\bar{\mathbf{C}}^{-1} \\ &+ \bar{\mathbf{C}}^{-1}\otimes\left(\frac{\partial^2 \bar{\Psi}}{\partial \bar{\mathbf{C}}\partial \bar{\mathbf{C}}} : \bar{\mathbf{C}}\right)\Bigg] \\ &+ \frac{4}{9}\left(\bar{\mathbf{C}} : \frac{\partial^2 \bar{\Psi}}{\partial \bar{\mathbf{C}}\partial \bar{\mathbf{C}}} : \bar{\mathbf{C}}\right)\bar{\mathbf{C}}^{-1}\otimes\bar{\mathbf{C}}^{-1}\end{aligned} \tag{19}$$

with $\mathbb{I}_{C^{-1}} = \partial\mathbf{C}^{-1}/\partial\mathbf{C} = -\mathbf{C}^{-1}\odot\mathbf{C}^{-1} = -(1/2)\times(C^{-1}_{IK}C^{-1}_{JL} + C^{-1}_{IL}C^{-1}_{JK})$. For convenience, the scalar function $\tilde{p}$ is introduced and is defined by

$$\tilde{p} = p + J\frac{\mathrm{d}p}{\mathrm{d}J} \tag{20}$$

with the constitutive equation for p given in $(12)_a$.

The elasticity tensor in the spatial description is defined as the push forward of c

$$c = c_{\text{vol}} + \bar{c} \tag{21}$$

where c_{vol} is defined as

$$c_{\text{vol}} = p(\mathbf{1} \otimes \mathbf{1} - 2\mathbb{I}) \tag{22}$$

with $\mathbb{I}$ the fourth-order identity tensor, p defined in (12) and $\bar{c}$

$$\begin{aligned}
\bar{c} = &-\frac{2}{3}(\operatorname{dev}\boldsymbol{\sigma} \otimes \mathbf{1} + \mathbf{1} \otimes \operatorname{dev}\boldsymbol{\sigma}) \\
&- \frac{4}{3J}\big[\big(\bar{\Psi}_1 + \bar{\Psi}_2\bar{I}_1\big)\bar{I}_1 - \bar{\Psi}_2\big(\bar{I}_1^2 - 2\bar{I}_2\big) + \bar{\Psi}_4\bar{I}_4 \\
&+ \bar{\Psi}_6\bar{I}_6\big]\left(\mathbb{I} - \frac{1}{3}\mathbf{1} \otimes \mathbf{1}\right) + 4\big[\big(\bar{\Psi}_{11} + 2\bar{\Psi}_{12}\bar{I}_1 + \bar{\Psi}_2 \\
&+ \bar{\Psi}_{22}\bar{I}_1^2\big)\bar{\boldsymbol{b}} \otimes \bar{\boldsymbol{b}} + \bar{\Psi}_{22}\big(\bar{\boldsymbol{b}}^2 \otimes \bar{\boldsymbol{b}}^2\big) - \bar{\Psi}_2\bar{\mathbb{I}}_{\bar{\boldsymbol{b}}} - \big(\bar{\Psi}_{12} \\
&+ \bar{\Psi}_{22}\bar{I}_1\big)(\bar{\boldsymbol{b}} \otimes \bar{\boldsymbol{b}}^2 + \bar{\boldsymbol{b}}^2 \otimes \bar{\boldsymbol{b}}) + \big(\bar{\Psi}_{14} + \bar{\Psi}_{24}\bar{I}_1\big)\bar{I}_4 \\
&\times (\bar{\boldsymbol{b}} \otimes \boldsymbol{m} \otimes \boldsymbol{m} + \boldsymbol{m} \otimes \boldsymbol{m} \otimes \bar{\boldsymbol{b}}) + \big(\bar{\Psi}_{16} + \bar{\Psi}_{26}\bar{I}_1\big) \\
&\times \bar{I}_6(\bar{\boldsymbol{b}} \otimes \boldsymbol{n} \otimes \boldsymbol{n} + \boldsymbol{n} \otimes \boldsymbol{n} \otimes \bar{\boldsymbol{b}}) - \bar{\Psi}_{22}\bar{I}_4\big(\bar{\boldsymbol{b}}^2 \otimes \boldsymbol{m} \\
&\otimes \boldsymbol{m} + \boldsymbol{m} \otimes \boldsymbol{m} \otimes \bar{\boldsymbol{b}}^2\big) + \bar{\Psi}_{44}\bar{I}_4^2(\boldsymbol{m} \otimes \boldsymbol{m} \otimes \boldsymbol{m} \otimes \boldsymbol{m}) \\
&- \bar{\Psi}_{22}\bar{I}_6\big(\bar{\boldsymbol{b}}^2 \otimes \boldsymbol{n} \otimes \boldsymbol{n} + \boldsymbol{n} \otimes \boldsymbol{n} \otimes \bar{\boldsymbol{b}}^2\big) + \bar{\Psi}_{66}\bar{I}_6^2 \\
&\times (\boldsymbol{n} \otimes \boldsymbol{n} \otimes \boldsymbol{n} \otimes \boldsymbol{n}) - \frac{4}{3}\big[\big(\bar{\Psi}_{11}\bar{I}_1 + \bar{\Psi}_{12}\bar{I}_1^2 \\
&+ \bar{\Psi}_{12}\bar{I}_2 + \bar{\Psi}_2\bar{I}_1 + 2\bar{\Psi}_{22}\bar{I}_1\bar{I}_2 + \bar{\Psi}_{14}\bar{I}_4 + \bar{\Psi}_{24}\bar{I}_1\bar{I}_4 \\
&+ \bar{\Psi}_{16}\bar{I}_6 + \bar{\Psi}_{26}\bar{I}_1\bar{I}_6\big)\bar{\boldsymbol{b}} - \big(\bar{\Psi}_{12}\bar{I}_1 + 2\bar{\Psi}_{22}\bar{I}_2 + \bar{\Psi}_2 \\
&+ \bar{\Psi}_{24}\bar{I}_4 + \bar{\Psi}_{26}\bar{I}_6\big)\bar{\boldsymbol{b}}^2 + \big(\bar{\Psi}_{14}\bar{I}_1 + 2\bar{\Psi}_{22}\bar{I}_2 \\
&+ \bar{\Psi}_{44}\bar{I}_4\big)\boldsymbol{m} \otimes \boldsymbol{m} \otimes \bar{\boldsymbol{b}} + \big(\bar{\Psi}_{16}\bar{I}_1 + 2\bar{\Psi}_{22}\bar{I}_2 \\
&+ \bar{\Psi}_{66}\bar{I}_6\big)\boldsymbol{n} \otimes \boldsymbol{n} \otimes \bar{\boldsymbol{b}} + \mathbf{1} \otimes \big(\big(\bar{\Psi}_{11}\bar{I}_1 + \bar{\Psi}_{12}\bar{I}_1^2 \\
&+ \bar{\Psi}_{12}\bar{I}_2 + \bar{\Psi}_2\bar{I}_1 + 2\bar{\Psi}_{22}\bar{I}_1\bar{I}_2 + \bar{\Psi}_{14}\bar{I}_4 + \bar{\Psi}_{24}\bar{I}_1\bar{I}_4 \\
&+ \bar{\Psi}_{16}\bar{I}_6 + \bar{\Psi}_{26}\bar{I}_1\bar{I}_6\big)\bar{\boldsymbol{b}} - \big(\bar{\Psi}_{12}\bar{I}_1 + 2\bar{\Psi}_{22}\bar{I}_2 + \bar{\Psi}_2 \\
&+ \bar{\Psi}_{24}\bar{I}_4 + \bar{\Psi}_{26}\bar{I}_6\big)\bar{\boldsymbol{b}}^2 + \big(\bar{\Psi}_{14}\bar{I}_1 + 2\bar{\Psi}_{24}\bar{I}_2 \\
&+ \bar{\Psi}_{44}\bar{I}_4\big)\boldsymbol{m} \otimes \boldsymbol{m}\big) + \big(\bar{\Psi}_{16}\bar{I}_1 + 2\bar{\Psi}_{26}\bar{I}_2 + \bar{\Psi}_{66}\bar{I}_6\big) \\
&\times (\boldsymbol{n} \otimes \boldsymbol{n})\big] + \frac{4}{9}\big[\big(\big(\bar{\Psi}_{11} - \bar{\Psi}_{12}\big)\bar{I}_1^2 + 2\bar{\Psi}_2\bar{I}_2 + 4\bar{\Psi}_{22}\bar{I}_2^2 \\
&+ 4\bar{\Psi}_{12}\bar{I}_1\bar{I}_2 + 2\bar{\Psi}_{14}\bar{I}_1\bar{I}_4 + 2\bar{\Psi}_{16}\bar{I}_1\bar{I}_6 + 4\bar{\Psi}_{24}\bar{I}_2\bar{I}_4 \\
&+ \bar{\Psi}_{44}\bar{I}_4^2 + 4\bar{\Psi}_{26}\bar{I}_2\bar{I}_6 + \bar{\Psi}_{66}\bar{I}_6^2)\mathbf{1} \otimes \mathbf{1}\big]
\end{aligned} \tag{23}$$

Following this approach, different strain energy functions have been proposed in order to take into account both the isotropy related to the solid matrix and the anisotropy introduced by the collagen fibers.

Lanir [109] used a strain energy approach to form a continuum model for fibrous connective tissue. The deformation energy was assumed to arise from the tensile stretch in the collagen fibers, with the only contribution from the matrix being a simple hydrostatic pressure. The model described an incompressible composite of undulating collagen fibers embedded in a fluid matrix. The model assumed that the collagen fibers buckle under a compressive load and the unfolding of the fibers during deformation squeezed the matrix, resulting in an internal hydrostatic pressure. The stress due to the deformation was described by

$$\mathbf{S} = \lambda W_\lambda \mathbf{m} \otimes \mathbf{m} + p\mathbf{1} \tag{24}$$

where λ is the collagen fiber stretch, W_λ is the strain energy contribution from the collagen fibers, $\mathbf{m}$ is a unit vector describing the local fiber direction, and p is the hydrostatic pressure arising from the matrix.

The most used transverse model for ligaments is the early proposed by Weiss [206]. The strain energy function for incompressible material was divided into an isotropic part that corresponds to a Neo-Hookean model and other depending on the collagen fibers (F_λ).

$$\Psi = C_1\big(\bar{I}_1 - 3\big) + F_\lambda(\lambda) \tag{25}$$

where C_1 is the Neo-Hookean constant, D the inverse of the bulk modulus $k = 1/D$, $\bar{I}_1$ is the first modified strain invariant of the symmetric modified Cauchy–Green tensor $\bar{\mathbf{C}}$.

Following physical observations in human ligaments, they assumed that collagen fibers do not support compressive loads, Fig. 2. The derivatives of the term of the free-energy function related to the fibers that were initially proposed by Weiss et al. [206] can be written as:

$$\begin{aligned}
&\lambda\Psi_\lambda = 0 \quad \lambda < 1 \\
&\lambda\Psi_\lambda = C_3\big(e^{C_4(\lambda-1)} - 1\big) \quad \lambda < \lambda^* \\
&\lambda\Psi_\lambda = C_5\lambda + C_6 \quad \lambda > \lambda^*
\end{aligned} \tag{26}$$

where $\Psi_\lambda = \partial F_\lambda/\partial\lambda$, λ^* is the stretch at which collagen fibers start to be straightened, changing Ψ_λ from exponential to linear, C_3 scales the exponential stress, C_4 is related to the rate of collagen uncrimping and C_5 is the elastic modulus of the straightened collagen fibers.

Limbert et al. [115] proposed another ligament model where the strain energy function takes the form

$$\Psi = C_1\big(\bar{I}_1 - 3\big) + \Psi_\lambda(\lambda) \tag{27}$$

and the term Ψ_λ is defined in the following form

$$\Psi_\lambda = 0 \quad I_4 < 1$$
$$\Psi_\lambda = \frac{C_2}{C_3}\left(e^{C_3(I_4-1)^2} - 1\right) \quad 1 \le I_4 < I_4^* \tag{28}$$
$$\Psi_\lambda = 2C_4\sqrt{I_4} + C_5 \ln I_4 \quad I_4 \ge I_4^*$$

where $I_4 = \lambda^2$.

Hirokawa et al. [80, 81] proposed an anisotropic hyperelastic model for ligaments where the anisotropy was defined by a two vector field. This model is more useful for soft tissues characterized by the existence of two family of the fibers as blood vessels [85] or human cornea [3].

Regarding cartilage, Cohen et al. [32, 33] demonstrated that the linear transversely isotropic biphasic theory could provide successful results, suggesting that the difficulties encountered with the isotropic model could be overcome by modeling tissue anisotropy, similarly to the earlier work of Lanir et al. [108]. Soulhat et al. [184] proposed a fibril-network reinforced model for the solid phase of biphasic cartilage that incorporates tension-compression nonlinearity, when the collagen fibrils can only sustain tensile stresses. In the same way, Li et al. [119, 120] considered the solid phase of the matrix as elastic, and introduced collagen fibers like springs that only worked in tension. Korhonen et al. [105] used a similar model to study the behaviour of the healthy cartilage. They compared its behaviour when the collagen network is damaged modifying the stiffness of the springs that simulates the collagen fibers. In the same way, Park et al. [142] suggested the significance of the introduction of different properties in the tissue under traction and compression, relating them with the pressurization of the tissue.

Different strain energy functions have been proposed for cartilage [4, 188]. However, only Almeida and Spilker [6] and Pérez del Palomar and Doblaré [153] have used transversely isotropic hyperelastic models to model the collagen fibers of the solid phase. In [153] for example, the strain density energy function earlier proposed by Holzapfel et al. [84],

$$\Psi = C_1\left(\bar{I}_1 - 3\right) + \frac{K_1}{2K_2}\left\{\exp\left[K_2\left(\bar{I}_4 - 1\right)^2\right] - 1\right\} + \frac{1}{D}(J-1)^2 \tag{29}$$

was used.

The second aspect that the current constitutive models includes is tissues' time dependent behaviour [60, 67, 71, 114, 158]. Pioletti et al. [158, 160] developed a three-dimensional, visco-hyperelastic model for ligaments and tendons that included nonlinear elastic behavior, short-term memory effects, and long-term memory effects. The short-term memory effects describe the dependence of stress on the strain rate while the long-term memory effects describe stress relaxation on a longer time scale. The second Piola–Kirchhoff stress tensor is then written as:

$$\begin{aligned}\mathbf{S}(t) &= \mathbf{S}_e\left(\mathbf{C}(t)\right) + \mathbf{S}_v\left(\mathbf{C}(t); \dot{\mathbf{C}}(t)\right) \\ &\quad + \int_0^\infty \sum \mathbf{G}\left((t-s), s\right)\mathbf{C}(t)\,\mathrm{d}s \\ &= \frac{\partial \Psi_e}{\partial \mathbf{C}} + \frac{\partial \Psi_v}{\partial \dot{\mathbf{C}}} + \int_0^\infty \sum \mathbf{G}\left((t-s), s\right)\mathbf{C}(t)\,\mathrm{d}s\end{aligned} \tag{30}$$

where Ψ_e is the previously defined strain energy function for a hyperelastic material and Ψ_v is a similarly defined dissipative potential for short-term memory effects from which the viscous stress is derived. The model was limited by considering specimens to be isotropic, homogeneous and incompressible. Limbert and Middleton [114] extended the dissipative potential Ψ_v to the anisotropic case. These phenomenological approaches [114, 158] have however an important drawback, they involve 10 and 15 invariants, respectively.

A fully three-dimensional finite strain viscoelastic model not restricted to the isotropic domain was developed by Simo [176]. This model is based on the concept of internal variables and allows a very general description of materials involving irreversible effects. This constitutive model was applied to model the mechanical behavior of isotropic elastomers. Following Simo's constitutive framework, Holzapfel and Gasser [86] proposed a Maxwell type viscoelastic model of fiber-reinforced composites at finite strains that considered a different viscoelastic behaviour for the matrix and the fibers. The proposed constitutive expression for the second Piola–Kirchhoff stress tensor is:

$$\mathbf{S} = 2\frac{\partial \Psi(\mathbf{C}, \mathbf{m}_0, \mathbf{n}_0, \mathbf{Q}_i)}{\partial \mathbf{C}} = \mathbf{S}_{\mathrm{vol}}^{\infty} + \mathbf{S}_{\mathrm{iso}}^{\infty} + \sum_{i=1}^{n} \mathbf{Q}_i \tag{31}$$

where $\mathbf{S}_{\mathrm{vol}}^{\infty}$ and $\mathbf{S}_{\mathrm{iso}}^{\infty}$ define the stress response at $(t \to \infty)$ and $\mathbf{Q}_i$ may be interpreted as non-equilibrium stresses associated to matrix and fibers.

However, ligaments are usually assumed to have a Kelvin–Voight-type viscoelastic constitutive behaviour [165, 169, 197]. Following Simo [176] and Holzapfel and Gasser [86], Peña et al. [148] presented a fully three-dimensional finite strain anisotropic visco-hyperelastic Kelvin–Voight model for ligaments. They postulated the existence of an uncoupled free energy function of the form

$$\begin{aligned}&\Psi(\mathbf{C}, \mathbf{m}_0, \mathbf{n}_0, \mathbf{Q}_i) \\ &= \Psi_{\mathrm{vol}}^0(J) + \bar{\Psi}^0(\bar{\mathbf{C}}, \mathbf{m}_0 \otimes \mathbf{m}_0, \mathbf{n}_0 \otimes \mathbf{n}_0) \\ &\quad - \sum_{i=1}^{n} \frac{1}{2}\bar{\mathbf{C}} : \mathbf{Q}_i + \Xi\left(\sum_{i=1}^{n} \mathbf{Q}_i\right)\end{aligned} \tag{32}$$

where Ψ^0_{vol} and $\bar{\Psi}^0$ are the volumetric and deviatoric parts of the initial elastic stored energy function Ψ^0, $\mathbf{Q}_i$ play the role of internal variables (not accessible to direct observation) corresponding to the reference configuration and Ξ is a certain function of the internal variables.

Restricting the attention to the isothermal case and exploiting the Clausius–Duhem inequality $\mathcal{D}_{\text{int}} = -\dot{\Psi} + \frac{1}{2}\mathbf{S} : \dot{\mathbf{C}} \geq 0$ [125], one gets

$$\begin{aligned}\mathbf{S} &= 2\frac{\partial \Psi(\mathbf{C}, \mathbf{m}_0, \mathbf{n}_0, \mathbf{Q}_i)}{\partial \mathbf{C}} = Jp\mathbf{C}^{-1} \\ &\quad + J^{-\frac{2}{3}}\,\text{dev}\left[2\frac{\partial \bar{\Psi}^0(\bar{\mathbf{C}}, \mathbf{m}_0, \mathbf{n}_0)}{\partial \bar{\mathbf{C}}} - \sum_{i=1}^{n}\mathbf{Q}_i\right] \\ &= \mathbf{S}^0_{\text{vol}} + \bar{\mathbf{S}}^0 - J^{-\frac{2}{3}}\,\text{dev}\left[\sum_{i=1}^{n}\mathbf{Q}_i\right] \end{aligned} \tag{33}$$

$$\begin{aligned}\mathcal{D}_{\text{int}} &= -\sum_{i=1}^{n}\frac{\partial \Psi(\mathbf{C}, \mathbf{m}_0, \mathbf{n}_0, \mathbf{Q}_i)}{\partial \mathbf{Q}_i} : \dot{\mathbf{Q}}_i \\ &= \sum_{i=1}^{n}\left[\frac{1}{2}\bar{\mathbf{C}} - \frac{\partial \Xi(\mathbf{Q}_i)}{\partial \mathbf{Q}_i}\right] : \dot{\mathbf{Q}}_i \geq 0 \end{aligned} \tag{34}$$

$\mathbf{Q}_i$ may be interpreted as non-equilibrium stresses, in the sense of non-equilibrium thermodynamics, and remain unaltered under superposed spatial rigid body motions [177]. This fundamental requirement is the same invariance property classically placed on the second Piola–Kirchhoff tensor $\mathbf{S}$ and automatically ensures frame indifference of the constitutive relationship (33).

Since $\boldsymbol{\sigma} = (1/J)\mathbf{F}\mathbf{S}\mathbf{F}^T$, in the spatial description expression (33) may be recast in the equivalent form

$$\boldsymbol{\sigma} = p\mathbf{1} + \frac{1}{J}\,\text{dev}\left[\bar{\mathbf{F}}\left\{2\frac{\partial \bar{\Psi}^0(\bar{\mathbf{C}}, \mathbf{m}_0, \mathbf{n}_0)}{\partial \bar{\mathbf{C}}} - \sum_{i=1}^{n}\mathbf{Q}_i\right\}\bar{\mathbf{F}}^T\right] \tag{35}$$

Motivated by Holzapfel and Gasser [86] and in order to consider different contributions of the matrix material and families of fibers on the non-equilibrium part, the internal variables can be divided in the following way:

$$\mathbf{Q}_i = \sum_{j=1\, j\neq 3}^{9}\mathbf{Q}_{ij} \tag{36}$$

where $\mathbf{Q}_{i1}$ and $\mathbf{Q}_{i2}$ are the isotropic contribution due to the matrix material associated to $\bar{I}_1$ and $\bar{I}_2$ invariants and $\mathbf{Q}_{i4}, \ldots, \mathbf{Q}_{i9}$ are the anisotropic contribution due to the two families of fibers associated to $\bar{I}_4, \ldots, \bar{I}_9$ invariants. Thus, the evolution equations can be formulated in a separate form for each contribution. The following set of rate equations governing the evolution of internal variables $\mathbf{Q}_{ij}$ can be considered [176]

$$\dot{\mathbf{Q}}_{ij} + \frac{1}{\tau_{ij}}\mathbf{Q}_{ij} = \frac{\gamma_{ij}}{\tau_{ij}}\,\text{dev}\left[2\delta\bar{\Psi}^{0(j)}\right] \qquad \lim_{t\to-\infty}\mathbf{Q}_{ij} = \mathbf{0} \tag{37}$$

with $\gamma_{ij} \in [0, 1]$ are free energy factors associated with relaxation time $\tau_{ij} > 0$ and $\delta\bar{\Psi}^{0(j)} = (\partial\bar{\Psi}^0/\partial I_j)(\partial I_j/\partial\bar{\mathbf{C}})$.

The evolution equations (37) are linear and, therefore, explicitly lead to the following convolution representation

$$\mathbf{Q}_{ij}(t) = \frac{\gamma_{ij}}{\tau_{ij}}\int_{-\infty}^{t}\exp\left[\frac{-(t-s)}{\tau_{ij}}\right]\text{dev}\left[2\delta\bar{\Psi}^{0(j)}\right]\text{d}s \tag{38}$$

Ξ can be determined from the condition of thermodynamic equilibrium [176]. It is clear that, given the rate equations (37), equilibrium is achieved for

$$\begin{aligned}&\dot{\mathbf{Q}}_{ij} = \mathbf{0} \Longrightarrow \mathbf{Q}_{ij} = \gamma_{ij}\,\text{dev}\left[2\delta\bar{\Psi}^{0(j)}\right] \\ &\frac{\partial\delta\bar{\Psi}^{0(j)}}{\partial\mathbf{Q}_{ij}} = 0 \Longrightarrow \sum_{i=1}^{n}\sum_{j=1, j\neq 3}^{9}\left[-\frac{1}{2}\bar{\mathbf{C}} + \frac{\partial\Xi}{\partial\mathbf{Q}_{ij}}\right] = \mathbf{0}\end{aligned} \tag{39}$$

Equation (39) defines Ξ as the Legendre transformation of the function Ψ^0_{iso} in the sense that

$$\Xi(\mathbf{Q}_{ij}) = \sum_{i=1}^{n}\left[\sum_{j=1, j\neq 3}^{9}\left[-2\gamma_{ij}\delta\bar{\Psi}^{0(j)}\right] + \frac{1}{2}\bar{\mathbf{C}} : \sum_{j=1, j\neq 3}^{9}\mathbf{Q}_{ij}\right] \tag{40}$$

Substitution of (38) into (33) and integrating by parts then yields the following equivalent expression

$$\begin{aligned}\mathbf{S} &= Jp\mathbf{C}^{-1} + J^{-\frac{2}{3}}\sum_{j=1, j\neq 3}^{9}\left[\left(1 - \sum_{i=1}^{n}\gamma_{ij}\right)\right. \\ &\quad \left.\times\,\text{dev}\left\{2\delta\bar{\Psi}^{0(j)}\left(\bar{\mathbf{C}}, \mathbf{m}_0, \mathbf{n}_0\right)\right\}\right] \\ &\quad + \sum_{i=1}^{n}\sum_{j=1, j\neq 3}^{9}\left[J^{-\frac{2}{3}}\gamma_{ij}\int_{-\infty}^{t}\exp\left[\frac{-(t-s)}{\tau_{ij}}\right]\frac{\text{d}}{\text{d}s}\right. \\ &\quad \left.\left\{\text{dev}\left[2\delta\bar{\Psi}^{0(j)}\left(\bar{\mathbf{C}}, \mathbf{m}_0, \mathbf{n}_0\right)\right]\right\}\text{d}s\right]\end{aligned} \tag{41}$$

Note that $\mathbf{Q}_i$ attains its equilibrium value (39) as $t/\tau_{ij} \longrightarrow \infty$. The corresponding value of the equilibrium stress is a fraction of the initial stress; that is

$$\begin{aligned}\lim_{\frac{t}{\tau_{ij}}\longrightarrow\infty}\mathbf{S} &= Jp\mathbf{C}^{-1} + J^{-\frac{2}{3}}\sum_{j=1, j\neq 3}^{9}\left[\left(1 - \sum_{i=1}^{n}\gamma_{ij}\right)\right. \\ &\quad \left.\times\,\text{dev}\left\{2\delta\bar{\Psi}^{0(j)}\left(\bar{\mathbf{C}}, \mathbf{m}_0, \mathbf{n}_0\right)\right\}\right]\end{aligned} \tag{42}$$

The convolution representation (41) in terms of the Cauchy stress tensor takes the form [148]

$$\boldsymbol{\sigma} = p\mathbf{1} + \frac{1}{J}\Bigg[\sum_{j=1,j\neq 3}^{9}\Bigg[\left(1-\sum_{i=1}^{n}\gamma_{ij}\right) \times \mathrm{dev}\left\{\bar{\mathbf{F}}\left[2\delta\bar{\Psi}^{0(j)}\left(\bar{\mathbf{C}},\mathbf{m}_0,\mathbf{n}_0\right)\right]\bar{\mathbf{F}}^T\right\}\Bigg] + \sum_{i=1}^{n}\sum_{j=1,j\neq 3}^{9}\Bigg[\gamma_{ij}\int_{-\infty}^{t}\exp\left[\frac{-(t-s)}{\tau_{ij}}\right]\frac{\mathrm{d}}{\mathrm{d}s} \left\{\mathrm{dev}\left\{\bar{\mathbf{F}}\left[2\delta\bar{\Psi}^{0(j)}\left(\bar{\mathbf{C}},\mathbf{m}_0,\mathbf{n}_0\right)\right]\bar{\mathbf{F}}^T\right\}\right\}\mathrm{d}s\Bigg]\Bigg] \tag{43}$$

Both the anisotropic hyperelastic and viscoelastic models presented above describe the behaviour of the solid matrix of soft tissues. As mentioned previously however, these tissues have a percentage of liquid that in the case of cartilage strongly influences its overall behaviour. Thus, although in other soft tissues this fluid phase can be neglected assuming the incompressibility assumption, in the case of cartilage, the fluid phase not only contributes to the distribution of the load but the free fluid flow also makes the tissue viscoelastic [50, 82, 116, 182]. Thus, the current models use for this tissue starts from the assumption that cartilage is composed of two phases and then biphasic models are needed.

It was not until the 80s when Mow et al. [130] proposed the biphasic theory based on the mixtures theory. In this theory, the tissue is modeled as a mixture of two different phases, both immiscible and incompressible: an elastic solid matrix and a non viscous fluid. Due to the intrinsic incompressibility of both phases, the dilatation of the tissue is supposed to be caused by the exudation or absorption of interstitial fluid. In the biphasic theory it is supposed that the stiffness due to the collagen fibers and proteoglycans is included in the elastic constants of the solid matrix. This model had an important success on the description of the experimental results corresponding to confined compression tests [23, 49, 101, 131, 132], although later experiments suggested some limitations for the interpretation of these experiments using those models.

The porous media models, such as the biphasic mixture theory of Mow et al. [130] or the electromechanical model of Frank and Grodzinsky [57] can appropriately explain the time-dependent viscoelastic response of cartilage as resulting primarily from the dissipative drag of interstitial fluid flowing through the porous solid matrix. Alternatively, Suh and Bai [189] were able to show successful data using a linear isotropic poroviscoelastic model firstly proposed by Mak [123] and also used by Setton et al. [173]. To complete these formulations, the mechanism of flow independent viscoelasticity in the solid matrix can be also taken into account. Recently, Pérez del Palomar and Doblaré [153] have developed a finite deformation biphasic model where the solid matrix is considered as transversely isotropic and hyperelastic, and where the incompressibility is treated accurately.

Recent theoretical analyses using triphasic or quadriphasic mixture theory (which includes the electrical charge of each constituent) have identified two important sources of electrical potential in the negatively charged articular cartilage: a diffusion potential resulting from the inhomogeneous distribution of the fixed charge density either strain induced or naturally occurring, and a streaming potential resulting from fluid flow within charged tissue [99, 107, 124, 135]. Recently, Chen et al. [31] have developed a triphasic theory for modelling the mechano-electrochemical phenomena of charged hydrated soft tissue extending it to finite deformation problems. These recent theoretical studies indicate that the charged nature of articular cartilage has a profound influence not only on the swelling and electric behaviors but also on mechanical behaviors as well, which has been reviewed above.

2.4 Active Response of Muscle Tissue

In previous sections, the behaviour of the muscle has been briefly explained. It was mentioned that it has a passive and an active response. The passive one is usually considered as a fibered hyperelastic material, and therefore, all the constitutive relations explained before can be directly applied. However, the active component responsible of the shortening of the muscles fibers determines its behaviour and needs to be described separately. Here, only a brief description of the models that are most used is presented.

Hill's model is the most famous equation in muscle mechanics [79] and is still the basis for most of the currently used models. Hill represented the muscle actuators as composed of three elements, as depicted in Fig. 4.

- One elastic element to account for the muscle elasticity in isometric conditions.

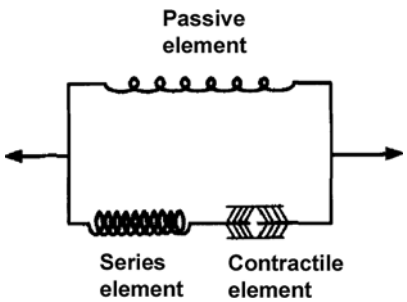

Fig. 4 Schematic representation of the 3D Hill model to account both the active and passive response of the muscle

- One contractile element, which is freely extensible at rest, but capable of shortening when activated.
- One elastic element placed in parallel with the two others to account for elasticity of the muscle at rest.

It has been recognized that the parallel element stands for the action of the intramuscular connective tissues surrounding the fibres and the series element has mainly been attributed to the intrinsic elasticity of the cross-bridges [117].

Some of the most interesting papers in this field are [93, 126, 210, 217]. These are phenomenological models, accounting for the length-force and the velocity-force relationship of the muscle.

Huxley [93] for instance presented a phenomenological model at different architectural levels. The basic theory focuses on an ensemble of myosin heads which are assumed to be capable of binding to actin, to form a cross-bridge. During contraction, a fraction of all cross-bridges is attached. Every attached crossbridge has its own dimensionless attachment length ξ. The distribution of attached cross-bridges with respect to their length is given by the function $n(\xi, t)$ and the rate of change of this distribution can be expressed with a modified two-state Huxley equation:

$$\frac{\partial n(\xi,t)}{\partial t} - u(t)\frac{\partial n(\xi,t)}{\partial \xi} = r(t) f(\xi)\big[\alpha - n(\xi,t)\big] - g(\xi) n(\xi,t) \tag{44}$$

where $u(t)$ is the scaled shortening velocity of a half sarcomere, $f(\xi)$ and $g(\xi)$ are the attachment and detachment rate of the cross-bridges, respectively, α is an overlap factor, and $r(t)$ is an activation factor, depending on the amount of calcium in the myofibrillar space. It should be noted at this point that (44) again is a partial differential equation with a time derivative and a derivative to the attachment length, which is a microstructural property. The shortening velocity $u(t)$ is a macroscopic property.

The active muscle stress can be determined from the distribution of attached cross-bridges n. It is assumed that the cross-bridge force depends linearly on the attachment length ξ. The active Cauchy stress $\boldsymbol{\sigma}_a$ generated by all cross-bridges in a slice of half sarcomeres is described as

$$\boldsymbol{\sigma}_a = c_a \lambda \int_{-\infty}^{\infty} \xi n(\xi,t)\, \mathrm{d}\xi = c_a \lambda Q_1(t) \tag{45}$$

where $Q_1(t)$ is the first moment of function $n(\xi, t)$, c_a is a material constant and represents the maximal isometric stress with the maximum number of cross-bridges attached and λ is the extension ratio in fiber direction [215, 216].

It is assumed that the total stress in the material is defined by a superposition of a passive stress (caused by the stiffness properties of collagen and cytoskeletal materials) and an active stress that works only in the fibre direction [140]. In mathematical terms this can be written as

$$\begin{aligned}\boldsymbol{\sigma} &= \boldsymbol{\sigma}_p + \boldsymbol{\sigma}_a \mathbf{e}_f \mathbf{e}_f \\ &= \boldsymbol{\sigma}_p^{\text{matrix}} + \boldsymbol{\sigma}_p^{\text{fiber}} \mathbf{e}_f \mathbf{e}_f + \boldsymbol{\sigma}_a \mathbf{e}_f \mathbf{e}_f\end{aligned} \tag{46}$$

where $\boldsymbol{\sigma}_p$ is the passive stress and $\mathbf{e}_f$ denotes the local fiber direction. In the most recent models, the passive stress $\boldsymbol{\sigma}_p$ is usually decoupled in matrix and fiber contribution [126, 140, 216].

2.5 Initial Strains

Initial strains are a consequence of the continuous growth, remodelling, damage and viscoelastic strains that suffer living materials along their whole life. Their most important aim is to homogenize the stress distribution at different stages of tissue deformation. For example, in arteries, their effect is to decrease the circumferential stresses at the inner wall and to reduce the stress gradient through the arterial thickness [28]. It has been assumed by different authors that the physiological state of a healthy artery requires constant circumferential stress in each layer. This situation is only possible by the presence of initial stresses [166]. In ligaments of diarthrodial joints, initial stretches provide joint stability even in a relatively unloaded joint configuration [63]. Typical residual strains are approximately 3–5% in these ligaments [12].

Initial strains can be relieved by selective cutting of the living tissue and removal of its internal constraints. Direct measurement of ligament stresses is very difficult, invasive and in most cases simply not available. Therefore, numerical estimations of the effect of these stress and strain distributions and the associate parametric study are useful for a better understanding of the mechanical behaviour of these organs under physiological and pathological conditions. This information is also important in the design of artificial grafts.

In order to describe the current deformation state of a solid, including the effect of initial deformations, three different configurations are usually defined: (a) the stress-free state (Ω_{sf}), (b) the reference state in which the material is unloaded (Ω_0) and (c) the current deformed state (Ω). It is assumed that the total deformation gradient tensor corresponding to the current state ($\mathbf{F}_r$) admits a multiplicative decomposition [205] such as:

$$\mathbf{F}_r = \mathbf{F}\mathbf{F}_0 \tag{47}$$

The initial stress in the reference state, $\boldsymbol{\sigma}_0$, is defined for hyperelastic materials in the standard form, by the strain-energy density function $\Psi_{\Omega_{\text{sf}}}$. Note that this function is always referred to the stress-free state Ω_{sf}, while $\boldsymbol{\sigma}_0$ are true

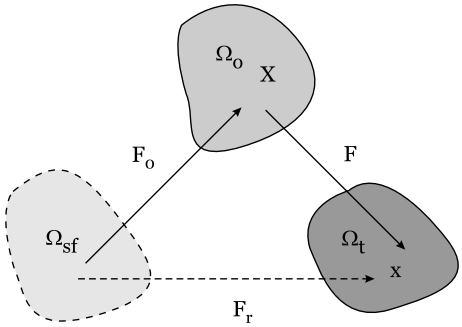

Fig. 5 Multiplicative decomposition of the total deformation gradient where Ω_{sf} denotes the stress free state, Ω_0 the reference state and Ω the current configuration [149]

stresses in the reference load-free configuration. Then

$$\boldsymbol{\sigma}_0 = \frac{2}{J_0}\boldsymbol{\chi}_*\left[\left.\frac{\partial \Psi_{\Omega_{sf}}(\mathbf{C})}{\partial \mathbf{C}}\right|_{\mathbf{C}=\mathbf{C}_0}\right] = \frac{2}{J_0}\mathbf{F}_0\left[\left.\frac{\partial \Psi_{\Omega_{sf}}(\mathbf{C})}{\partial \mathbf{C}}\right|_{\mathbf{C}=\mathbf{C}_0}\right]\mathbf{F}_0^T \tag{48}$$

with $\boldsymbol{\chi}_*$ the push-forward associated to $\mathbf{F}_0$ and $\mathbf{C}_0 = \mathbf{F}_0^T\mathbf{F}_0$.

In the same way, it is possible to define the total stresses corresponding to the current state $\boldsymbol{\sigma}_r$ in the standard form by using the strain-energy density function $\Psi_{\Omega_{sf}}$ through $\mathbf{F}_r$.

$$\boldsymbol{\sigma}_r = \frac{2}{J_r}\boldsymbol{\chi}_*\left[\left.\frac{\partial \Psi_{\Omega_{sf}}(\mathbf{C})}{\partial \mathbf{C}}\right|_{\mathbf{C}=\mathbf{C}_r}\right] = \frac{2}{J_r}\mathbf{F}_r\left[\left.\frac{\partial \Psi_{\Omega_{sf}}(\mathbf{C})}{\partial \mathbf{C}}\right|_{\mathbf{C}=\mathbf{C}_r}\right]\mathbf{F}_r^T \tag{49}$$

with $J_r = J_0 J$ and $\mathbf{C}_r = \mathbf{F}_r^T\mathbf{F}_r$.

Finally, the elasticity tensor in the material description

$$\mathbb{C} = 4\left.\frac{\partial^2 \Psi_{\Omega_{sf}}(\mathbf{C})}{\partial \mathbf{C}\partial \mathbf{C}}\right|_{\mathbf{C}=\mathbf{C}_r} \tag{50}$$

3 Finite Element Modeling

In this section the formulation of the biphasic theory under the frame of multiphasic systems is derived. First of all, the balance laws for multiphasic systems are presented, and then these are particularized for the case of two and one phase materials. Finally, some computational aspects that have to be taken into account are described.

3.1 Balance Laws of Multiphasic Systems

At this point, the unified model proposed by Garikipati et al. [64] is described in order to derive the constitutive equations for biphasic systems. The multiphasic solid $\mathcal{B}$ occupies the region $\Omega_0 \subset \mathbb{R}^3$ in the reference configuration. Points of $\mathcal{B}$

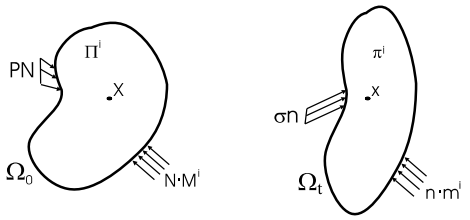

Fig. 6 Continuum tissue with diffusing species (Ω_0 undeformed configuration and Ω_t current configuration)

are parameterized by their coordinates in the reference configuration, $\boldsymbol{X}$. The deformation of $\mathcal{B}$ is denoted by the function $\boldsymbol{\varphi}(\boldsymbol{X}, t) \in \mathbb{R}^3$ (Fig. 6), in Ω_0, that makes correspond each point $\boldsymbol{X}$ its deformed position $\boldsymbol{x} = \boldsymbol{\varphi}(\boldsymbol{X}, t)$, at time $t \in [0, T]$. In each deformed configuration $\mathcal{B}$ occupies the opened region $\Omega_t = \boldsymbol{\varphi}(\Omega_0, t)$, $\Omega_t \subset \mathbb{R}^3$. The deformation gradient and the associated Jacobian are therefore defined as $\mathbf{F} = \partial\boldsymbol{\varphi}/\partial\boldsymbol{X}$ and $J = \det\mathbf{F}$, respectively.

The tissue is considered to be composed of different species. The solid phase is denoted by s, and the fluid phase by f. The remaining species, $\alpha, \ldots, \omega$, are precursors of the tissue or bioproducts coming from biochemical reactions inside it. The index i is used to indicate a specie. Each specie has sources/sinks of mass $\pi^\alpha, \ldots, \pi^\omega$ and fluxes of mass $\boldsymbol{m}^\alpha, \ldots, \boldsymbol{m}^\omega$ in the deformed configuration. We have to point out that the fluxes are defined relative to the solid phase. The solid phase is associated with possible sources and sinks and without mass fluxes ($\pi^s \neq 0, \boldsymbol{m}^s = \mathbf{0}$), while the fluid phase is only related to mass fluxes ($\pi^f = 0, \boldsymbol{m}^f \neq \mathbf{0}$). The solid phase does not undergo mass transport so its movement is uniquely determined by means of $\boldsymbol{\varphi}(\boldsymbol{X}, t)$. The remaining species are convective with respect to the solid and diffusive with it. Finally, we consider the whole system closed with respect to mass, that is, $\sum_i \pi^i = 0$.

The current concentration of the specie i, $\rho_0^i = \bar{\rho}^i\phi^i$, is defined as mass per unit of volume in Ω_0 and is expressed in terms of the intrinsic density $\bar{\rho}^i$ and the volume fraction ϕ^i. Therefore, density in the deformed configuration can be calculated by means of the deformation gradient as $\rho^i = \rho_0^i J^{-1}$. The tissue density is defined as $\rho_0 = \sum_i \rho_0^i$.

Balance of mass The concentrations, ρ_0^i, change due to mass transport and interconversion of species. The balance of mass in the deformed configuration is:

$$\frac{\mathrm{d}}{\mathrm{d}t}\int_{\varphi(v)} \rho^i \,\mathrm{d}V = \int_{\varphi(v)} \pi^i \,\mathrm{d}V - \int_{\partial\varphi(v)} \boldsymbol{m}^i \cdot \boldsymbol{n} \,\mathrm{d}S \quad \forall v \subset \Omega_0 \tag{51}$$

Applying the Leibnitz rule, the divergence theorem, and summing over all the species we get,

$$\frac{\mathrm{d}\rho}{\mathrm{d}t} = -\sum_i \operatorname{div} \boldsymbol{m}^i - \rho \operatorname{div} \boldsymbol{v} \tag{52}$$

where $\mathrm{d}/\mathrm{d}t$ is the material derivative, and $\boldsymbol{v}$ is the spatial velocity of the solid movement.

Balance of linear momentum The tissue is subjected to surface stresses $\boldsymbol{t}$ and body forces $\boldsymbol{g}$. We assume that $\boldsymbol{t} = \sum_i \boldsymbol{\sigma}^i \cdot \boldsymbol{n}$, where $\boldsymbol{\sigma}^i$ is the Cauchy stress tensor corresponding to specie i and the index runs over all species.

The solid has a material velocity field $\mathbf{V}(\mathbf{X}, t) = \partial \boldsymbol{\varphi}(\boldsymbol{X}, t)/\partial t$. Since fluxes are defined relative to the solid phase, the total spatial velocity of the solid phase is $\mathbf{v} = \mathbf{V} \circ \boldsymbol{\varphi}^{-1}$, and for each of the remaining species $\boldsymbol{v} + \boldsymbol{v}^i$, $(i = s, f, \alpha, \ldots, \omega)$, with the understanding that $\boldsymbol{v}^s = \mathbf{0}$ and $\boldsymbol{v}^i = (1/\rho^i)\boldsymbol{m}^i$.

The balance of linear momentum in the deformed configuration for each specie is:

$$\begin{aligned}
&\frac{\mathrm{d}}{\mathrm{d}t}\int_{\varphi(v)} \rho^i (\boldsymbol{v} + \boldsymbol{v}^i)\,\mathrm{d}V \\
&\quad = \int_{\varphi(v)} \rho^i (\boldsymbol{g} + \boldsymbol{q}^i)\,\mathrm{d}V + \int_{\varphi(v)} \pi^i (\boldsymbol{v} + \boldsymbol{v}^i)\,\mathrm{d}V \\
&\qquad + \int_{\partial\varphi(v)} \boldsymbol{\sigma}^i \cdot \boldsymbol{n}\,\mathrm{d}S - \int_{\partial\varphi(v)} (\boldsymbol{v} + \boldsymbol{v}^i)\boldsymbol{m}^i \cdot \boldsymbol{n}\,\mathrm{d}S \\
&\qquad \forall v \subset \Omega_0
\end{aligned} \tag{53}$$

with $\boldsymbol{q}^i$ the interaction force per unit mass between the specie i and the other species.

Summing (53) over all the species and comparing with the same equation but for the whole system, we get $\sum_i \rho^i \boldsymbol{q}^i = -\sum_i \pi^i \boldsymbol{v}^i$.

Finally, the local version of the linear momentum for one specie is:

$$\begin{aligned}
\rho^i \frac{\partial}{\partial t}(\boldsymbol{v} + \boldsymbol{v}^i) = \rho^i (\boldsymbol{g} + \boldsymbol{q}^i) + \operatorname{div} \boldsymbol{\sigma}^i \\
- \left[\nabla(\boldsymbol{v} + \boldsymbol{v}^i)\right] \cdot \boldsymbol{m}^i \\
- \rho^i \left[\nabla(\boldsymbol{v} + \boldsymbol{v}^i)\right] \cdot \boldsymbol{v}
\end{aligned} \tag{54}$$

Balance of angular momentum For the purely mechanical theory, balance of angular momentum implies that the Cauchy stress for each specie is symmetric: $\boldsymbol{\sigma}^i = \boldsymbol{\sigma}^{i^T}$ [64].

Balance of energy The internal energy per unit mass of the specie i is denoted by e^i, the heat supply to specie i per unit mass of that specie is r^i and the partial heat flux vector $\boldsymbol{f}^i_q$, defined on Ω. An interaction energy appears between species: the energy per unit mass of i, transferred to i by all other species is $\tilde{e}^i$. Therefore, the balance of energy for the specie i in integral form becomes:

$$\begin{aligned}
&\frac{\mathrm{d}}{\mathrm{d}t}\int_{\varphi(v)} \rho^i \left(e^i + \frac{1}{2}\|\boldsymbol{v} + \boldsymbol{v}^i\|^2\right)\mathrm{d}V \\
&\quad = \int_{\varphi(v)} \left[\rho^i \boldsymbol{g} \cdot (\boldsymbol{v} + \boldsymbol{v}^i) + \rho^i r^i\right]\mathrm{d}V \\
&\qquad + \int_{\varphi(v)} \rho^i \boldsymbol{q}^i \cdot (\boldsymbol{v} + \boldsymbol{v}^i)\,\mathrm{d}V \\
&\qquad + \int_{\varphi(v)} \left[\pi^i \left(e^i + \frac{1}{2}\|\boldsymbol{v} + \boldsymbol{v}^i\|^2\right) + \rho^i \tilde{e}^i\right]\mathrm{d}V \\
&\qquad + \int_{\partial\varphi(v)} \left[(\boldsymbol{v} + \boldsymbol{v}^i) \cdot \boldsymbol{\sigma}^i - \boldsymbol{m}^i \left(e^i + \frac{1}{2}\|\boldsymbol{v} + \boldsymbol{v}^i\|^2\right)\right. \\
&\qquad \left. - \boldsymbol{f}^i_q\right] \cdot \boldsymbol{n}\,\mathrm{d}S \quad \forall v \subset \Omega_0
\end{aligned} \tag{55}$$

Summing over all the species and taking into account the balance of energy of the complete system with its environment, the energy balance equation on the deformed configuration is:

$$\begin{aligned}
&\sum_i \rho^i \frac{\mathrm{d}e^i}{\mathrm{d}t} \\
&\quad = \sum_i \left[\boldsymbol{\sigma}^i : \nabla(\boldsymbol{v} + \boldsymbol{v}^i) - \boldsymbol{m}^i \cdot \nabla e^i - \operatorname{div} \boldsymbol{f}^i_q\right] \\
&\qquad - \sum_i \left[\rho^i \boldsymbol{q}^i \cdot \boldsymbol{v}^i + \pi^i \left(e^i + \frac{1}{2}\|\boldsymbol{v}^i\|^2\right) - \rho^i r^i\right]
\end{aligned} \tag{56}$$

Clausius–Duhem inequality Let ϑ^i the entropy per unit mass of specie i in the deformed configuration and θ the absolute temperature. The entropy inequality can be written as,

$$\begin{aligned}
&\sum_i \frac{\mathrm{d}}{\mathrm{d}t}\int_{\varphi(v)} \rho^i \vartheta^i\,\mathrm{d}V \\
&\quad \geq \sum_i \int_{\varphi(v)} \left(\pi^i \vartheta^i + \frac{\rho^i r^i}{\theta}\right)\mathrm{d}V \\
&\qquad - \sum_i \int_{\partial\varphi(v)} \left(\vartheta^i \boldsymbol{m}^i + \frac{\boldsymbol{f}^i_q}{\theta}\right) \cdot \boldsymbol{n}\,\mathrm{d}S \quad \forall v \subset \Omega_0
\end{aligned} \tag{57}$$

Applying the Leibnitz rule, the divergence theorem, using the balance of mass and introducing the Helmholtz' free energy $\psi^i = e^i - \theta\vartheta^i$, the Clausius–Duhem inequality in the deformed configuration becomes,

$$\begin{aligned}
&\sum_i \left[\rho^i \left(\frac{\mathrm{d}\psi^i}{\mathrm{d}t} + \vartheta^i \frac{\mathrm{d}\theta}{\mathrm{d}t}\right) - \boldsymbol{\sigma}^i : \nabla(\boldsymbol{v} + \boldsymbol{v}^i)\right. \\
&\quad + \boldsymbol{m}^i \cdot (\nabla\psi^i + \vartheta^i \nabla\theta) + \frac{1}{\theta}\boldsymbol{f}^i_q \cdot \nabla\theta + \rho^i \boldsymbol{q}^i \cdot \boldsymbol{v}^i \\
&\quad \left. + \pi^i \left(\psi^i + \theta\vartheta^i + \frac{1}{2}\|\boldsymbol{v}^i\|^2\right)\right] \leq 0
\end{aligned} \tag{58}$$

Additionally, for a saturated tissue, $\sum_i \phi^i = \sum_i (\rho^i/\bar{\rho}^i) = 1$ must be satisfied. Introducing this restriction in the definition of the total free energy by means of a Lagrange multiplier, p, yields

$$W = J \sum_i \rho^i \bar{\psi}^i + pJ\left(1 - \sum_i \frac{\rho^i}{\bar{\rho}^i}\right) \tag{59}$$

where $W = W(\mathbf{F}, \theta)$ is the free energy of the tissue, $\bar{\psi}^i = \bar{\psi}^i(\mathbf{F}, \theta)$ stands for the free energy per unit mass of each specie. Therefore, introducing the mass balance equation, and making some algebraic manipulations, the inequality (58) turns:

$$\begin{aligned}
&\left(\frac{\partial W}{\partial \mathbf{F}} \cdot \mathbf{F}^T - J\boldsymbol{\sigma}^s - Jp\frac{\rho^s}{\bar{\rho}^s}\mathbf{1}\right) : \nabla \boldsymbol{v} \\
&\quad + \left(\frac{\partial W}{\partial \theta} + J\sum_i \rho^i \vartheta^i\right)\frac{\mathrm{d}\theta}{\mathrm{d}t} \\
&\quad + J\sum_i \left[\left(\rho^i \psi^i \mathbf{1} - \boldsymbol{\sigma}^i - p\frac{\rho^i}{\bar{\rho}^i}\mathbf{1}\right) : \nabla \boldsymbol{v}^i\right] \\
&\quad + J\sum_i \pi^i \left(\theta\vartheta^i + \frac{1}{2}\|\boldsymbol{v}^i\|^2 + \frac{p}{\bar{\rho}^i}\right) \\
&\quad + J\sum_i \left[\boldsymbol{v}^i \cdot \left(\nabla(\rho^i\psi^i) + \rho^i\vartheta^i\nabla\theta + \rho^i \boldsymbol{q}^i - p\nabla\frac{\rho^i}{\bar{\rho}^i}\right)\right] \\
&\quad + J\sum_i \left[\frac{1}{\theta}\boldsymbol{f}_q^i \cdot \nabla\theta\right] \\
&\quad - \left(1 - \sum_i \frac{\rho^i}{\bar{\rho}^i}\right)\frac{\mathrm{d}}{\mathrm{d}t}(pJ) \leq 0
\end{aligned} \tag{60}$$

3.1.1 Application to Biphasic Soft Tissues

In this case, the tissue is composed of only two constituents: a solid phase and a liquid phase, so $i = s, f$. Assuming that the tissue is saturated and denoting by $\phi^s = \rho^s/\bar{\rho}^s$ the solid volume fraction and $\phi^f = \rho^f/\bar{\rho}^f$ the fluid volume fraction, we have that $\phi^s + \phi^f = 1$. Note that the particularization to only one phase would be immediate to obtain using the following equations without the contribution of the fluid phase.

Therefore, the tissue density in the deformed configuration $\rho = \rho(t)$ is,

$$\rho = \phi^s\bar{\rho}^s + \phi^f\bar{\rho}^f = \rho^s + \rho^f \tag{61}$$

where $\bar{\rho}^s$ and $\bar{\rho}^f$ are the intrinsic density of the solid and fluid phases respectively. Assuming that there is no generation of mass, the balance of mass for both phases becomes:

$$\frac{\mathrm{d}(\phi^s\bar{\rho}^s)}{\mathrm{d}t} = -\bar{\rho}^s\phi^s \operatorname{div}\boldsymbol{v}^s \tag{62}$$

$$\frac{\mathrm{d}(\phi^f\bar{\rho}^f)}{\mathrm{d}t} = -\bar{\rho}^f\phi^f \operatorname{div}\boldsymbol{v}^s - \operatorname{div}\boldsymbol{m}^f \tag{63}$$

where $\boldsymbol{v}^s$ corresponds to the absolute velocity of the solid phase (note that we have changed the previous notation $\boldsymbol{v}$ by $\boldsymbol{v}^s$ and $\boldsymbol{v}^f$ by $(\boldsymbol{v}^s - \boldsymbol{v}^f)$ being now $\boldsymbol{v}^f$ the absolute velocity of the fluid. These will be the chosen variables in the development of the following formulation).

Making use of the relation $\boldsymbol{m}^f = -\rho^f(\boldsymbol{v}^s - \boldsymbol{v}^f) = -\phi^f\bar{\rho}^f(\boldsymbol{v}^s - \boldsymbol{v}^f)$, the solid and fluid phases can be obtained:

$$\frac{\mathrm{d}\phi^s}{\mathrm{d}t} = -\phi^s \operatorname{div}\boldsymbol{v}^s \tag{64}$$

$$\frac{\mathrm{d}\phi^f}{\mathrm{d}t} = -\phi^f \operatorname{div}\boldsymbol{v}^s + \operatorname{div}(\phi^f\boldsymbol{v}^s - \phi^f\boldsymbol{v}^f) \tag{65}$$

Summing (64) and (65) and using the saturation condition we have:

$$\operatorname{div}(\phi^s\boldsymbol{v}^s + \phi^f\boldsymbol{v}^f) = 0 \tag{66}$$

which is the continuity equation for a biphasic mixture [83, 130–132].

The volume fractions of the solid and fluid phases in the deformed configuration can be expressed as,

$$\phi_0^\alpha = J^\alpha\phi^\alpha \quad \alpha = s, f \tag{67}$$

and taking into account that the fluid is considered to be convective with the solid phase, the Jacobian of the fluid phase can be related to the one of the solid through the saturation condition as,

$$\frac{1}{J^f} = \frac{1}{J^s} + \frac{1}{\phi_0^f}\left(1 - \frac{1}{J^s}\right) \tag{68}$$

Assuming that, there is no mass generation $\pi^i = 0$, the temperature is uniform $\nabla\theta = 0$, the process is adiabatic, $\boldsymbol{f}_q^i = 0$, and the fluid phase is fully incompressible, (60) must be satisfied for all thermodynamically possible processes, therefore, following standard arguments in Continuum Mechanics, we can state:

$$\begin{aligned}
&J\sum_i \rho^i\vartheta^i = -\frac{\partial W}{\partial\theta}, \quad i = s, f, \\
&\boldsymbol{\sigma}^f = -p\phi^f\boldsymbol{I}, \\
&\boldsymbol{\sigma}^s = \rho^s J^{-1}\frac{\partial W}{\partial \mathbf{F}} \cdot \mathbf{F}^T - p\phi^s\boldsymbol{I}, \\
&\phi^s + \phi^f = 1, \\
&(\boldsymbol{v}^s - \boldsymbol{v}^f) \cdot (-p\nabla\phi^f + \rho^f\boldsymbol{q}^f) \leq 0
\end{aligned} \tag{69}$$

Remember that $J = J^s$ since we have identified the movement and deformation gradient with those of the solid phase.

The last relation and $\rho^s \boldsymbol{q}^s + \rho^f \boldsymbol{q}^f = 0$ are fulfilled if we choose the phenomenological relations:

$$\begin{aligned} \rho^f \boldsymbol{q}^f &= -\boldsymbol{K} \cdot (\boldsymbol{v}^f - \boldsymbol{v}^s) + p \nabla \phi^f \\ \rho^s \boldsymbol{q}^s &= -\rho^f \boldsymbol{q}^f = \boldsymbol{K} \cdot (\boldsymbol{v}^f - \boldsymbol{v}^s) + p \nabla \phi^s \end{aligned} \tag{70}$$

where $\boldsymbol{K}$ is a positive definite second order tensor, usually known as diffusive drag coefficient.

Finally, the equilibrium equations for a biphasic solid can be written as,

$$\begin{aligned} \nabla \cdot \boldsymbol{\sigma}_e^s - \phi^s \nabla p - \boldsymbol{K} \cdot (\boldsymbol{v}^s - \boldsymbol{v}^f) = 0 \\ -\phi^f \nabla p + \boldsymbol{K} \cdot (\boldsymbol{v}^s - \boldsymbol{v}^f) = 0 \end{aligned} \tag{71}$$

where $\boldsymbol{\sigma}_e^s$ is usually known as effective stress. These equations are the same as those proposed by Mow et al. [130], and used by others [4, 188], but they have been obtained from a different approach.

3.2 Weak Form of the Biphasic Mixture Equations

Let $\delta \boldsymbol{\chi}^s$ and $\delta \boldsymbol{\chi}^f$, be arbitrary admissible variations of the displacements associated to the solid and fluid phases respectively, which are Sobolev functions of first order over Ω, and take null values on Γ_h^s and Γ_h^f being these the parts of the boundary of Ω, Γ, where solid displacements and fluid velocities are imposed, respectively. The weak form of the equilibrium equations (71) can be obtained from a standard weighted residual approach as:

$$\begin{aligned} &\int_\Omega \delta \boldsymbol{\chi}^s \cdot \left[\operatorname{div} \boldsymbol{\sigma}_e^s - \phi^s \nabla p - \boldsymbol{K} (\boldsymbol{v}^s - \boldsymbol{v}^f) \right] \mathrm{d}v \\ &\quad + \int_\Omega \delta \boldsymbol{\chi}^f \cdot \left[-\phi^f \nabla p + \boldsymbol{K} (\boldsymbol{v}^s - \boldsymbol{v}^f) \right] \mathrm{d}v = 0 \end{aligned} \tag{72}$$

Applying the divergence theorem to (72), we obtain for a biphasic mixture:

$$\begin{aligned} &G(\boldsymbol{u}^s, \boldsymbol{u}^f; \delta \boldsymbol{\chi}^s, \delta \boldsymbol{\chi}^f) \\ &= \int_\Omega (\nabla^{sym} \delta \boldsymbol{\chi}^s)^T : \boldsymbol{\sigma}_e^s \, \mathrm{d}v - \int_\Omega \operatorname{div}(\phi^s \delta \boldsymbol{\chi}^s) p \, \mathrm{d}v \\ &\quad + \int_\Omega \delta \boldsymbol{\chi}^s \cdot \boldsymbol{K} (\boldsymbol{v}^s - \boldsymbol{v}^f) \, \mathrm{d}v \\ &\quad - \int_\Omega \operatorname{div}(\phi^f \delta \boldsymbol{\chi}^f) p \, \mathrm{d}v \\ &\quad - \int_\Omega \delta \boldsymbol{\chi}^f \cdot \boldsymbol{K} (\boldsymbol{v}^s - \boldsymbol{v}^f) \, \mathrm{d}v - \int_{\Gamma_{t^s}} \delta \boldsymbol{\chi}^s \cdot \bar{\boldsymbol{t}}^s \, \mathrm{d}a \\ &\quad + \int \bar{p} f \cdot (\delta \boldsymbol{\chi}^f \cdot \boldsymbol{n}) \, \mathrm{d}a = 0 \end{aligned} \tag{73}$$

3.2.1 *Augmented Lagrangian Method for Incompressible Response*

Traditionally, in order to solve the incompressibility condition in biphasic formulations, the continuity equation is penalized in such a way that the pressure is eliminated from the formulation [4, 6, 186, 188]. Therefore, considering β as the penalty parameter, the continuity equation is replaced by,

$$\operatorname{div}(\phi^s \boldsymbol{v}^s + \phi^f \boldsymbol{v}^f) + \frac{p}{\beta} = 0 \tag{74}$$

Other possibility is to force the incompressibility condition for the tissue by means of an Augmented Lagrangian Method [53, 55, 65, 121, 181]. This combines penalty functions and local duality. In this method, the system is solved for a load step with a relatively compressible material. Next, the penalty parameter is increased incrementally, forcing the incompressibility. With an appropriate update scheme of the variables, this method leads to a stable algorithm. The new functional is then defined as:

$$L(\boldsymbol{u}^s, \boldsymbol{u}^f, p; \lambda) = \Pi(\boldsymbol{u}^s, \boldsymbol{u}^f, p) + \int_\Omega \lambda h \, \mathrm{d}v \tag{75}$$

where h is a function of the constraint, the continuity equation in this case, that becomes zero when the material is incompressible and λ is the Lagrange multiplier.

An important advantage of this method is that allows to find the value of the parameters (λ and β) incrementally and to use different values of the parameter in the mesh, avoiding the introduction of high penalty parameters in those zones where they are not necessary.

Collecting all terms in (73), the weak form of the problem can be written as:

$$\begin{aligned} &G(\boldsymbol{u}^s, \boldsymbol{u}^f; \delta \boldsymbol{\chi}^s, \delta \boldsymbol{\chi}^f) \\ &\quad = G_s(\boldsymbol{u}^s; \delta \boldsymbol{\chi}^s) + G_{\text{Drag}}(\boldsymbol{u}^s, \boldsymbol{u}^f; \delta \boldsymbol{\chi}^s, \delta \boldsymbol{\chi}^f) \\ &\qquad + G_{\text{Aug}}(\boldsymbol{u}^s, \boldsymbol{u}^f; \delta \boldsymbol{\chi}^s, \delta \boldsymbol{\chi}^f) \\ &\qquad + g_{\text{ext}}(\bar{\boldsymbol{t}}^s \cdot \bar{p}^f; \delta \boldsymbol{\chi}^s, \delta \boldsymbol{\chi}^f) \end{aligned} \tag{76}$$

where,

$$G_s(\boldsymbol{u}^s; \delta \boldsymbol{\chi}^s) = \int_\Omega (\nabla^{\text{sym}} \delta \boldsymbol{\chi}^s)^T : \boldsymbol{\sigma}_e^s \, \mathrm{d}v \tag{77}$$

$$\begin{aligned} &G_{\text{Drag}}(\boldsymbol{u}^s, \boldsymbol{u}^f; \delta \boldsymbol{\chi}^s, \delta \boldsymbol{\chi}^f) \\ &\quad = \int_\Omega \delta \boldsymbol{\chi}^s \cdot \boldsymbol{K} (\boldsymbol{v}^s - \boldsymbol{v}^f) \, \mathrm{d}v \\ &\qquad - \int_\Omega \delta \boldsymbol{\chi}^f \cdot \boldsymbol{K} (\boldsymbol{v}^s - \boldsymbol{v}^f) \, \mathrm{d}v \end{aligned} \tag{78}$$

$$G_{\text{Aug}}(\boldsymbol{u}^s, \boldsymbol{u}^f; \delta\boldsymbol{\chi}^s, \delta\boldsymbol{\chi}^f) = \int_\Omega \operatorname{div}(\phi^s \delta\boldsymbol{\chi}^s)\big[\lambda + \beta \operatorname{div}(\phi^s \boldsymbol{v}^s + \phi^f \boldsymbol{v}^f)\big]\,\mathrm{d}v + \int_\Omega \operatorname{div}(\phi^f \delta\boldsymbol{\chi}^f)\big[\lambda + \beta \operatorname{div}(\phi^s \boldsymbol{v}^s + \phi^f \boldsymbol{v}^f)\big]\,\mathrm{d}v \quad (79)$$

$$g_{\text{ext}}(\boldsymbol{u}^s; \delta\boldsymbol{\chi}^s, \delta\boldsymbol{\chi}^f) = \int_{\Gamma_{tf}} \bar{p} f (\delta\boldsymbol{\chi}^f \cdot \mathbf{n})\,\mathrm{d}a - \int_{\Gamma_{ts}} \delta\boldsymbol{\chi}^s \cdot \overline{\boldsymbol{t}}^s\,\mathrm{d}\Gamma \quad (80)$$

Since Ω and Γ in the above weighted residual statement correspond to the current configuration, they are time-dependent and, therefore, unknown. A Total Lagrangian formulation can be used, where the integrals in (76) are referred to the reference configuration at initial time $t = 0$ using the well-known expressions:

$$\mathrm{d}v = J\,\mathrm{d}v_0 \quad \text{and} \quad \boldsymbol{n}\mathrm{d}a = J\boldsymbol{n}_0 \cdot \mathbf{F}^{-1}\mathrm{d}a_0 \quad (81)$$

where $J = \det\mathbf{F}$, and the superscript s of the Jacobian has been dropped out for simplicity.

In the case of monophasic tissue such as the ligament, where only the solid phase is considered, all the terms including superindex f must be removed.

3.3 Computational Aspects

3.3.1 Incremental and Time Evolution Algorithms

Typically, in an incremental nonlinear finite element approach, the solution at time t, $\boldsymbol{u}_n$ is known and we seek the solution at the next time increment $t + \Delta t$, $\boldsymbol{u}_{n+1} = \boldsymbol{u}_n + \Delta\boldsymbol{u}$, where we have dropped the reference to the step in $\Delta\boldsymbol{u}$ to simplify the notation. If a linear one-step implicit integrator is used as in many applications [90], the velocity may be written in terms of the displacement increment as:

$$\boldsymbol{v}_{n+1} = f(\boldsymbol{v}_n, \Delta\boldsymbol{u}) \quad (82)$$

For Newton approaches, the derivative of the different variables with respect to the incremental displacement is needed. Thus, each component of the movement is uncoupled, we can write:

$$\frac{\delta\boldsymbol{v}_n}{\delta\Delta\boldsymbol{u}_{n+1}} = \frac{\delta f}{\delta\Delta\boldsymbol{u}_{n+1}} = \eta \quad (83)$$

where η is a scalar.

3.3.2 Integration Algorithm for the Visco-Hyperelastic Model

The basic idea in the numerical integration of the constitutive equations is to evaluate the convolution integral in (41) through a recursive relation. A related procedure was first suggested by Herrmann and Peterson [77] and modified by Simo [180]. The key idea is to transform the convolution representation discussed in previous section into a two-step recursive formula involving internal variables stored at the quadrature points of a finite-element mesh [177].

We introduce the following internal algorithmic history variables can be introduced,

$$\mathbf{H}^{(ij)} = \int_{-\infty}^{t} \exp\left[\frac{-(t-s)}{\tau_{ij}}\right]\frac{\mathrm{d}}{\mathrm{d}s} \times \left\{\operatorname{dev}\left[2\delta\bar{\Psi}^{0(j)}(\bar{\mathbf{C}}, \mathbf{m}_0, \mathbf{n}_0)(s)\right]\right\}\mathrm{d}s \quad (84)$$

Let $[t_0, T] \subset \mathbb{R}$, with $t_0 < T$, be the time interval of interest. Without loss of generality, t_0 can be taken $-\infty$. Further, let $[t_0, T] = \bigcup_{n\in\mathbb{I}}[t_n, t_{n+1}]$, be a partition of the interval $[t_0, T]$ with $\mathbb{I}$ an appropriate subset of the natural numbers and $\Delta t_n = t_{n+1} - t_n$ the associated time increment. From an algorithmic standpoint, the problem is defined in the usual strain-driven format and it can be assumed that at certain times t_n and t_{n+1} all relevant kinematic quantities are known.

Using the semigroup property of the exponential function, the property of additivity of the integral over the interval of integration and the midpoint rule to approximate the integral over $[t_n, t_{n+1}]$ one can arrive to the update formula [177]

$$\mathbf{H}^{(ij)}_{n+1} = \exp\left[\frac{-\Delta t_n}{\tau_{ij}}\right]\mathbf{H}^{(ij)}_n + \exp\left[\frac{-\Delta t_n}{2\tau_{ij}}\right]\left(\bar{\mathbf{S}}^{0(j)}_{n+1} - \bar{\mathbf{S}}^{0(j)}_n\right) \quad (85)$$

where $\bar{\mathbf{S}}^{0(j)}_{n+1} = \operatorname{dev}[2\delta\bar{\Psi}^{0(j)}(\bar{\mathbf{C}}, \mathbf{m}_0, \mathbf{n}_0)(s)]$ is the term of the initial stress response corresponding to I_j, i.e., $\bar{\mathbf{S}}^{0(1)}_{n+1}$ and $\bar{\mathbf{S}}^{0(2)}_{n+1}$ are due to the matrix material and $\bar{\mathbf{S}}^{0(4)}_{n+1} \ldots \bar{\mathbf{S}}^{0(9)}_{n+1}$ are due to the two families of fibers, see (13).

Following the convolution representation (41), the algorithmic approximation for the second Piola–Kirchhoff stress takes the form

$$\mathbf{S}_{n+1} = J_{n+1}\, p_{n+1}\mathbf{C}^{-1}_{n+1} + J^{-\frac{2}{3}}_{n+1}\sum_{j=1,j\neq 3}^{9}\left[\left(1 - \sum_{i=1}^{n}\gamma_{ij}\right)\bar{\mathbf{S}}^{0(j)}_{n+1}\right] + J^{-\frac{2}{3}}_{n+1}\sum_{j=1,j\neq 3}^{9}\sum_{i=1}^{n}\left[\gamma_{ij}\left\{\operatorname{dev}\left[\mathbf{H}^{(ij)}_{n+1}\right]\right\}\right] \quad (86)$$

Also, the Cauchy stress tensor can be calculated as:

$$\boldsymbol{\sigma}_{n+1} = p_{n+1}\mathbf{1} + \frac{1}{J_{n+1}}\sum_{j=1,j\neq 3}^{9}\left[\left(1 - \sum_{i=1}^{n}\gamma_{ij}\right)\operatorname{dev}\left\{\bar{\mathbf{F}}_{n+1}\left[2\frac{\partial\bar{\Psi}^{0(j)}(\bar{\mathbf{C}}_{n+1}, \mathbf{m}_0, \mathbf{n}_0)}{\partial\bar{\mathbf{C}}}\right]\bar{\mathbf{F}}^T_{n+1}\right\}\right]$$

$$+\frac{1}{J_{n+1}}\sum_{j=1,j\neq 3}^{9}\sum_{i=1}^{n}\Big[\gamma_{ij}\Big\{\mathrm{dev}\big[\bar{\mathbf{F}}_{n+1}\big[\mathbf{H}_{n+1}^{(ij)}\big]\times\bar{\mathbf{F}}_{n+1}^{T}\big]\Big\}\Big] \tag{87}$$

In order to obtain an easier recursive update procedure, the update formula (85) can be rewritten as in [177]

$$\tilde{\mathbf{H}}_{n}^{(ij)}=\exp\left[\frac{-\Delta t_n}{\tau_{ij}}\right]\mathbf{H}_{n}^{(ij)}-\exp\left[\frac{-\Delta t_n}{2\tau_{ij}}\right]\bar{\mathbf{S}}_{n}^{0(j)} \tag{88}$$

$$\mathbf{H}_{n+1}^{(ij)}=\tilde{\mathbf{H}}_{n}^{(ij)}+\exp\left[\frac{-\Delta t_n}{2\tau_{ij}}\right]\bar{\mathbf{S}}_{n+1}^{0(j)} \tag{89}$$

With this notation

$$\mathbf{S}_{n+1}=J_{n+1}p_{n+1}\mathbf{C}_{n+1}^{-1}+J_{n+1}^{-\frac{2}{3}}\sum_{j=1,j\neq 3}^{9}\left[(1-\gamma_j+\nu_j)\bar{\mathbf{S}}_{n+1}^{0(j)}+\sum_{i=1}^{n}\gamma_{ij}\Big\{\mathrm{dev}\big[\tilde{\mathbf{H}}_{n}^{(ij)}\big]\Big\}\right] \tag{90}$$

$$\boldsymbol{\sigma}_{n+1}=p_{n+1}\mathbf{1}+\sum_{j=1,j\neq 3}^{9}\Big[(1-\gamma_j+\nu_j)\,\mathrm{dev}\big[\boldsymbol{\sigma}_{n+1}^{0(j)}\big]+\frac{1}{J_{n+1}}\sum_{i=1}^{n}\gamma_{ij}\Big\{\mathrm{dev}\big[\tilde{\mathbf{h}}_{n}^{(ij)}\big]\Big\}\Big] \tag{91}$$

where $\gamma_j=\sum_{i=1}^{n}\gamma_{ij}$ and $\nu_j=\sum_{i=1}^{n}\gamma_{ij}\exp[\frac{-\Delta t_n}{2\tau_{ij}}]$. Note that $\tilde{\mathbf{H}}_{n}^{(ij)}$ is a constant at time t_{n+1} in the linearization process.

Using (16) and (90) we obtain

$$\mathbb{C}_{n+1}=\mathbb{C}_{\mathrm{vol}\,n+1}^{0}+\sum_{j=1,j\neq 3}^{9}\left[(1-\gamma_j+\nu_j)\bar{\mathbb{C}}_{n+1}^{0(j)}-\frac{2}{3}J_{n+1}^{-\frac{4}{3}}\sum_{i=1}^{n}\gamma_{ij}\left\{\mathrm{dev}\big[\tilde{\mathbf{H}}_{n}^{(ij)}\big]\otimes\bar{\mathbf{C}}_{n+1}^{-1}+\bar{\mathbf{C}}_{n+1}^{-1}\otimes\mathrm{dev}\big[\tilde{\mathbf{H}}_{n}^{(ij)}\big]-\big(\tilde{\mathbf{H}}_{n}^{(ij)}:\bar{\mathbf{C}}\big)\left(\mathbb{I}_{\boldsymbol{C}_{n+1}}^{-1}-\frac{1}{3}\bar{\mathbf{C}}_{n+1}^{-1}\otimes\bar{\mathbf{C}}_{n+1}^{-1}\right)\right\}\right] \tag{92}$$

and the spatial tangent modulus defined in (21) takes the form

$$c_{n+1}=c_{\mathrm{vol}\,n+1}^{0}+\sum_{j=1,j\neq 3}^{9}\left[(1-\gamma_j+\nu_j)\bar{\mathbb{C}}_{n+1}^{0(j)}-\frac{2}{3J_{n+1}}\sum_{i=1}^{n}\gamma_{ij}\left\{\mathrm{dev}\big[\tilde{\mathbf{h}}_{n}^{(ij)}\big]\otimes\mathbf{1}+\mathbf{1}\otimes\mathrm{dev}\big[\tilde{\mathbf{h}}_{n}^{(ij)}\big]-\mathrm{tr}\big[\tilde{\mathbf{h}}_{n}^{(ij)}\big]\left(\mathbb{I}-\frac{1}{3}\mathbf{1}\otimes\mathbf{1}\right)\right\}\right] \tag{93}$$

where $\tilde{\mathbf{h}}_{n}^{(ij)}=\bar{\mathbf{F}}_{n+1}\tilde{\mathbf{H}}_{n}^{(ij)}\bar{\mathbf{F}}_{n+1}^{T}$.

3.3.3 Numerical Treatment of Initial Strains

The main objective of this section is to discuss different methodologies to enforce initial strains in living soft tissues commented in the previous section, and more specifically in knee ligaments [149]. Two of these possible methodologies are:

- Stress-free Reference Configuration (SFRC): It corresponds to a Total Lagrangian Approach where the initial deformation product $\mathbf{F}_0$ is computed in an initial deformation step from a known stress-free state. The subsequent configurations are all referred to this stress-free state.
- Deformed Reference Configuration (DRC): It is related with an Updated Lagrangian Approach. In this case, initial strains $\mathbf{F}_0$ are enforced by defining an appropriate "deformation" field in the current configuration that, after an additional auto-equilibrium step, leads to a balanced initial state. The next configurations were then referred to this latter reference geometry.

The SFRC methodology implies to know the stress-free configuration. This is actually an idealized state since, as noted by Fung [59], it is practically impossible the existence of a configuration with zero stress at every point of a soft tissue. The compatibility constraints to maintain continuity between different parts of the tissue with different constitutive properties generate these internal stresses.

In addition, the "extraction" of this idealized stress-free configuration "in vivo" is almost impossible. Possibly, the best approximation is to obtain it from a fresh-frozen specimen by dissecting it from its attachments. Another further difficulty corresponds to the viscoelastic behaviour of most soft tissues. When ligaments, for instance, are dissected, an instantaneous elastic recovery takes place. This, however, does not correspond to the stress-free configuration. Initial stresses computed with this configuration underestimate the real ones. On the contrary, if the configuration obtained after the complete viscoelastic recovery is considered as the stress-free state, stresses computed after a purely elastic step from this configuration overestimate the actual ones. This methodology was used by Hirokawa

et al. [81] for the finite element simulation of the ACL deformation. In their work, in order to obtain the stress-free configuration, the ligament of a fresh-frozen specimen was dissected of its attachments and the resulting state was considered as the stress-free configuration. They modelled the ligament as a hyperelastic material. Normally, this strategy requires remeshing steps and the corresponding projections of the current results, making finite element formulations ineffective and inaccurate without additional improvements [21].

A way to overcome these drawbacks is to refer the problem to the zero-load reference configuration. In this case it is assumed that the initial strain distribution is known. This information can be obtained from experiments, but the associated process is usually very laborious. The real strain distribution of the specimen is three-dimensional and heterogenous and direct measures are very complex. However, some type of approximation is always possible.

In the DRC technique, $\mathbf{F}_0$ represents in general, an incompatible strain field, corresponding to the map from the two idealized configurations Ω_{sf} to Ω_0 (initial strains), and $\mathbf{F}$ the deformation gradient that results after application of the external loads to the reference configuration Ω_0. Usually $\mathbf{F}_0$ is not a real deformation gradient tensor because it does not arise from a displacement field. As noted, $\mathbf{F}_0$ is difficult to determine from experiments. In the case of ligaments and tendons, Gardiner et al. [63] proposed a relatively easy form to measure length variations along the fiber direction at different points, that is, $\mathbf{F}_0$ corresponds to an axial stretch λ_0 along the fiber direction $\mathbf{a}_0$ in the reference state Ω_0 that in ligaments closely follows the direction of maximal length. The concomitant contraction in the perpendicular plane is dictated by incompressibility, usual assumption in biological soft tissues.

In a coordinate system (*) where the fiber direction $\mathbf{a}_0$ is aligned with the X_1 axis, $\mathbf{F}_0$ can be written as:

$$\left[\mathbf{F}_0^*\right] = \begin{bmatrix} \lambda_0 & 0 & 0 \\ 0 & \frac{1}{\sqrt{\lambda_0}} & 0 \\ 0 & 0 & \frac{1}{\sqrt{\lambda_0}} \end{bmatrix} \tag{94}$$

and transformed to the global systems:

$$\mathbf{F}_0 = \mathbf{R}\mathbf{F}_0^* \tag{95}$$

with $\mathbf{R}$ the rotation tensor from this local system to the global one.

To introduce initial strains into the finite element formulation by the DRC technique, it is necessary to specify $\mathbf{F}_0$ pointwise within the finite element mesh. An equilibrium step is firstly applied with zero forces with the constitutive behaviour defined by $\Psi_{\Omega_{\text{sf}}}$ in order to obtain a balanced, although not fully compatible configuration. A second load step will result in the deformation gradient $\mathbf{F}$ that balances the externally applied forces.

Due to their non-linear behavior and the non-uniform distribution of the residual stresses, a wrong inclusion of the initial strain state in computational models of soft tissues can lead to important errors.

3.3.4 Numerical Treatment of the Incompressibility

A full Newton–Raphson approach in each load increment, with the update algorithm of the Lagrange multiplier and penalty parameter proposed by Powell [161] can be chosen to enforce the incompressibility, see Sect. 3.2.1.

The iterative Newton–Raphson scheme in each Δt with the update procedure both for Lagrange multiplier λ and the penalty parameter β is schematically shown in Table 1. It can be observed that if the maximum value of the constraint is larger than the parameter ξ, only the penalization should be updated, while if this value is smaller than ξ, then the Lagrange multiplier is updated to guarantee optimality, reducing the value of ξ to ensure convergence. The values of β and λ remain constant during the Newton–Raphson iterations keeping the quadratic convergence of the method.

Table 1 Augmented Lagrangian scheme for the incompressibility treatment

Let h be $h = \max_{e=1,N_e}\{h_e\} = \max_{e=1,N_e}\{\nabla\cdot(\phi_e^s \boldsymbol{v}_e^s + \phi_e^f \boldsymbol{v}_e^f)\}$
$\lambda_e^{(0)} = 0$, $\beta_e^{(0)} = \beta_0$, $\xi^{(0)} = \max(1/\beta_e^{(0)})$, $h^{(0)} = \infty$
$k = 0$
DO n increments
  WHILE $h^{(k)} > TOL$
    $\Delta\boldsymbol{u} = 0$
    DO j iterations
      solve $\boldsymbol{r}_{n+1}^{(j)} = G(\boldsymbol{u}_n^s, \boldsymbol{u}_n^f; \delta\boldsymbol{\chi}^s, \delta\boldsymbol{\chi}^f)$
      if $|\boldsymbol{r}_{n+1}^{(j)}| < TOL$ then endif
        else $\Delta\boldsymbol{u}_{n+1}^{(j+1)} = \{[\boldsymbol{\delta G}]^j\}^{-1}\boldsymbol{r}_{n+1}^{(j)}$
    END DO
    $h^{(k+1)} = \max_{e=1,N_e}\{h_e^{(k)}\}$
      $= \max_{e=1,N_e}\{\nabla\cdot(\phi_e^s \boldsymbol{v}_e^s + \phi_e^f \boldsymbol{v}_e^f)\}$
    IF $h^{(k+1)} > \xi^{(k)}$
      IF $h_e^{(k)} > \xi^{(k)}$
      $\beta_e^{(k+1)} = 10\beta_e^{(k)}$
      END IF
    ELSE
      $\lambda_e^{(k+1)} = \lambda_e^{(k)} + \beta_e^{(k)} h_e^{(k)}$
      $\xi^{(k+1)} = 0.2\xi^{(k)}$
      $k = k + 1$
    END IF
  END WHILE
  $\boldsymbol{u}_{n+1}^{(k+1)} = \boldsymbol{u}_n^{(k)} + \Delta\boldsymbol{u}_{n+1}^{(k)}$
  $n := n + 1$
END DO

3.3.5 FE Approximation and Consistent Linearization

The corresponding finite element approximation of the weak form (73) is obtained after subdividing the continuum into an appropriate FE mesh. An isoparametric conforming finite element approximation of the space of admissible variations is defined in the standard manner as

$$\delta \mathbf{u}^{\alpha} = \sum_{j=1}^{m} \phi_j \delta \mathbf{u}_j^{\alpha}, \qquad \delta \mathbf{u}_j^{\alpha} \in \mathbb{R}^3 \tag{96}$$

where ϕ_j are the isoparametric shape functions and m is the number of nodes which the approximate function is computed.

After substituting the independent variables by their approximated counterparts, the non-linear algebraic system is obtained. To achieve the solution of this system at $\Omega_0 + \Delta \boldsymbol{u}_n^{\alpha}$, an initial estimate for $\Delta \boldsymbol{u}_n^{\alpha}$, $\alpha = s, f$ can be assumed. This estimate is then iteratively improved using, for examples, a consistently linearized full-Newton method. The term consistent simply means that the expression of $G(\boldsymbol{u}^s, \boldsymbol{u}^f; \delta\boldsymbol{\chi}^s, \delta\boldsymbol{\chi}^f)$ is linearized after the approximation, that is, from $G(\bar{\boldsymbol{u}}^s, \bar{\boldsymbol{u}}^f; \delta\overline{\boldsymbol{\chi}}^s, \delta\overline{\boldsymbol{\chi}}^f)$ ensuring that quadratic convergence is maintained along the Newton iteration strategy. This linearization takes the form:

$$\begin{aligned} \overline{LG}_e^{k+1} &= \overline{G}_e^k + \boldsymbol{D}\overline{G}_e^k \cdot \left(\Delta \bar{\boldsymbol{u}}^{\alpha(k+1)} - \Delta \bar{\boldsymbol{u}}^{\alpha(k)}\right) \\ &= \overline{G}_e^k + \boldsymbol{D}\overline{G}_e^k \cdot \left(\Delta\Delta \bar{\boldsymbol{u}}^{\alpha(k)}\right) \end{aligned} \tag{97}$$

where $\overline{()}$ denotes the approximated counterparts.

In what follows the directional derivatives will be denoted as:

$$\begin{aligned} \boldsymbol{\delta}^s \overline{G}_e &= \boldsymbol{D}\overline{G}_e \cdot (\Delta\Delta \bar{\boldsymbol{u}}_n^s, 0) \\ \boldsymbol{\delta}^f \overline{G}_e &= \boldsymbol{D}\overline{G}_e \cdot (0, \Delta\Delta \bar{\boldsymbol{u}}_n^f) \end{aligned} \tag{98}$$

where the term $\boldsymbol{\delta}^s \overline{G}_e$ corresponds to the directional derivative of $\overline{G}_e$ in the direction of $\Delta\Delta \bar{\boldsymbol{u}}^s$ and $\boldsymbol{\delta}^f \overline{G}_e$ to the respective derivative in the direction of $\Delta\Delta \bar{\boldsymbol{u}}_n^f$.

The derivative of (77) at $\Delta \bar{\boldsymbol{u}}^{\alpha(k)}$ in the direction $\Delta\Delta \bar{\boldsymbol{u}}^{s(k)}$, that is, the Gâteaux derivative of the nonlinear functional $\overline{G}_s$ along the direction of $\Delta \bar{\boldsymbol{u}}^{\alpha}$ particularized for $\Delta\Delta \bar{\boldsymbol{u}}^{\alpha(k)}$ can be expressed as:

$$\begin{aligned} \boldsymbol{\delta}^s \overline{G}_s = &\int_{\Omega_0} \left[\operatorname{div}(\Delta\Delta \bar{\boldsymbol{u}}^s)\boldsymbol{\sigma}_e^s\right] : \nabla \delta\overline{\boldsymbol{\chi}}^s J \, \mathrm{d}v_0 \\ &+ \int_{\Omega_0} \operatorname{div}(\Delta\Delta \bar{\boldsymbol{u}}^s) : \left[p_e(\mathbf{1}\otimes\mathbf{1} - 2\mathbb{I}) + \widetilde{\mathbb{C}}\right] \\ &: (\nabla \delta\overline{\boldsymbol{\chi}}^s) J \, \mathrm{d}v_0 \end{aligned} \tag{99}$$

where all the terms are evaluated at $\boldsymbol{u}_{n+1}^{(k)}$ and the super and subscripts have been dropped for clearness. Note that p_e is the hydrostatic pressure due to the uncoupling of the strain energy function in a dilatational and deviatoric components and $\widetilde{\mathbb{C}}$ is the modified Green tensor defined in (18).

In (99) the first term represents the geometric, or initial stress stiffness matrix, and the second represents the material stiffness. These terms arise in a traditional displacement-based nonlinear analysis.

The derivative of (78) at $\Delta \bar{\boldsymbol{u}}^{\alpha(k)}$ in the direction $\Delta\Delta \bar{\boldsymbol{u}}^{s(k)}$ is:

$$\begin{aligned} \boldsymbol{\delta}^s \overline{G}_{\mathrm{Drag}} = &\int_{\Omega_0} \delta\overline{\boldsymbol{\chi}}^s \cdot \boldsymbol{\pi} J \operatorname{div} \Delta\Delta \bar{\boldsymbol{u}}^s (\bar{\boldsymbol{v}}_s - \bar{\boldsymbol{v}}_f) J \, \mathrm{d}v_0 \\ &+ \int_{\Omega_0} \delta\overline{\boldsymbol{\chi}}^s \cdot \boldsymbol{K} \eta^s \Delta\Delta \bar{\boldsymbol{u}}^s J \, \mathrm{d}v_0 \\ &+ \int_{\Omega_0} \delta\overline{\boldsymbol{\chi}}^s \cdot \boldsymbol{K} (\bar{\boldsymbol{v}}_s - \bar{\boldsymbol{v}}_f) J \operatorname{div} \Delta\Delta \bar{\boldsymbol{u}}^s \, \mathrm{d}v_0 \\ &- \int_{\Omega_0} \delta\overline{\boldsymbol{\chi}}^f \cdot \boldsymbol{\pi} J \operatorname{div} \Delta\Delta \bar{\boldsymbol{u}}^s (\bar{\boldsymbol{v}}_s - \bar{\boldsymbol{v}}_f) J \, \mathrm{d}v_0 \\ &- \int_{\Omega_0} \delta\overline{\boldsymbol{\chi}}^f \cdot \boldsymbol{K} \eta^s \Delta\Delta \bar{\boldsymbol{u}}^s J \, \mathrm{d}v_0 \\ &- \int_{\Omega_0} \delta\overline{\boldsymbol{\chi}}^f \cdot \boldsymbol{K} (\bar{\boldsymbol{v}}_s - \bar{\boldsymbol{v}}_f) J \operatorname{div} \Delta\Delta \bar{\boldsymbol{u}}^s \, \mathrm{d}v_0 \end{aligned} \tag{100}$$

where $\boldsymbol{\pi}$ is the partial derivative of the scalar diffusive drag matrix with respect to the Jacobian, $\partial \boldsymbol{K}/\partial J$, that depends on the permeability function and η^s is a scalar that depends on the algorithm used to define the velocity of the solid (see Sect. 3.3.1). The directional derivative of J along $\Delta\Delta \bar{\boldsymbol{u}}^s$ is expressed as:

$$\boldsymbol{\delta}^s J = J \operatorname{div}(\Delta\Delta u^s) \tag{101}$$

On the other hand, the derivative of (78) at $\Delta \bar{\boldsymbol{u}}^{\alpha(k)}$ in the direction $\Delta\Delta \bar{\boldsymbol{u}}^{f(k)}$ is:

$$\begin{aligned} \boldsymbol{\delta}^f G_{\mathrm{Drag}} = &- \int_{\Omega_0} \delta\overline{\boldsymbol{\chi}}^s \cdot \boldsymbol{K} \eta^f \Delta\Delta \bar{\boldsymbol{u}}^f J \, \mathrm{d}v_0 \\ &+ \int_{\Omega_0} \delta\overline{\boldsymbol{\chi}}^f \cdot \boldsymbol{K} \eta^f \Delta\Delta \bar{\boldsymbol{u}}^f J \, \mathrm{d}v_0 \end{aligned} \tag{102}$$

where η^f depends on the algorithm used for the fluid velocity definition (see Sect. 3.3.1).

Finally, the derivative of (79) at $\Delta \bar{\boldsymbol{u}}^{\alpha(k)}$ in the direction $\Delta\Delta \bar{\boldsymbol{u}}^{s(k)}$ is:

$$\begin{aligned} \boldsymbol{\delta}^s G_{\mathrm{Aug}} = &\sum_{\alpha=s,f} \left\{ \int_{\Omega_0} \boldsymbol{\delta}^s \left[\operatorname{div}(\phi^{\alpha} \delta\overline{\boldsymbol{\chi}}^{\alpha})\right] \right. \\ &\left[\lambda + \beta \operatorname{div}(\phi^s \bar{\boldsymbol{v}}^s + \phi^f \bar{\boldsymbol{v}}^f)\right] J \, \mathrm{d}v_0 \\ &+ \int_{\Omega_0} \operatorname{div}(\phi^{\alpha} \delta\overline{\boldsymbol{\chi}}^{\alpha}) \boldsymbol{\delta}^s \\ &\left. \left[\lambda + \beta \operatorname{div}(\phi^s \bar{\boldsymbol{v}}^s + \phi^f \bar{\boldsymbol{v}}^f)\right] J \, \mathrm{d}v_0 \right. \end{aligned}$$

$$+\int_{\Omega_0}\operatorname{div}(\phi^\alpha\delta\overline{\boldsymbol{\chi}}^\alpha)\Big[\lambda+\beta\operatorname{div}(\phi^s\bar{\boldsymbol{v}}^s+\phi^f\bar{\boldsymbol{v}}^f)\Big]\boldsymbol{\delta}^s[J]\,\mathrm{d}v_0\Big\} \tag{103}$$

Next, each derivative is expanded in the following way,

$$\begin{aligned}&\boldsymbol{\delta}^s\big[\operatorname{div}(\phi^s\overline{\boldsymbol{\chi}}^s)\big]\\&=\frac{\phi_0^s}{J^2}\big\{2\operatorname{div}\Delta\Delta\bar{\boldsymbol{u}}^s\nabla J-\boldsymbol{\delta}^s[\nabla J]\big\}\cdot\Delta\Delta\bar{\boldsymbol{u}}^s\\&\quad-\frac{\phi_0^s}{J}\operatorname{div}\Delta\Delta\bar{\boldsymbol{u}}^s\operatorname{div}\Delta\Delta\bar{\boldsymbol{u}}^s\\&\quad+\phi^s\boldsymbol{\delta}^s[\boldsymbol{F}^{-1}]:\overline{\nabla}\Delta\Delta\bar{\boldsymbol{u}}^s\end{aligned} \tag{104}$$

where the term ∇J, $\boldsymbol{\delta}^s[\nabla J]$ and $\boldsymbol{\delta}^s[\boldsymbol{F}^{-1}]$ are defined below; and the operators ∇ and $\overline{\nabla}$ are the gradient operators in the current configuration and reference configuration, respectively.

The gradient of the Jacobian of the solid phase can be expressed as:

$$(\nabla J)_l=\epsilon_{IJK}\left(\frac{\partial F_{I1}}{\partial x_l}F_{J2}F_{K3}+F_{I1}\frac{\partial F_{J2}}{\partial x_l}F_{K3}+F_{I1}F_{J2}\frac{\partial F_{K3}}{\partial x_l}\right) \tag{105}$$

with $\boldsymbol{F}$ the deformation gradient.

Thus, the directional derivative of the gradient of the Jacobian (105) is,

$$\begin{aligned}\boldsymbol{\delta}^s(\nabla J)&=\boldsymbol{\delta}^s(\overline{\nabla}J\cdot\boldsymbol{F}^{-T})\\&=\overline{\nabla}(\boldsymbol{\delta}^sJ)\boldsymbol{F}^{-T}+\overline{\nabla}J\boldsymbol{\delta}^s(\boldsymbol{F}^{-T})\\&=\overline{\nabla}(J\operatorname{div}\Delta\boldsymbol{u}^s)\boldsymbol{F}^{-T}-\overline{\nabla}J\boldsymbol{F}^{-T}\overline{\nabla}\Delta\boldsymbol{u}^s\boldsymbol{F}^{-T}\\&=\nabla(J\operatorname{div}\Delta\boldsymbol{u}^s)-\nabla J\overline{\nabla}\Delta\boldsymbol{u}^s\boldsymbol{F}^{-T}\\&=\nabla(J\operatorname{div}\Delta\boldsymbol{u}^s)-\nabla J\cdot\nabla(\Delta\boldsymbol{u}^s)\end{aligned} \tag{106}$$

Finally, the directional derivative of the inverse of the deformation gradient can be written as:

$$\boldsymbol{\delta}^s(\boldsymbol{F}^{-1})=-\boldsymbol{F}^{-1}(\boldsymbol{\delta}^s\boldsymbol{F})\boldsymbol{F}^{-1} \tag{107}$$

where the directional derivative of the deformation gradient can be defined as $\boldsymbol{\delta}^s\boldsymbol{F}=\overline{\nabla}\Delta\boldsymbol{u}^s$.

In the same way,

$$\begin{aligned}&\boldsymbol{\delta}^s\big[\operatorname{div}(\phi^s\bar{\boldsymbol{v}}^s+\phi^f\bar{\boldsymbol{v}}^f)\big]\\&=\frac{\phi_0^s}{J^2}\big\{2\operatorname{div}\Delta\Delta\bar{\boldsymbol{u}}^s-\boldsymbol{\delta}^s[\nabla J]\big\}(\bar{\boldsymbol{v}}^s-\bar{\boldsymbol{v}}^f)\\&\quad-\frac{\phi_0^s}{J^2}\nabla J\eta^s\Delta\Delta\bar{\boldsymbol{u}}^s\\&\quad+\phi^s\big[\boldsymbol{\delta}^s[\boldsymbol{F}^{-1}]:\overline{\nabla}\bar{\boldsymbol{v}}^s+\boldsymbol{F}^{-1}:\eta^s\overline{\nabla}\Delta\Delta\bar{\boldsymbol{u}}^s\big]\\&\quad-\frac{\phi_0^s}{J}\operatorname{div}\Delta\Delta\bar{\boldsymbol{u}}^s(\operatorname{div}\bar{\boldsymbol{v}}^s-\operatorname{div}\bar{\boldsymbol{v}}^f)\end{aligned} \tag{108}$$

where η^s arise from the time evolution algorithm, and finally

$$\begin{aligned}&\boldsymbol{\delta}^s\big[\operatorname{div}(\phi^f\overline{\boldsymbol{\chi}}^f)\big]\\&=-\frac{\phi_0^s}{J^2}\big\{2\operatorname{div}\Delta\Delta\bar{\boldsymbol{u}}^s\nabla J-\boldsymbol{\delta}^s[\nabla J]\big\}\cdot\Delta\Delta\bar{\boldsymbol{u}}^f\\&\quad+\frac{\phi_0^s}{J}\operatorname{div}\Delta\Delta\bar{\boldsymbol{u}}^s\operatorname{div}\Delta\Delta\bar{\boldsymbol{u}}^f+\phi^f\boldsymbol{\delta}^s[\boldsymbol{F}^{-1}]:\overline{\nabla}\Delta\Delta\bar{\boldsymbol{u}}^f\end{aligned} \tag{109}$$

Operating in the same way, the derivative of (79) at $\Delta\bar{\boldsymbol{u}}^{\alpha(k)}$ in the direction $\Delta\Delta\bar{\boldsymbol{u}}^{f(k)}$ is

$$\boldsymbol{\delta}^fG_\beta=\sum_{\alpha=s,f}\left\{\beta\int_{\Omega_0}\operatorname{div}(\phi^\alpha\Delta\Delta\bar{\boldsymbol{u}}^\alpha)\{\operatorname{div}\phi^f\eta^f\Delta\Delta\bar{\boldsymbol{u}}^f+\phi^f\eta^f\overline{\nabla}\Delta\Delta\bar{\boldsymbol{u}}^f\}J\,\mathrm{d}v_0\right\} \tag{110}$$

The above linearization process of the weak form of biphasic materials can be simplified for materials with the solid being the only one that significantly contributes to its overall behavior. Thus, as mentioned before, for the case of ligaments, this formulation can be simplified by removing the terms with superindex f.

4 Simulation of Articulate Joints

The three types of joints that exist in the human body are fibrous, cartilaginous, and synovial. Synarthroses, or fibrous joints are those in which the bone surfaces have very little movement relative to each other (skull). Amphiarthroses, or cartilaginous joints, are those in which the bone surfaces may have some relative movement (vertebral bodies of the spine). Only synovial, or diarthrodial joints will be discussed in this paper. They allow a large degree of relative movement between the opposing bones. Some examples of this type of joint are the shoulder, elbow, hip, knee, temporomandibular and ankle. We will only focus here in two important diarthrodial joints such as the knee and the temporomandibular joint.

4.1 Knee Joint

4.1.1 Anatomical Description of the Knee Joint

Although the knee may look like a simple joint, it is one of the most complex. Moreover, the knee is more likely to be injured than any other joint in the body. The knee is essentially made up of four bones: femur, tibia, patella and fibula; four ligaments: anterior and posterior ligaments (ACL, PCL) and lateral and medial collateral ligaments (LCL and MCL), patellar tendon (PT), articular cartilage and menisci (Fig. 7). The human knee joint compliance and stability required for

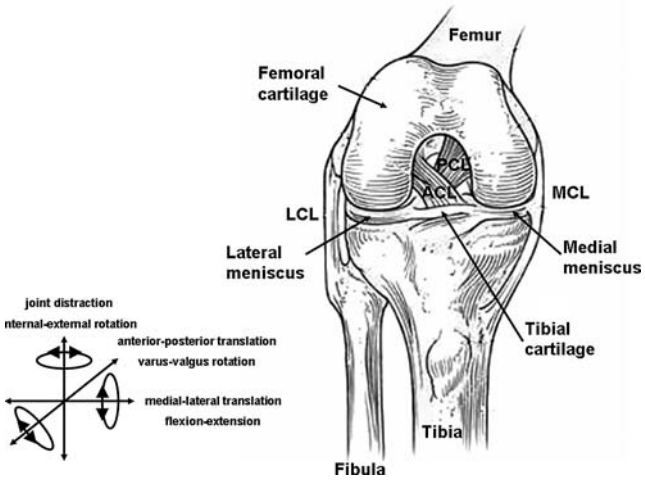

Fig. 7 Anterior view of the knee joint with the description of its main components

optimal daily functions are provided by several components like menisci, cartilage, ligaments and muscle forces that allow complex mechanical responses to different types of physiological loads.

An important multifunctional component of the knee are the menisci. They are a complex biomechanical system in themselves, with a fundamental role in load transmission, shock absorption, proprioception, improvement of stability and lubrication [196]. In order to perform these functions efficiently, their behavior is completely dynamic. They effectively distribute contact forces over the articular surfaces by increasing the contact surface of the joint. Load distribution over an incongruent joint surface is redistributed by the menisci by maintaining maximal congruency. The functionality of the menisci and their role in load transmission across the knee have been discussed by many authors [52, 122]. This functionality is strongly affected by various lesions. For example, Scheller et al. [172], Jackson [94] found frequent degenerative changes after meniscectomy.

Because of the relative incongruence of the articular surfaces, ligaments play an important role in providing passive stability to the joint. For the development of adequate diagnostic and surgical procedures, it is essential to understand the role of individual ligament as motion restraints [22]. The primary role of the ligaments that surround the knee is to provide stability to the joint throughout its range of motion. Each ligament plays a role in providing stability in more than one degree of freedom as well as restraining knee motion in response to externally applied loads. Overall joint stability depends on the contributions of the individual ligaments as well as interaction between them.

The anterior cruciate ligament (ACL) is known to be a restraint against anterior tibial loads by limiting anterior tibial translations. The posterior cruciate ligament (PCL) is a major stabilizer of the knee joint. The PCL is known to be a restraint against posterior tibial loads by limiting posterior tibial translations. But, the role of the PCL under more complex rotatory motions is not clear [56]. The function of the medial collateral ligament (MCL) as the primary valgus restrain has firmly established [91]. Depending upon the investigation read, the MCL has been shown to resist external rotation, internal rotation, both rotations, and neither rotation. However, the majority of the experiments point to the MCL as a restraint to external rotation only [9]. Of the two collateral ligaments, the lateral collateral ligament (LCL) has received considerably less attention. Owing to its position contralateral to the MCL, the LCL would be expected to resist varus and internal rotation, as has been shown by many authors [9, 22, 69]. The activity of the LCL in response to tibial axial rotation is not well established.

4.1.2 A Brief Review of Available Numerical Models of the Knee Joint

Knee models can help to understand the biomechanics of the joint and can also be used to estimate the consequences of injuries and surgical treatments. In this review we distinguish two types of knee models: analytical and FE models. The analytical models are used to describe the distribution of the forces in muscles and ligaments, contact forces and the kinematics of the knee during different types of joint loading conditions. On the contrary, FE models can predict nonuniform 3D stresses and strains and study the combined behavior of the main components in load transmission and stability.

Early attempts to model the knee joint articulation were primarily centered on rigid body models with prescribed bending moments and simple analytical approximations (which provided a simplification of the knee using closed-form expressions). In particular, the use of the Hertzian theory has been extensively used to model articulation contact mechanics [47, 48]. However, the simplifications in geometry and boundary conditions limit its usefulness for patella focused studies. Moreover, the majority of these studies were 2D. Hefzy and Grood [74] developed an analytical model to include geometric nonlinearities such as ligament wrapping. Discrete element joint models have been developed to simulate the response of joints to dynamically applied loads [1, 48, 51]. The inertial effects of bones were included in these joint models and in all cases, the ligaments were represented by simple elastic springs while bones were modelled as rigid bodies. The approach used by Moeinzadeh and Engin [128] in the development of a two-dimensional, sagittal plane knee joint model considered nonlinear elastic spring ligaments to connect the rigid bones. The model was used to predict ligament and joint contact forces with the application of dynamic loads to the tibia. These models, while useful, especially for dynamic analysis, have obvious limitations such as point contact assumptions and inextensible

ligaments as pointed out by Beynnon et al. [20, 22, 27]. For a more detailed review of the analytical models available in the literature, see [73].

The first FE models were developed for the patello-femoral articulation. Matthews et al. [127] and Huberti et al. [89] studied the contact area and pressures in the patellar cartilage. Heegard et al. [72] and Hefzy and Yang [75] developed a tridimensional model of the patello-femoral articulation to simulate de knee flexion in order to determine patello-femoral motions and contact mechanics. In all cases, ligaments were modelled using one-dimensional representations. With respect to the tibio-femoral joint, some studies have been developed in the literature. Bendjaballah et al. [17, 18] and Jalani et al. [96] constructed respective nonlinear finite element models of the entire human knee to investigate the biomechanics of the passive tibiofemoral joint in full extension under anterior-posterior drawer forces and internal-external torques. Perie and Hobatho [163] and Li et al. [112, 113] considered joint contact stresses and contact areas on the human knee menisci. In all these models, ligaments were modelled as non-linear springs. In addition, the combined behavior of ligaments and menisci was not considered in any of them.

Other researchers developed 3D finite element models of individual human ligaments such as the ACL [61, 62, 81, 115, 160, 183] or the MCL [63]. Gardiner et al. [62] developed a finite element model of the MCL to study its three-dimensional stress-strain behavior under valgus loading. Gabriel et al. [61] determined the distribution of an in situ force between the two bundles of the ACL when the knee is subject to anterior tibial and rotatory loads. Hirokawa et al. [81] developed a three-dimensional model of the ACL that was used to study the deformation and stress distributions in this ligament during knee flexion. Limbert et al. [115] proposed a 3D finite element model of the human ACL, that model was used to simulate clinical procedures such as the Lachman and drawer tests. Moglo and Shirazi-Adl [129] used a 3D finite element model of the knee in order to study the cruciate coupling and screw-home mechanics in passive knee joint during extension-flexion movement. In all these studies, the interactions between ligaments and between ligaments and other components of the knee were not taken into account.

The model developed by Peña et al. [145] is one of the most complete model of the healthy human knee joint available in the literature. It includes all the relevant ligaments (ACL, PCL, LCL, MCL and PT), menisci and articular cartilages. Femur and tibia were considered to be rigid, articular cartilage and menisci linearly elastic, isotropic and homogeneous while ligaments were modelled as 3D hyperelastic transversely isotropic. Initial strains in all the ligaments were considered. This model [145] has been used to analyze the combined role of menisci and ligaments in load transmission and stability.

Three-dimensional Finite Element models can also be used to estimate the consequences of injuries and surgical treatments. Most models of injured and reconstructed knee joint have been directed towards ligament injuries. For example, Au et al. [11] developed a three dimensional finite element model in order to study the stress in surgically altered femur and tibia. In that model, only bones were simulated and no knee soft tissue was considered. Raminaraka et al. [167] performed a 3D computational study of the influence of graft mechanical properties after PCL reconstruction. They replaced the mechanical properties of the ligament with the mechanical properties of the graft, but they did not consider the reconstruction technique. They found higher contact pressures in the reconstructed joint than in the intact knee. Suggs et al. [187] developed a computational model of the human knee joint to study the ACL reconstruction. They used nonlinear springs to model ligaments and graft. That model was used to simulate ACL reconstruction using three different grafts. Since they modelled the graft as a spring, the graft stress distribution was not analyzed. Peña et al. [150] developed a 3D finite element model of the human knee including all the main ligaments and graft in order to study the effect of graft stiffness and graft tensioning on the knee joint biomechanics. They considered a transversely isotropic hyperelastic behavior of the ligaments that were initially prestressed. Another important surgery studied by FE models is meniscectomy. Wilson et al. [209] and Bendjaballah et al. [17] considered the effect of total medial meniscectomies on the human knee joint using the finite element method. Peña et al. [146, 147] studied the effect of total and partial medial and lateral meniscectomies.

4.1.3 Some Examples of Application

Description of the model In the following the model developed by Peña et al. [145] is summarized. The geometrical data of the model developed [145] were obtained by NMR (Nuclear Magnetic Resonance) for soft tissues and CT (Computerized Tomography) for bones, with images taken from a normal adult volunteer. The CT and NMR image block consisted of parallel digital images separated at intervals of 1.5 mm in the sagittal, coronal and axial planes with the knee at 0° flexion.

The contours of the femur, tibia, articular cartilage, menisci and ligaments (patellar tendon, anterior cruciate, posterior cruciate, medial collateral and lateral collateral) were manually identified in each image with the help of M.D.s from the Traumatology Department of the University of Zaragoza (Fig. 8). The manual segmentation had an accuracy of 0.3 mm. These lines were transferred into the commercial code I-DEAS v.9 where the main surfaces and solid version of the model were reconstructed (Fig. 8c).

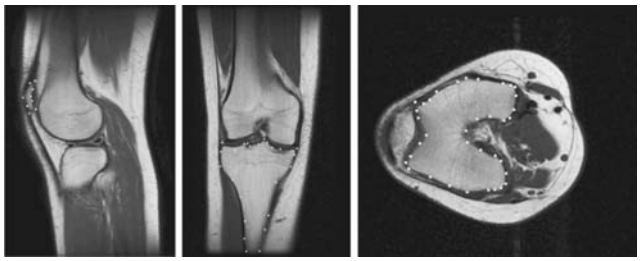

(a) Sagittal (b) Coronal (c) Axial

Fig. 8 NMR images [145]

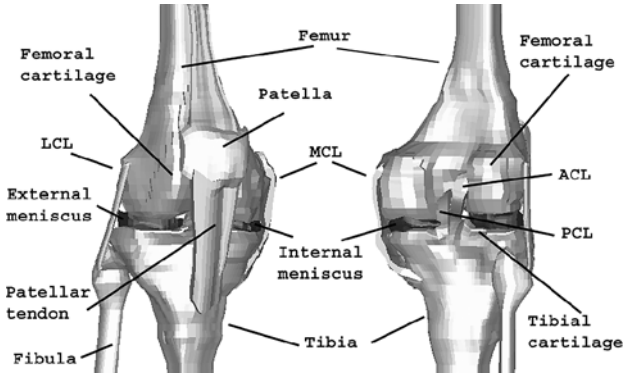

Fig. 9 Finite element model of the knee joint [145]

Bones were assumed to be rigid in this model, and hexahedral block-structured meshes of the ligaments, menisci and articular cartilages were constructed. A total of 4783 four-node surface elements were used to mesh the bony surfaces and 5195 eight-node brick elements for the meshes of cartilages, menisci and ligaments (Fig. 9). In all cases, trilinear hexahedral elements with a full geometrically nonlinear formulation were used, see Sect. 3.

Although menisci and cartilage are hydrated tissues, in that case, and considering that the loading time of interest corresponded to that of a single leg stance, and the viscoelastic time constant of cartilage approaches 1500 seconds [10], articular cartilage was considered to behave as a single-phase linear elastic and isotropic material with an elastic modulus of $E = 5$ MPa and a Poisson ratio of $\nu = 0.46$ [113]. This is accurate enough to predict short-term cartilage response as demonstrated by Donzelli et al. [45], who proved that there are no significant changes in the cartilage contact response shortly after loading. For the same reason, menisci were also assumed to be a single-phase linear elastic and isotropic material with the following average properties: elastic modulus of $E = 59$ MPa and Poisson ratio of $\nu = 0.49$ [110].

On modelling ligaments, two important assumptions were made. First, no difference in the material behavior between the ligament body and its insertion were considered. Second, material characteristics depending on time, such as viscoelasticity, creep and relaxation were neglected [81] due again to the high ratio between the viscoelastic time constant of the material and the loading time of interest in this study. A transversely isotropic hyperelastic model was used including the effect of one family of fibers, usually applied to ligaments [201].

The volumetric part Ψ_{vol} (8) was considered, in a standard manner for quasi-incompressible materials, as a penalty function of the Jacobian [84]. The isochoric part $\bar{\Psi}$ of the strain-energy function (8) was divided into an isotropic part that corresponds to a Neo-Hookean model and other depending on the collagen fibers, see Sect. 2.3.2. We had in turn

$$\Psi = \frac{1}{2D}\ln(J)^2 + C_1\left(\bar{I}_1 - 3\right) + F_2(\lambda) \tag{111}$$

where C_1 is the Neo-Hookean constant and D the inverse of the bulk modulus $k = 1/D$ which was chosen for all the ligaments as $k/C_1 = 1000$ [202]. For $F_2(\lambda)$, the free-energy function defined in (26) earlier proposed by Weiss et al. [206] was used with the average constants obtained by Gardiner and Weiss [62] for the MCL in their experimental data. The LCL constants were assumed to be identical to those of the MCL. The uniaxial stress-strain curves obtained by Butler et al. [24] for ACL, PCL and PT (patellar tendon) were fit with those obtained by Weiss's getting the associated constants that have been included in Table 2.

In order to consider initial strains in ligaments, the methodology presented in previous section was employed. Initial strains in that model were defined from data available in literature [22, 112, 183] and have been included in Table 2 with the following terminology: a: anterior part of ligament; p: posterior part of ligament; m: medial part of ligament. Figure 10 shows the strain distribution for the ligaments after equilibrium but before the application of external loads. Obviously, the initial strains obtained after that equilibrium step are not exactly the prescribed ones. The differences found were all of them under 10% except in the PCL where a small initial strain appeared after equilibrium that Blankevoort and Huiskes [22] did not consider.

Boundary conditions were defined as follows. Each of the horns of the menisci and the external periphery of the medial meniscus, which is joined to the medial collateral ligament, were attached to the tibial plateau, simulating the horn-menisci attachment. Ligaments were attached to bone by establishing the final row of elements at their proximal and distal ends to be composed of the same material than the nearby bone [62].

Frictionless nonlinear contact was assumed for all the articulations [136] and fifteen potential contact zones were identified: two at the medial zone and two at the lateral (femoral cartilage-meniscus and meniscus-tibial cartilage), four between ligaments (MCL, LCL, ACL and PCL) and

Table 2 Material parameters for the ligament stress-free state

	C_1 (MPa)	C_2 (MPa)	C_3 (MPa)	C_4	C_5 (MPa)	λ^*	D (MPa^{-1})	Initial strains (%)
aMCL	1.44	0.0	0.57	48.0	467.1	1.063	0.00126	0.04
mMCL	1.44	0.0	0.57	48.0	467.1	1.063	0.00126	0.04
pMCL	1.44	0.0	0.57	48.0	467.1	1.063	0.00126	0.03
aLCL	1.44	0.0	0.57	48.0	467.1	1.063	0.00126	0.0
pLCL	1.44	0.0	0.57	48.0	467.1	1.063	0.00126	0.08
aACL	1.95	0.0	0.0139	116.22	535.039	1.046	0.00683	0.03
pACL	1.95	0.0	0.0139	116.22	535.039	1.046	0.00683	0.03
PCL	3.25	0.0	0.1196	87.178	431.063	1.035	0.0041	0.0
PT	2.75	0.0	0.065	115.89	777.56	1.042	0.00484	0.01

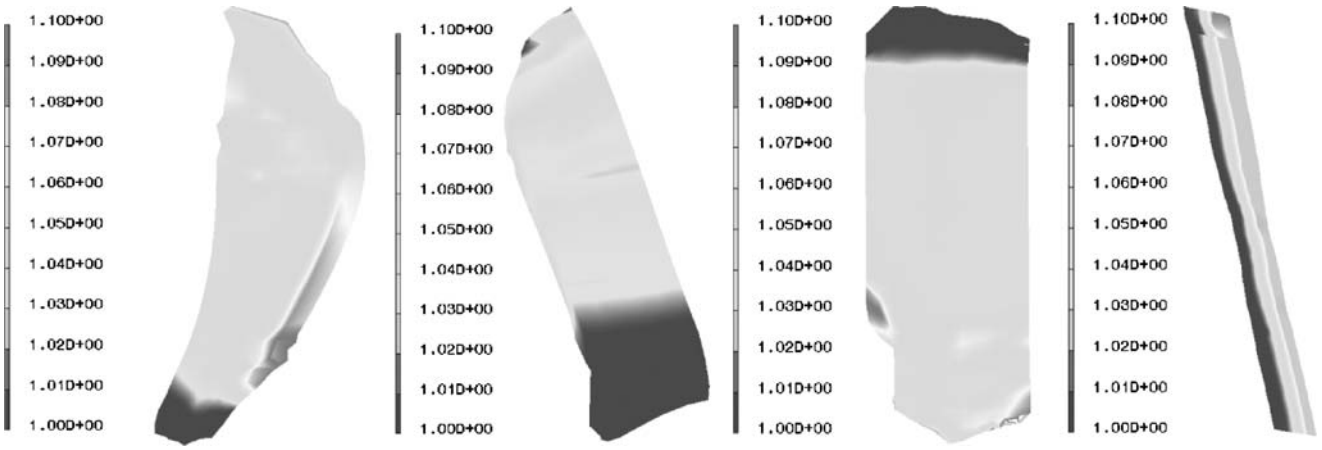

(a) ACL (b) PCL (c) MCL (d) LCL

Fig. 10 Initial stretch of the fibers after the equilibrium step and before loading in the different ligaments [145]

femur, four between ligaments and tibia and one between cruciate ligaments and between the femoral cartilage and the retropatellar articular cartilage. Contact conditions in the model were completely general including finite sliding. The motion of each bone was controlled by the six degrees of freedom of its reference node. In all the analyses, tibia and fibula remained fixed. The position at full extension served as the reference initial configuration.

Healthy joint The first example analyzes the combined role of menisci and ligaments in load transmission and stability. A compression load of 1150 N was applied for all the cases that corresponds to the maximal force in the gait cycle obtained by Sathasivam and Walker [170] at full extension. A load of 134 N in the anterior direction and a valgus torque of 10 Nm were also applied.

Under anterior tibial load of 134 N and a compression load of 1150 N, the anterior cruciate ligament supported about 75% of the total anterior load and the medial collateral ligament the rest 25% as secondary stabilizer. Figures 11 and 12 shows the results obtained in different ligaments under this anterior load. A significant tensile stress appeared in the posterior part of the ACL. The

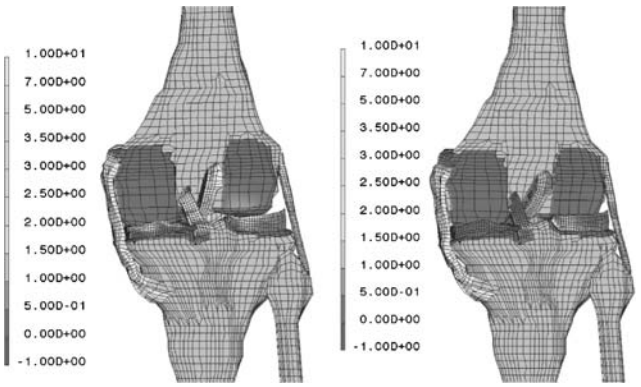

(a) Anterior load (b) Valgus torque

Fig. 11 Maximal principal stresses in the soft tissues of the knee at different loads

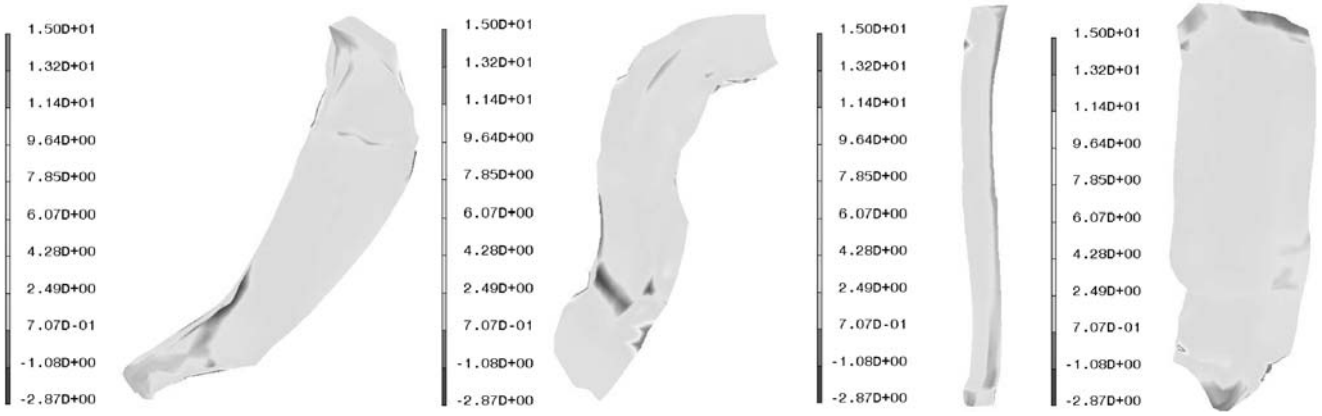

(a) ACL (b) PCL (c) LCL (d) MCL

Fig. 12 Maximal principal stresses in the ligaments in response to a compressive load of 1150 N and an anterior tibial load of 134 N (MPa) [145]

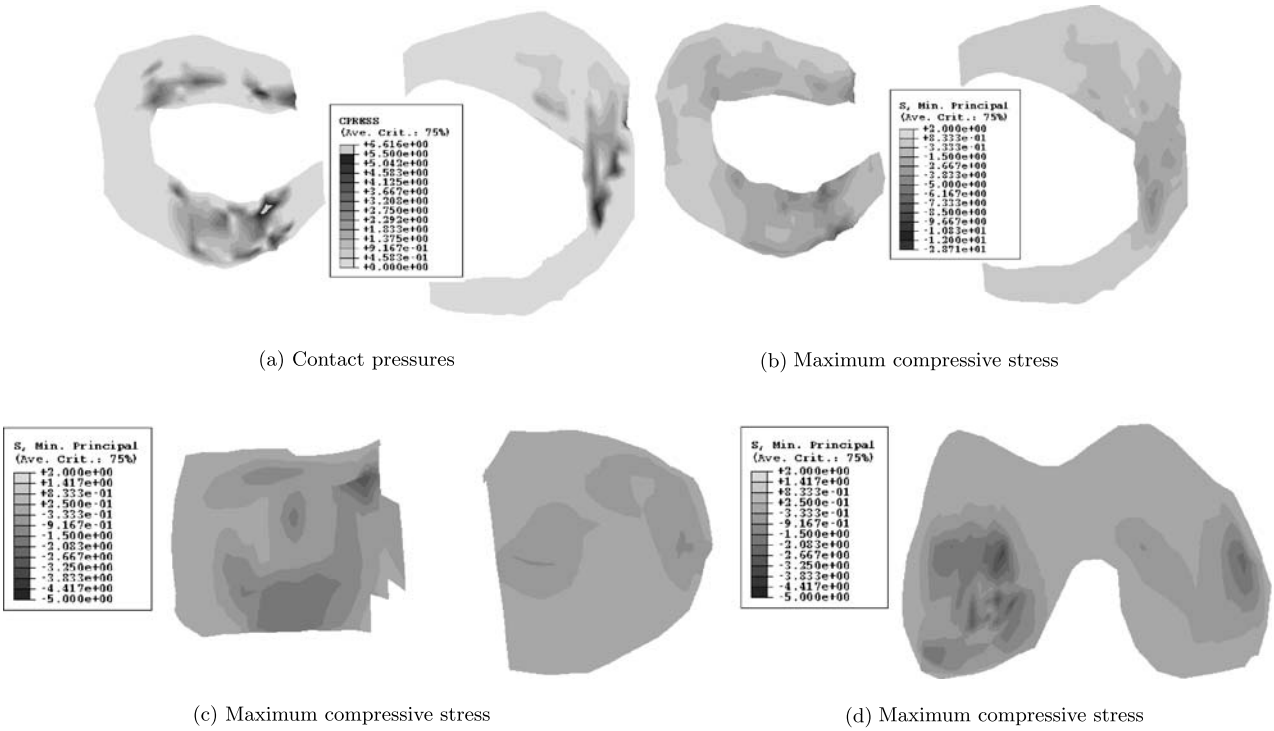

(a) Contact pressures (b) Maximum compressive stress

(c) Maximum compressive stress (d) Maximum compressive stress

Fig. 13 Contact pressures and minimal principal stresses in menisci and articular cartilages under valgus rotation (MPa) [145]

obtained results also showed that the PCL was mainly in compression; only the anterior proximal part. The LCL was tensioned due to the initial strains since during this movement it is mainly relaxed. The anterior load produced in the MCL a stress distribution similar to a shear problem, with tension in the anterior-distal and the posterior-proximal parts of the MCL. Menisci transferred about 62% of the total axial load (40% the medial meniscus, mainly concentrated on the lateral side). Contact stresses were slightly higher in the lateral meniscus [145]. They basically corresponded to the contact zones between the femoral condyles and the menisci and were very similar to those obtained experimentally by Walker and Erkman [199].

The application of a 10 N m valgus torque induced a valgus rotation, as observed by other authors [63]. The MCL provides primary restraint to valgus rotation so, the highest maximal principal stress took place in this ligament. The application of a 10 N m valgus torque decreased the transferred load by the medial meniscus, that became about 43% of the total axial load (Fig. 13). In this case, the high-

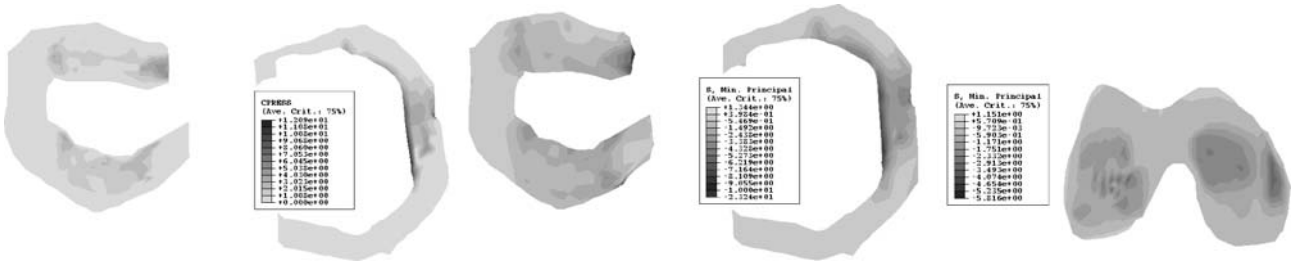

(a) Contact pressures (b) Maximum compression stress (c) Maximum compression stress

Fig. 14 Contact pressures and minimal principal stresses in the partial longitudinal medial meniscectomized joint [146]

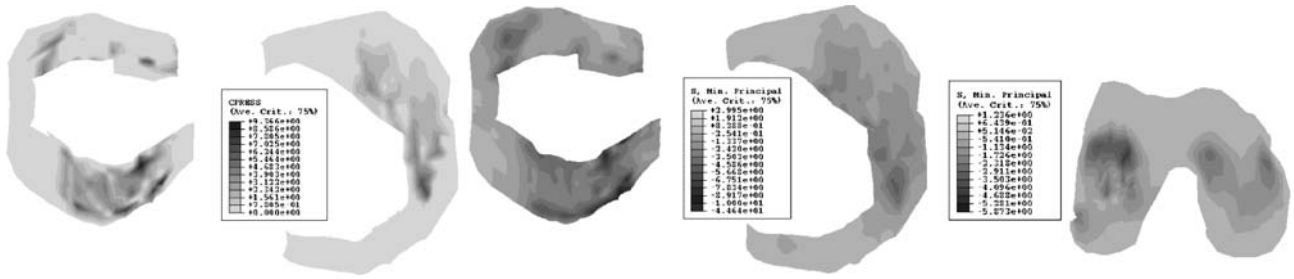

(a) Contact Pressure (b) Maximum compression stress (c) Maximum compression stress

Fig. 15 Contact pressures and minimal principal stresses in the partial longitudinal lateral meniscectomized joint [147]

est contact pressure and minimal principal stress (maximal compression) took place in the lateral meniscus.

The obtained results resulted close to experimental ones, demonstrating that subject-specific FE models can predict the complex, nonuniform stress and strain fields that occur in biological soft tissues and the kinematics of the human knee joint.

Pathological joint Finite element simulations help to understand the stress distribution in the human knee joint after joint injuries and pathological degeneration of articular joints [146]. For example, Peña et al. [146, 147] studied the effect of total and partial medial and lateral meniscectomies. They developed four finite element models of the meniscectomies removing elements of the model [146, 147].

In the first study developed by Peña et al. [146] for partial longitudinal medial meniscectomy, compression stresses and contact pressures in the remaining medial meniscus increases up to 107% and 143% respectively. For the articular cartilage (Fig. 14), there was a smoothing of the distribution of the compression stresses due to the translation of the contact area towards the posterior zone of the medial condyle with a maximal compression increase of 50 and 104% in the medial and lateral condyles, respectively [146]. In partial longitudinal lateral meniscectomy, the compression stresses and contact pressures grew up to 384% and 517% in contact pressure and compression stress, respectively (Fig. 15).

In another paper, a similar study was presented by Peña et al. [147] for a totally medially and laterally meniscectomized joint. The finite element model was obtained from the healthy joint (Fig. 9) by eliminating the medial or lateral meniscus. The same external load was considered. In the totally medially meniscectomized joint, a notable increase was observed in all the values. For example, the maximal shear stress increase for the totally medial and lateral meniscectomized joint were of 177% and 375%. The catastrophic effect of total lateral meniscectomies could be appreciated in these analyses. Increments of the maximal compression and the maximal shear stress on the articular cartilage reached values of 456% and 687% in the lateral condyle. A summary of the results is presented in Fig. 16. The values obtained in the FE simulation could help to understand why the clinical results after total or lateral meniscectomies are much poorer than those after medial ones [147].

Joint reconstruction Three-dimensional Finite Element models can also be used to estimate the consequences of surgical treatments in human knee joint. Most models of reconstructed knee joints have been directed towards ligament injuries, in particular, the anterior cruciate is the most frequent to be totally disrupted. There are many mechanical factors that influence the success or failure of ACL reconstruction. These include angle and position of the tunnels,

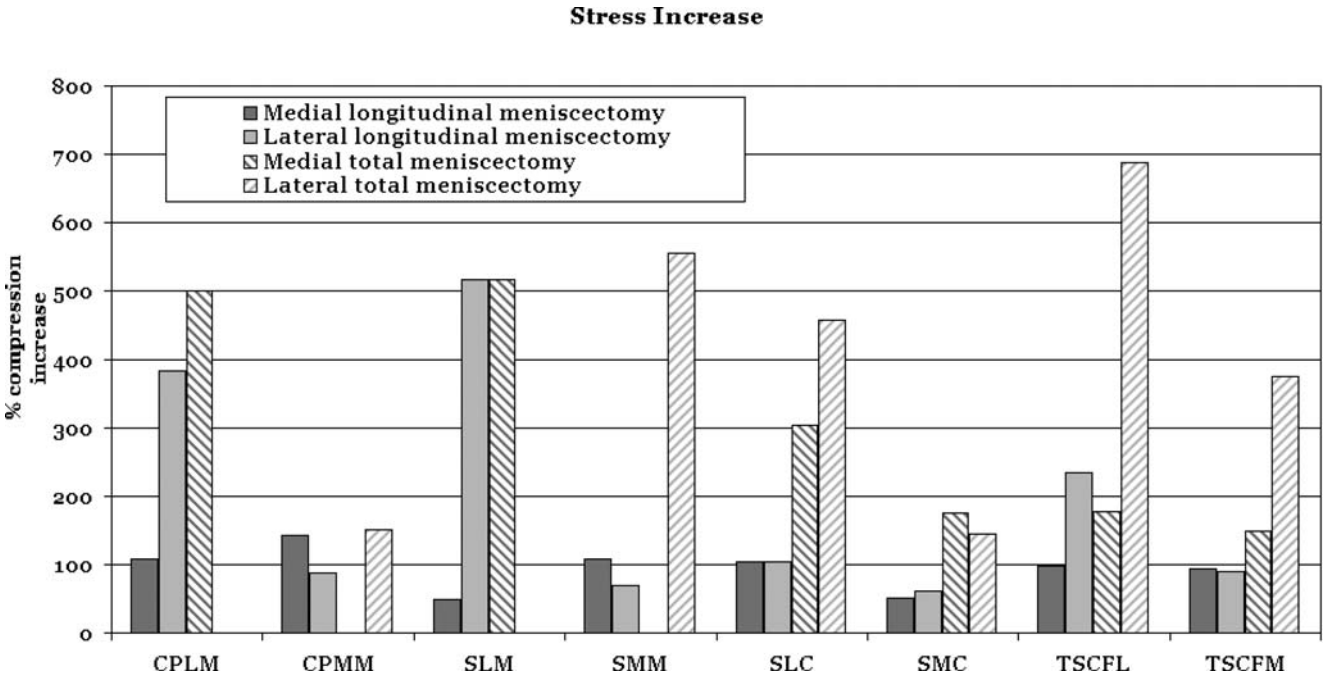

Fig. 16 Summary of the stress increase results for the lateral and medial meniscectomies (MPa). *CPMM*: Contact pressure in medial meniscus, *CPLM*: Contact pressure in lateral meniscus, *SMM*: Compression stress in medial meniscus, *SLC*: Compression stress in lateral meniscus, *SMC*: Compression stress in medial articular condyle cartilage, *SLC*: Compression stress in lateral articular condyle cartilage, *SMT*: Compression stress in medial articular tibial cartilage and *SLT*: Compression stress in lateral articular tibial cartilage

state of the articular and meniscal cartilages, graft material, surgical technique, and graft tension [58, 70, 111, 150].

One of the most complete model of the ACL reconstruction available in the literature is the model developed by Peña et al. [150]. The technique analyzed in that work was developed by Yoshiya et al. [214]. The 3D finite element models of the graft and bone plugs after positioned in the tibial and femoral tunnels and bone plugs were attached to the tibial and femoral surfaces allowing relative sliding by an appropriate contact algorithm without friction in the case of ligaments and without relative sliding in the case of bone plugs. Grafts were modelled as ligaments while bone plugs were considered to behave as linear elastic and isotropic with an elastic modulus of $E = 14220$ MPa and a Poisson ratio of $\nu = 0.3$ [95]. For details see [150]. Comparisons between published data [175] and the predicted kinematics in that paper under similar conditions demonstrated its good performance and accuracy.

The results corresponding to initial graft tensions of 0, 20, 40 or 60 N with the knee at 0°, 30° and 60° of flexion were obtained under 134 N of anterior load [150]. The joint did not fully recover, in any case, the kinematics of the healthy situation, although the anterior tibial translation was significantly less than that of the injured joint (Fig. 18). A pretension of 60 N produced much higher stresses in the graft than with an initial graft tension of 20 N or without it (Fig. 17). Three different grafts with stiffnesses corresponding to bone-patellar tendon-bone graft, gracilis graft and quadrupled semitendinosus graft were compared. Under the same load of 134 N, there were not relevant differences between the results obtained with patellar tendon and gracilis tendon grafts while the anterior tibial displacements resulted higher with a semitendinosus ligament [150].

That model was also used to investigate the effect of the angle in the coronal plane of femoral and tibial tunnels [144]. This angle was varied to 60°, 70°, and 80° for femoral and tibial tunnel, (Fig. 19). Graft tension and the resulting kinematics for the different angles under an anterior load of 134 N was compared to that of the intact knee. The angle of the femoral tunnel affects the graft tension while the tibial tunnel affects laxity, meniscal stresses and strains (Fig. 20).

Another clinical application of the FE model developed by Peña et al. [148] was the evolution along time of the initial prestress in bone-patellar tendon-bone grafts (see Sect. 2.3.2). Before graft fixation, an initial pretension is applied. The value of this initial tension applied to the replacing graft significantly alters the joint kinematics. This prestress helps to provide joint stability, but a very high pretension produces an important additional stress in the graft during the knee movement. Viscoelasticity decreases the tension imposed during surgery until its stabilization. The decrease of this initial stress can compromise the joint stability, affecting the postoperative results. Biomechanical testing protocols include preconditioning (cyclic or static stretching of the graft prior to implantation) to ensure

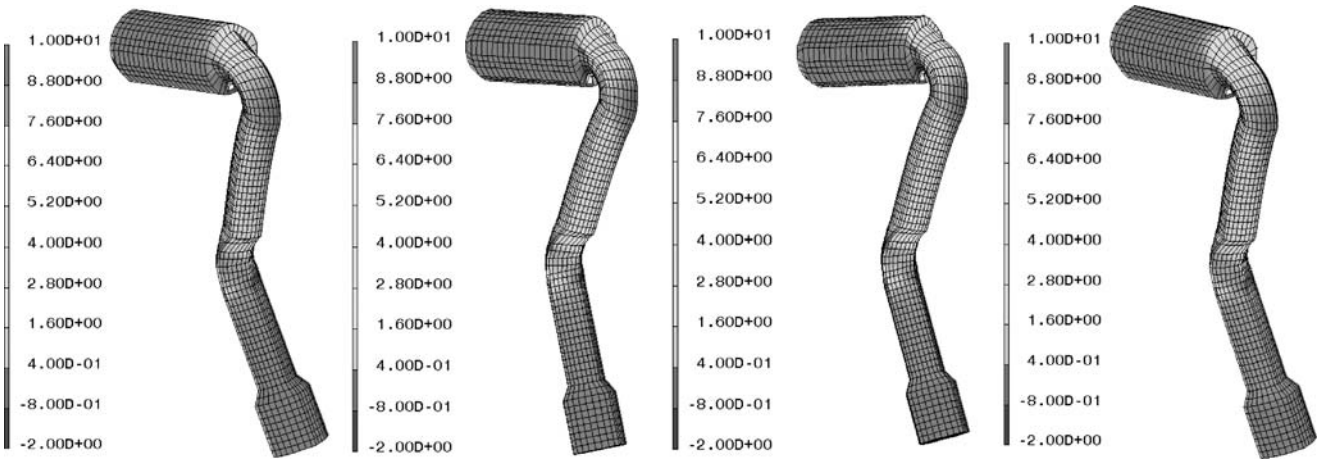

(a) 0 N (b) 20 N (c) 40 N (d) 60 N

Fig. 17 Maximal principal stresses in the ACL graft with different initial graft tensions [150]

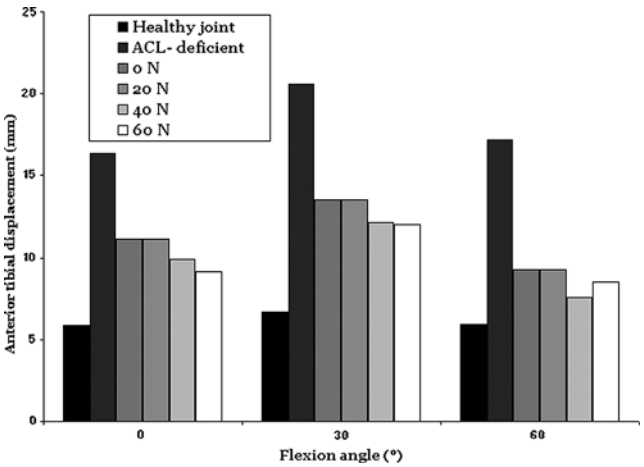

Fig. 18 Anterior tibial translation with different initial tensions during knee flexion [150]

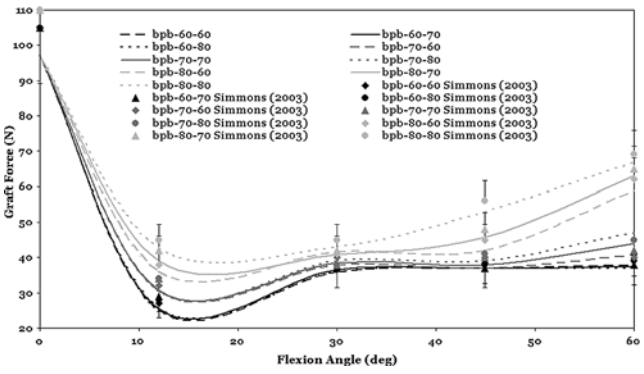

Fig. 19 Graft tension from 0° to 60° of flexion [144]

that ligaments have a uniform strain history and decrease relaxation of the initial stress in the graft [58]. Computational models can help to estimate the correct applied initial stress.

Table 3 PT viscoelastic material parameters [148]

γ_{11}	τ_{11} (s)	γ_{12}	τ_{12} (s)	γ_{14}	τ_{14}(s)
0.55	10	0.55	10	0.35	150

The viscoelastic parameters of the graft were obtained fitting the stress-curved obtained by Pioletti et al. [160] from the human patellar tendon (PT). These parameters are included in Table 3.

After fixation, the relaxation process of the graft was computed until thermodynamic equilibrium. Figure 21 shows the evolution of the initial prestress without and with previous cyclic load. The tension within the patellar tendon graft without cyclic load decreased a 32.5% and with cyclic load only 24.1%. This results is in agreement with clinical results [58].

4.2 Temporomandibular Joint

4.2.1 Anatomical Description of the Temporomandibular Joint

The TMJ is one of the most frequently used joints in the body, allowing us to talk, chew, yawn, swallow and sneeze and it is susceptible to all the problems that affect other joints in the body, including ankylosis, arthritis, trauma, dislocations, developmental anomalies and neoplasms.

The temporomandibular joint (TMJ) is a gliding joint, formed by the condyle of the mandible and the squamous portion of the temporal bone. The temporomandibular joint (TMJ) enables the frictionless movement between the temporal bone and the mandible. The articular surface of the temporal bone consists of a convex articular eminence anteriorly and a concave articular fossa posteriorly. The articular surface of the mandible consists of the top of the condyle.

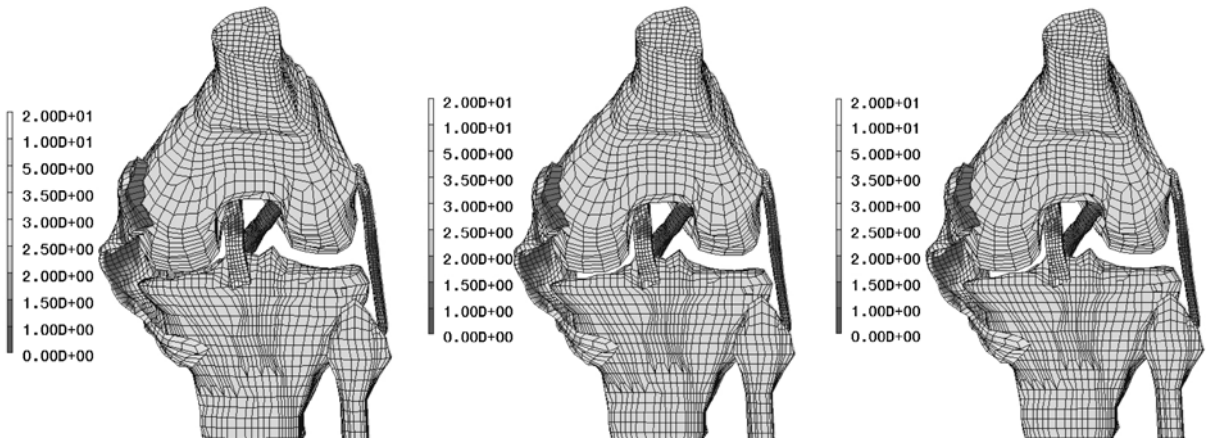

(a) 60-70 (b) 70-80 (c) 80-60

Fig. 20 Maximal principal stresses in the knee joint (MPa). The first and second numbers mean femoral and tibial angle respectively [144]

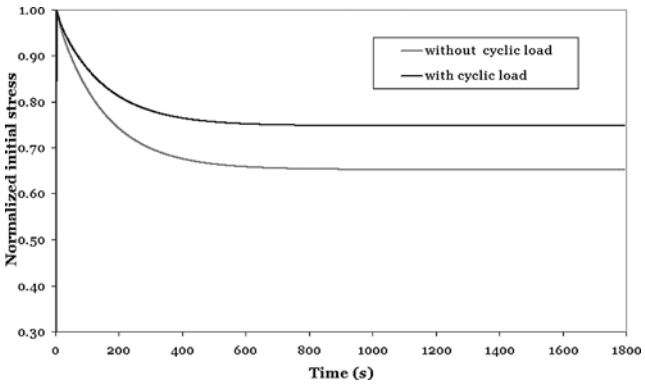

Fig. 21 Normalized initial stress evolution in the graft tendon with and without cyclic load [148]

Articular surfaces of the mandible and temporal bone are separated by an articular disk, which divides the joint cavity into two small spaces. Between the condylar process of the mandible and the glenoid fossa of the temporal bone, it lies an interposed fibrocartilaginous disc. It provides a stable platform for the rotational and gliding movements of the joint and also acts as a shock absorber [138] (Fig. 22).

The articular disk is a biconcave, fibrocartilaginous structure, which provides the gliding surface for the mandibular condyle, resulting in smooth joint movement. The disc has three parts: a thick anterior band, a thin intermediate zone, and a thick posterior band. In the closed position of the mouth, the condyle is separated from the articular fossa of the temporal bone by the thick posterior band, while in the mouth open position the condyle is separated from the articular eminence of the temporal bone by the thin intermediate zone. Thus, when we open the mouth, the rounded ends of the lower jaw, called condyles, glide along the joint socket of the temporal bone. The condyles slide back to their original position when we close our mouths (Fig. 22).

Fig. 22 Sagital section of the human temporomandibular joint. On the right a detail of the joint in open and closed mouth is depicted

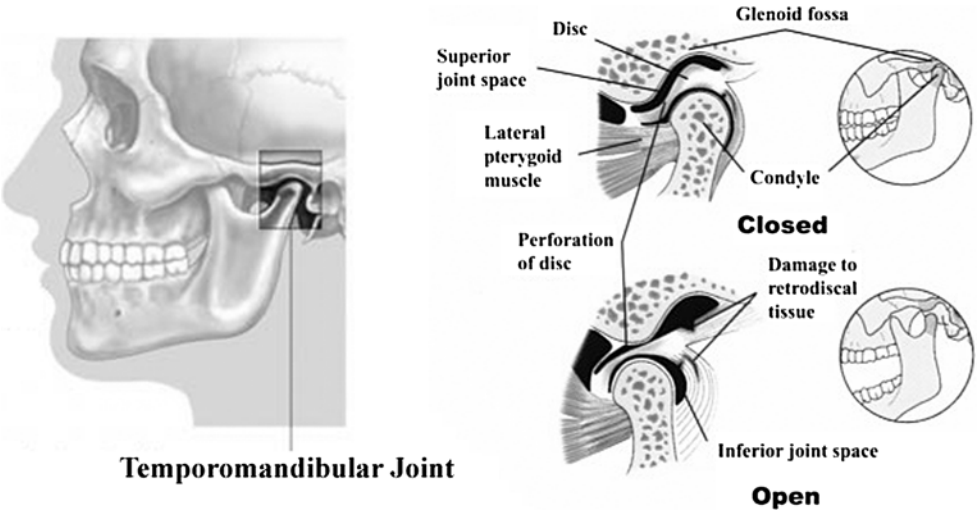

The mandible is held in position by a set of ligaments and muscles [66], and is connected to the temporal bone by an articular capsule reinforced with the lateral and medial ligaments. This capsule is very slack and thin, and it is composed of two types of fibers: long superficial fibers from the temporal bone to the mandible and short fibers that join the temporal bone to the discs and these to the condyles. The attachments of the discs to the condyles are tighter than those to the temporal bone. The lateral ligament which is thick and triangular, reinforces the lateral part of the capsule of the joint, and is stronger than the medial attachment [68]. Inside the joint capsule, located just behind the disc, there is a connective tissue known as retrodiscal tissue or bilaminar zone. It is composed partially of ligaments connecting the disk to the temporal bone and the condyle, but the primary composition is made up of a fairly loose, spongy material.

4.2.2 A Brief Review of Available Numerical Models of the Temporomandibular Joint

Many finite element (FE) analyses have been reported to probe the biomechanical status of the TMJ. The first finite element models were bidimensional [30, 38]. In these models the biomechanics of an oversimplified human TMJ was analyzed during the normal movement of the jaw, and although no reliable material properties were available for the different tissues, it was predicted that there was a nonlinear relationship between the maximal stresses that appeared in the tissues and the stiffness of the disc. Tanne et al. [192] measured elastic properties of dog articular discs, and they showed that the articular disc had a nonlinear stress-strain response in tension. The first three dimensional finite element model was constructed by Nagahara et al. [137]. In this model the authors analyzed the influence of the proper contact of the teeth to prevent disorders in the joint. Koolstra and van Eijden [103] developed a three dimensional model that included the masticatory muscles. Later, Beek et al. [14] reported that the stresses were located in the intermediate zone of the disc during clenching. The results of these studies suggested that the disc plays an important role in distributing and absorbing loads acting on the joint. The applied models, however, were (quasi-)static and, therefore, the applicability of their results is limited to situations where the jaw hardly moves (e.g., clenching) [16]. Posteriorly, Hu et al. [88] introduced in a simplified model of the joint, the fibrocartilaginous layers that cover the articulating surfaces of the joint, concluding that these prevent the disc and bone components from high stresses. Recently, Donzelli et al. [44] presented a 3D model of the joint, where the disc was considered as an isotropic poroelastic material. In their simulations a 5% opening of the joint was achieved without introducing a proper definition of the interfaces between cartilage and bones.

Biomechanical analyses of musculoskeletal system dynamics have been performed widely by applying rigid-body dynamics [7, 151]. This method, which basically transforms forces into movements, is very flexible and enables to investigate the influence of muscle activation on body movements. The distribution of forces in irregularly shaped joint structures, however, cannot be analyzed, and the deformations of articular cartilaginous layers cannot be taken into account. This method enables the prediction of the internal forces and deformations. The rigid body and FE method are supplementary [104].

The first model that took into account the presence of the collagen fibers inside the tissue, and the transversely isotropic character of the solid matrix was proposed by Pérez del Palomar and Doblaré [156], concluding that the introduction of collagen fibers in the biphasic behavior of the articular disc implies for a prescribed displacement not only an increase of the pressurization in the tissue, but also higher stresses in the anterior and posterior bands, as well as in the lateral zone of the disc. Thus, modelling the disc as an isotropic solid matrix leads in this case to an overestimation of the stresses in the intermediate zone, an underestimation of the pore pressure in this area, and an underestimation of the stresses in the rest of the disc. Following this idea, these authors also simulate the dynamically opening movement of the jaw [154] proposing different mechanisms of damage of the joint. However, they did not introduce the muscles in the joint.

4.2.3 Some Examples of Application

Description of the model In the following the model developed by Pérez del Palomar and Doblaré [154–156] is summarized. The geometrical model developed was built from NMR (Nuclear Magnetic Resonance) and CT (Computerized Tomography) images, which were obtained from an asymptomatic male subject aged 65. The contours of the cranium (temporal bone) and the mandible were obtained from the CT scan (Figs. 23a and 23b), while soft tissues contours were constructed from the NMR images (Fig. 23c). In this joint, bones were considered to be rigid also. Therefore, in order to create the rigid surfaces for the mandible and the

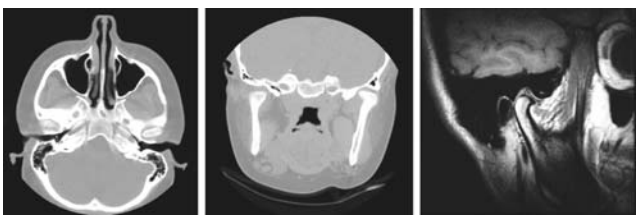

(a) Axial CT (b) Coronal CT (c) Sagittal NMR

Fig. 23 Computerized tomography and magnetic resonance images of the skull

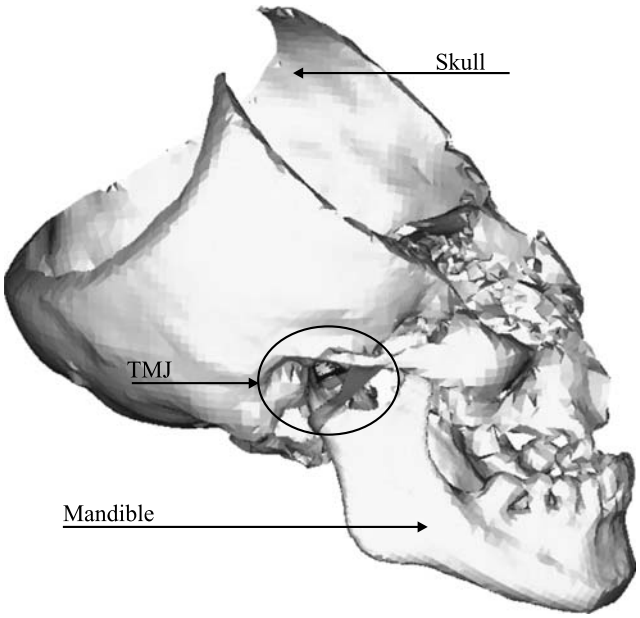

Fig. 24 Finite element model

temporal bone, a STL (Surface Tesselation) of these bone components was created and then meshed automatically in the commercial package I-DEAS v.9. The deformable parts of the joint, the articular disc and the ligaments were manually created. In order to generate the corresponding meshes, the contours of the different tissues were detected semiautomatically by means of a custom-design code, that allows the user to identify different components through a grey scale. These contours were approximated by splines, and then, these splines were used to construct the geometry and the finite element mesh of the disc and ligaments using eight-node brick elements in I-DEAS v.9.

The finite element model constructed includes therefore the mandible, the temporal bone, the two temporomandibular joints, the articular discs and the temporomandibular ligaments and is the first one that includes the ligaments and disc with a realistic geometry and properties. This model is shown in Fig. 24. The temporomandibular joint is detailed in Fig. 25, where the right condyle of the mandible, the temporal contact surface, the disc and collateral ligaments are shown.

The general-purpose finite element code ABAQUS v.6.4 [78] was used to simulate the problem, implementing appropriate user routines for the constitutive behavior of the material of the disc (see Sect. 3). The mechanical properties of the remaining materials were chosen from data available in literature [5, 174, 201].

The human disc has a biconcave profile in sections cut perpendicularly to its long axis. The thinner central part of the disc is designated as the intermediate zone, and the thickened rims are referred as the anterior and posterior bands respectively. In the thinner central region, the collagen bundles are preferentially oriented in an anteroposterior direction, while in the thicker more peripheral regions they run mediolaterally [174] (see Fig. 26a).

The presence of collagen in the articular disc must be taken into account when considering movement and distortion of the disc during normal jaw excursions [19]. Therefore, it is necessary to introduce a constitutive model for the disc that incorporates its biphasic nature and the anisotropy induced by collagen fibres (see Sect. 2.3.2).

The strain energy function chosen characterizing the hyperelastic behavior of the solid phase was earlier proposed by [84],

$$\Psi = C_1(\overline{I_1} - 3) + \frac{K_1}{2K_2}\left\{\exp\left[K_2(\overline{I_4} - 1)^2\right] - 1\right\} + \frac{1}{D}(J-1)^2 \tag{112}$$

where C_1 is the material constant related to the ground substance, $K_1 > 0$ and $K_2 > 0$ are the parameters which identify the exponential behavior due to the presence of collagen fibres, and D is the compressibility modulus.

The material constants have been obtained from a nonlinear fit of the experimental data reported by [174]. In that

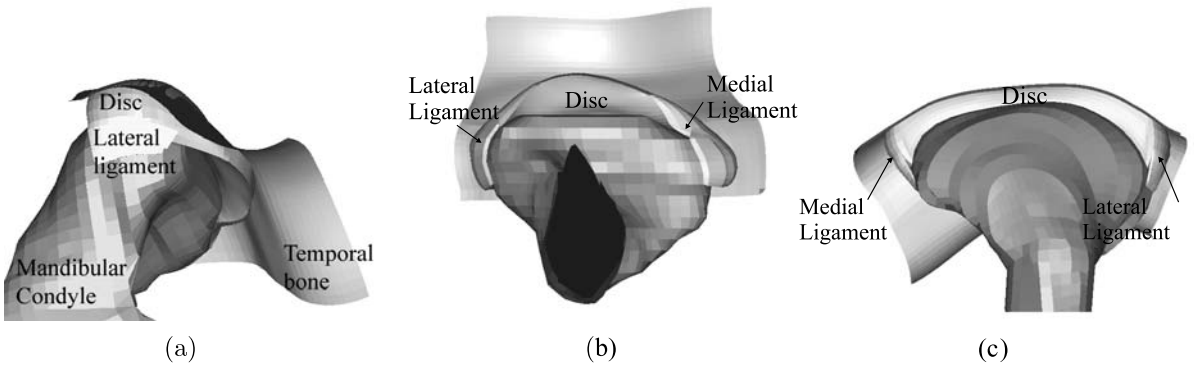

Fig. 25 Detail of the right temporomandibular joint. **a** Lateral view. **b** Inferior view. **c** Posterior view

work, Shengyi and coworkers performed tensile tests along the mediolateral direction of the disc on strips taken from the anterior and posterior bands, and from the middle zone. In this way, the isotropic behavior of the matrix can be characterized with the data obtained from the middle zone, since the fibres run perpendicularly to the axis of the test. On the other hand, the elastic constants related to the collagen fibres (the exponential term in (112)) can be obtained from the tests conducted on the tissue from the bands.

Figure 27 shows the experimental curves obtained by [174] and those obtained by the nonlinear fit of (112). It can be observed that within the 0% to 6% range, the theoretical curves are a sufficiently good fit of the experimental data. Although the exponential parameters of both bands are slightly different, the average of these values for both of them can be used. Table 4 depicts the elastic constants obtained from the nonlinear regression that have been used to define the behavior of the articular disc.

The disc has been divided in a number of element groups to which a particular fibre orientation was assigned (Fig. 26b). In this way the entire distribution of fibre orientation in the disc was covered in the numerical model.

The biphasic properties of the disc were obtained from literature [15]: an initial permeability of 7×510^{-15} m^4/N s and a solid volume fraction of 0.2. The hydraulic permeability is related to the amount of compaction the tissue experiences, which results in a decrease of apparent pore size. The permeability has been considered to present a non-linear dependence with the volumetric deformation [4, 188] (70), such as:

$$\kappa = \kappa_0 \cdot \left(\frac{J - \phi_0^s}{1 - \phi_0^s} \right)^L \cdot \exp\left(M \cdot \frac{J-1}{2} \right) \tag{113}$$

where κ_0 is the initial permeability, and M and L are material parameters that have been taken from [5] ($M = 4.638$ and $L = 0.0848$).

Since the interstitial fluid can leak out of the matrix when compressed, the whole disc surface was modelled with free drain boundary conditions. In this study, the fibrocartilage that covers the articulating surfaces of the condyle and the temporal bone were not included.

It is accepted that the temporomandibular ligaments constrain the motion of the mandible [171], not taking part in load transmission. Therefore, it is usually assumed that the articular surfaces, the ligaments, and the motion of the mandible induce the motion of the disc during the normal functioning of the joint [102, 141]. For the temporomandibular ligaments, a Neo-Hookean hyperelastic model with $C_1 = 6$ MPa [204] was used.

The contact between the different elements of the joint was introduced using the *contact pair option* in ABAQUS v.6.4 [78] which allows finite sliding. Ten contact pairs were defined in the model, including the interaction between the soft tissue and the rigid elements. The joint was also considered to be well lubricated, so a friction coefficient of 10^{-5} [190, 191] was considered.

Several movements can be considered to analyze the behaviour of this joint, however, one of the most complete is the opening movement of the jaw. In that paper, the results in

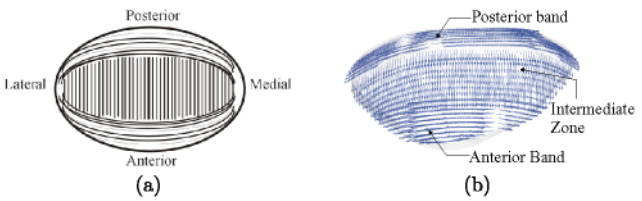

Fig. 26 **a** Schematic diagram of fibres distribution in the articular disc (viewed from top). **b** Collagen fibres distribution in the FE model

Table 4 Material constants of the hyperelastic behavior of the disc

C_1	0.770562 MPa
D	1.41 MPa^{-1}
K_1	0.6 MPa
K_2	79.8

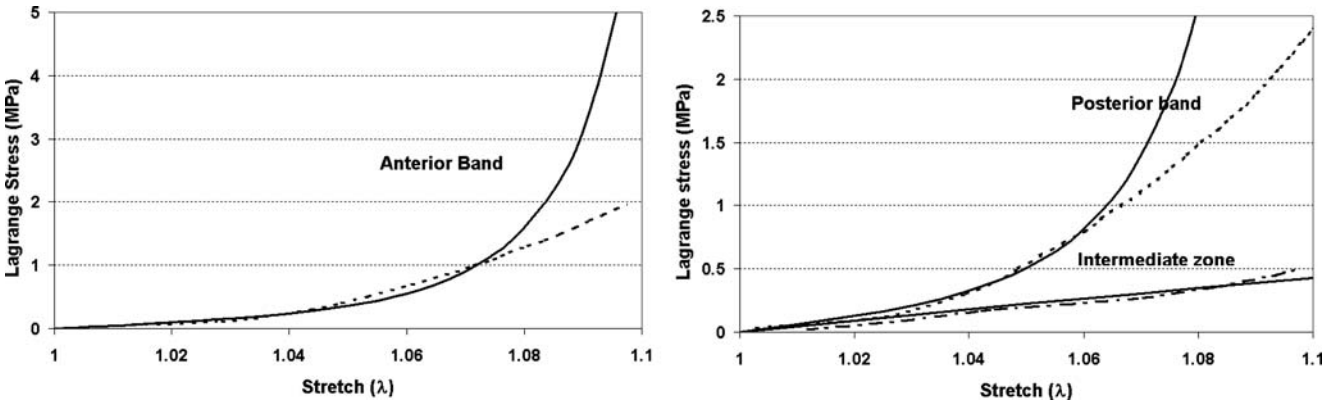

Fig. 27 Comparison of the experimental curves (*dotted lines*) [174] to the theoretical curves using Holzapfel strain energy function (*solid lines*)

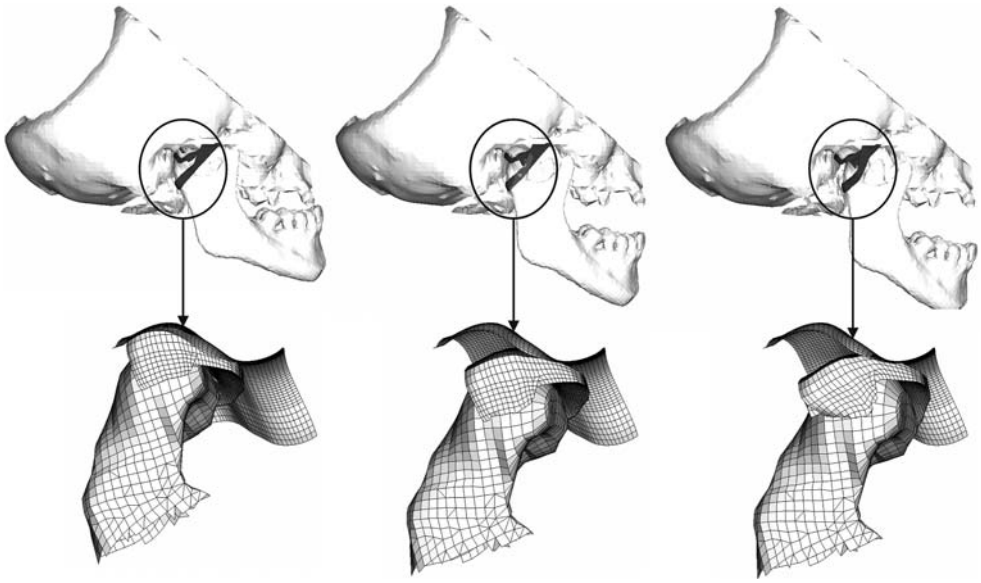

Fig. 28 Evolution of the opening movement of the jaw: Closed position (*left*), 10.5 mm opening (*middle*), 17.5 mm opening (*right*)

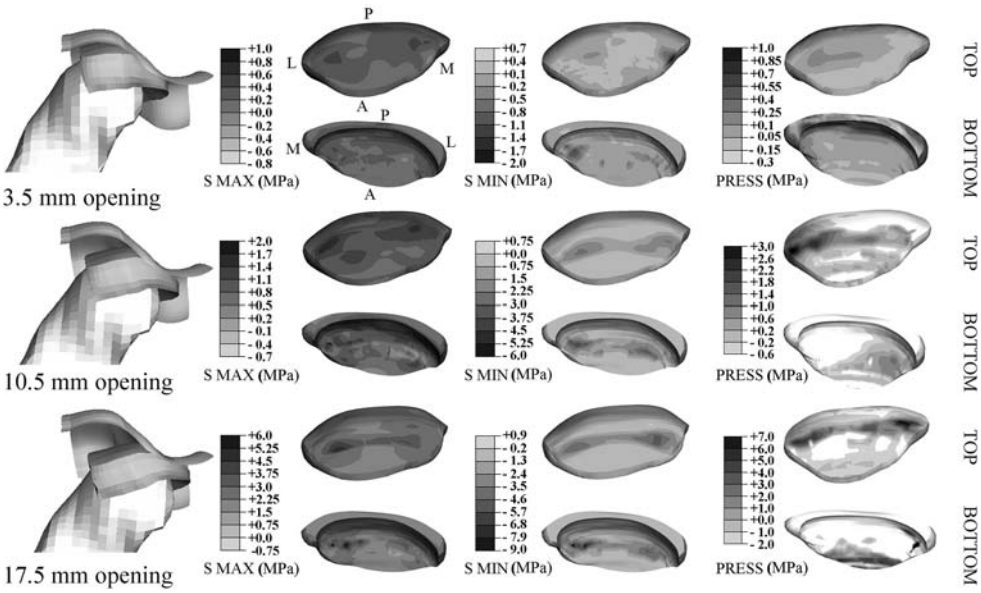

Fig. 29 Evolution of the maximum principal (*SMAX*), minimum principal (*SMIN*) stresses and pore pressure (*PRESS*) in the disc during the opening movement. Top and bottom surfaces of the disc are shown, with the following labels: *A* anterior, *P* Posterior, *L* Lateral and *M* Medial

a healthy, pathologic and reconstructed joint were presented for an opening movement of the jaw.

Healthy joint The displacements of the mandible were applied to a point located on the condyle. The trajectory of this point was obtained following the previous work of Chen et al. [29, 154]. The trajectory proposed by Chen was fit to the current FE model in order to obtain a physiological and smooth movement, obtaining a final mouth opening of 17.5 mm. The evolution of the opening movement is shown in Fig. 28 for different stages including a detail of the disc, the discal attachments and the condyle during the opening movement.

In Fig. 29, the maximum principal stresses (SMAX), the minimum principal stresses (SMIN) and the pore pressure (PRESS) in the articular disc for different opening degrees are shown. These results correspond to the right disc. It can be also appreciated that the disc moved with the condyle during the opening movement due to the collateral ligaments that hold the disc tightly to the mandible. At the beginning of the opening movement, higher stresses (SMAX) were found at the lateral and posterior parts of the disc, and the stress level increased with the progress of the opening movement. Compressive stresses (SMIN) were located in the intermediate zone of the disc during the movement, reaching a value of 8 MPa at its final stage. On the other hand, the introduction of a poroelastic model in the disc allowed to analyze the evolution of the pore pressure during the movement. Thus, it can be seen that the maximum pore pressure in the initial stage appeared in the central region of the disc, where it is

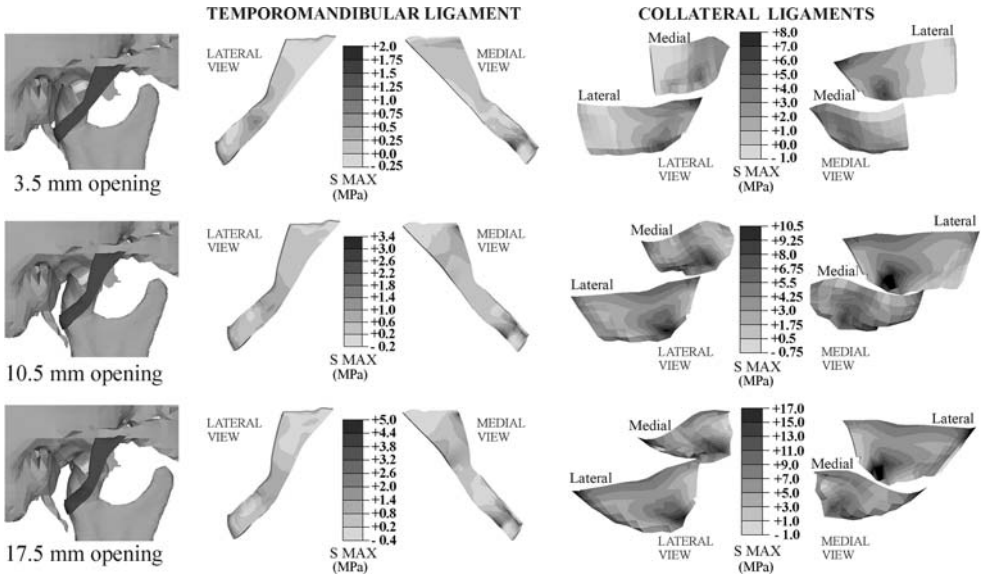

Fig. 30 Evolution of maximal principal stresses (*SMAX*) in the temporomandibular ligament and in the collateral ligaments during opening. These elements are shown in lateral and medial views

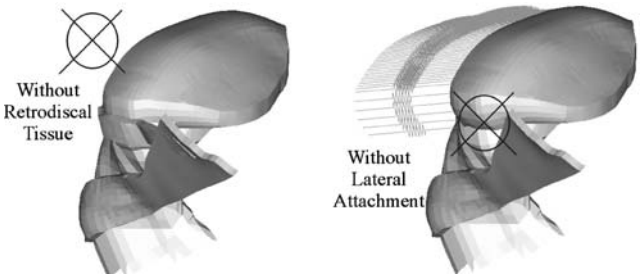

Fig. 31 Details of the two pathologic situations under study: on the *left*, disruption of the retrodiscal tissue; on the *right*, disruption of the lateral attachment of the disc to the condyle

compressed against the fossa. At the final stage, it can be observed that the maximum pore pressure was located in the lateral part of the intermediate zone on the bottom surface of the disc.

The evolution of the tensile stresses in the ligaments are shown in Fig. 30. It can be seen that the highest maximal principal stresses were located at its attachment point to the condyle (medial view), rising up to 5 MPa when the opening movement was completed. The tensile stresses were much higher in the collateral ligaments. These attach the disc to the condyle during all the different movements of the mandible, and are prone to failure in traumas [200]. In Fig. 30 the large distortion of these ligaments during movement can be appreciated. They result in higher stresses, with maximum around 20 MPa.

Injured joint It seems that one of the essential causes of disc disorders is the pathologic change in the ligamentous attachments of the disc-condyle complex [35, 162, 200]. According to statistics published in the Journal of American Dental Association in 1990, 44% to 99% of TMJ problems are caused by trauma [46]. This term comprises any impact to the head or mandible. Many traumatisms of the mandible come from impacts in the anteroposterior or lateral directions [200]. The impact force is transmitted to the skull through the TMJ and the surrounding ligaments. A trauma that comes from an anterior direction is likely to cause injury to the retrodiscal tissue, while one from a lateral direction will probably damage the lateral ligament insertions of the contralateral condyle.

In Fig. 32 a comparison between the stress response of the disc in the healthy and in a damaged joint affected of a bilaminar zone disruption is shown for a 10.5 mm opening. It can be observed that in this pathologic TMJ the compressive stresses (SMIN) moved posteriorly and the tensile stresses in the posterior band were lower than in the healthy one. The contact surface changed from the intermediate zone to the posterior band as well. Furthermore, higher stresses than in the healthy disc appeared in the medial zone of the disc, since it now moves both in the anterior and medial directions.

Another consequence of a head impact may result in injuries to the lateral discal attachment. In Fig. 33 the stresses undergone for the soft components in the healthy case and in the pathologic one without lateral attachments are compared for a 10.5 mm opening. It can be observed that the main effect of the lack of this ligament is that the lateral part of the disc is overstressed because this part of the disc tends to go up as the mandible moves. Therefore, both maximal and minimal principal stresses increased in that zone of the disc.

Pathologic joint The most common TMJ arthropathy is the internal derangement, which is characterized by a progressive anterior disc displacement. It is often associated with a capsulitis, making pain a common feature. It is a major TMJ disorder, accompanied with pain, clicking and/or

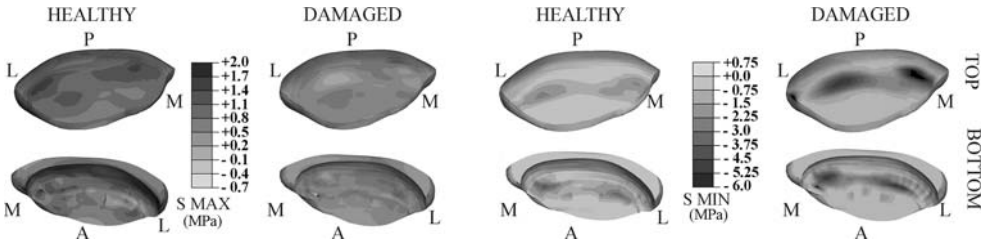

Fig. 32 Comparison of the maximal principal (*SMAX*) and minimal principal (*SMIN*) stresses in the disc between a healthy joint and one where the retrodiscal tissue has been removed (damaged)

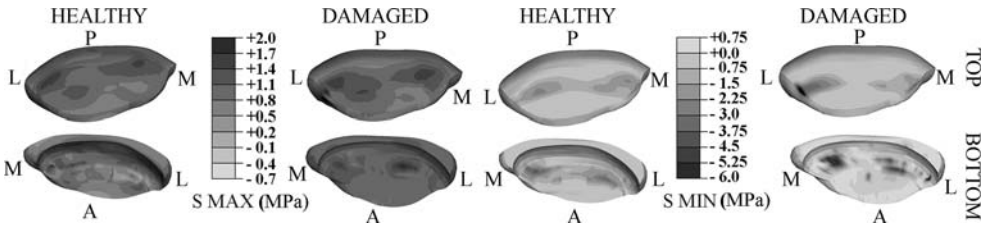

Fig. 33 Comparison of the maximal principal (*SMAX*) and minimal principal (*SMIN*) stresses in the disc between the healthy joint and one where the lateral attachment of the disc has been removed (damaged)

crepitus, muscle tenderness and limitation of mouth opening [139]. Displacement of the articular disc in the temporomandibular joint (TMJ) from its normal position was described and identified as a potential clinical problem more than a century ago [8]. Much emphasis has been placed on the damage caused by a displaced disc, however its origin and consequences are still unclear [139]. Theories and observations have been brought forward that would account for disc displacement as the cause of joint pain, limited mandibular movements, joint sounds, and osteoarthrotic changes in the TMJ [208]. These reports suggest that the disc protects the underlying tissues and that its displacement may expose these tissues to excessive loads with consequent degenerative changes [139]. What is clear is that the degenerative changes in the joint are influenced by the degree and the type of disc displacement. The more advanced the internal derangement, the more deteriorated the disc configuration [193]. Therefore, the biomechanical environment in the TMJ is a key to understand the inducing and progressive mechanism of temporomandibular disorders.

The anterior disc displacement has different degrees of severity. In an early stage, there is a simple displacement of the disc in the closed mouth position, usually anteriorly, due to weakness of the discal ligaments; this has been supported clinically [106, 162] and by finite element simulations [154]. When the subject opens the mouth, the disc takes again its normal position relative to the condyle: there is early clicking and the disc is said to be reduced early, due to the remaining elasticity of the bilaminar zone (the retrodiscal elastic ligament) and of the collateral ligaments; this is called anterior disc displacement with reduction (ADDWR) (Fig. 34). If this disorder becomes more severe the disc can not be reduced and then it adopts a displaced position during the movement. This case is called anterior disc displacement without reduction (ADDWOR).

The FE analysis was performed for an opening movement of the mouth for both pathologic cases (ADDWR and

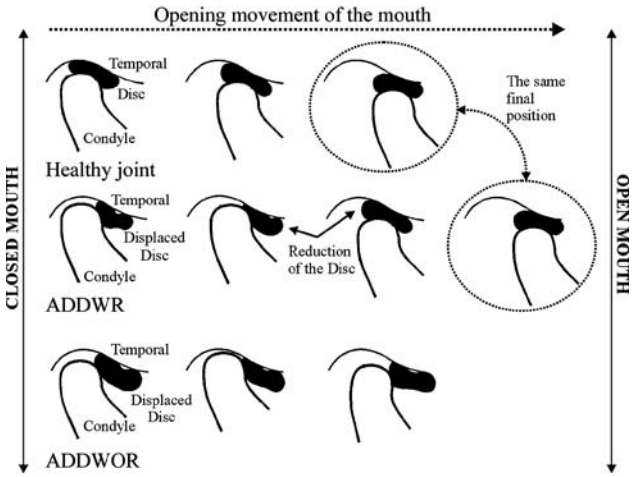

Fig. 34 Degree of anterior disc displacement simulated in this analysis; *Healthy*, *ADDWR*: anterior disc displacement with reduction, *ADDWOR*: anterior disc displacement without reduction

ADDWOR). In the case of reduction (ADDWR), the behaviour of the soft components of the joint can be analyzed before and after the recapturation of the disc.

The stress distribution that was obtained in each stage is shown in Fig. 35. It can be appreciated that before the recapture, the highest tensile stresses (SMAX) were located at both poles (lateral and medial) of the anterior band of the articular disc. The maximum compressive stresses in this stage, however, were located at the posterior band of the disc since it is compressed against the temporal surface when the condyle moves forward. At this position, the disc is reduced to its correct position on the condyle, and then the condyle and the disc move together over the articular eminence. In this stage, the maximum compressive stresses were located at the intermediate zone of the disc where it is compressed against the temporal bone. Thus, the maximum compressive stresses moved from the posterior band to the intermediate zone when the disc is reduced. However, it can be observed

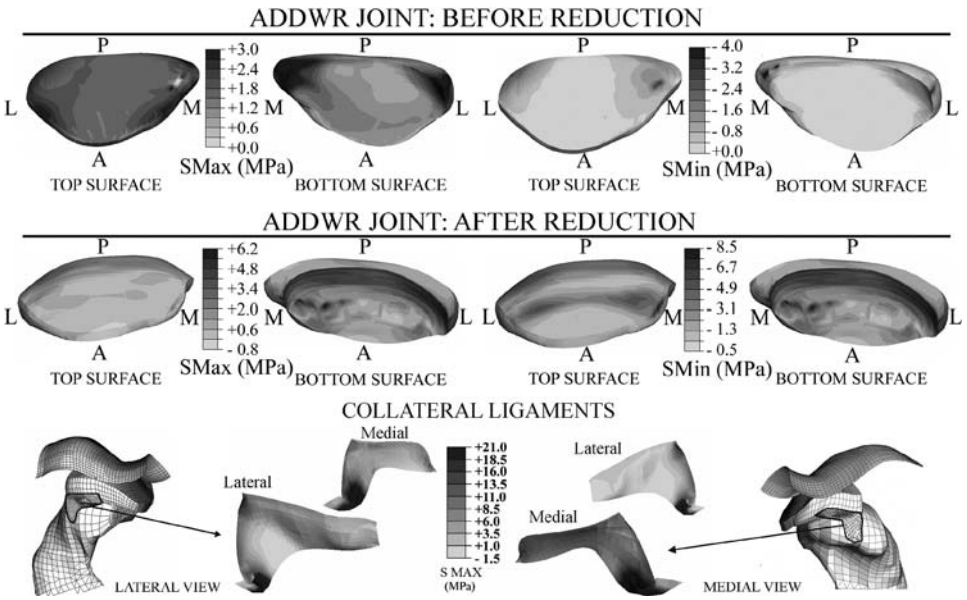

Fig. 35 Maximum Principal Stress (*SMAX*) and Minimum Principal Stress (*SMIN*) distribution in the disc during the opening movement in a TMJ with *ADDWR*. Tensile stresses in the collateral ligaments at the final state of the movement. Top and bottom surfaces of the disc are shown, with the following labels: *A* anterior, *P* Posterior, *L* Lateral and *M* Medial; Lateral and Medial Views are shown for the collateral ligaments

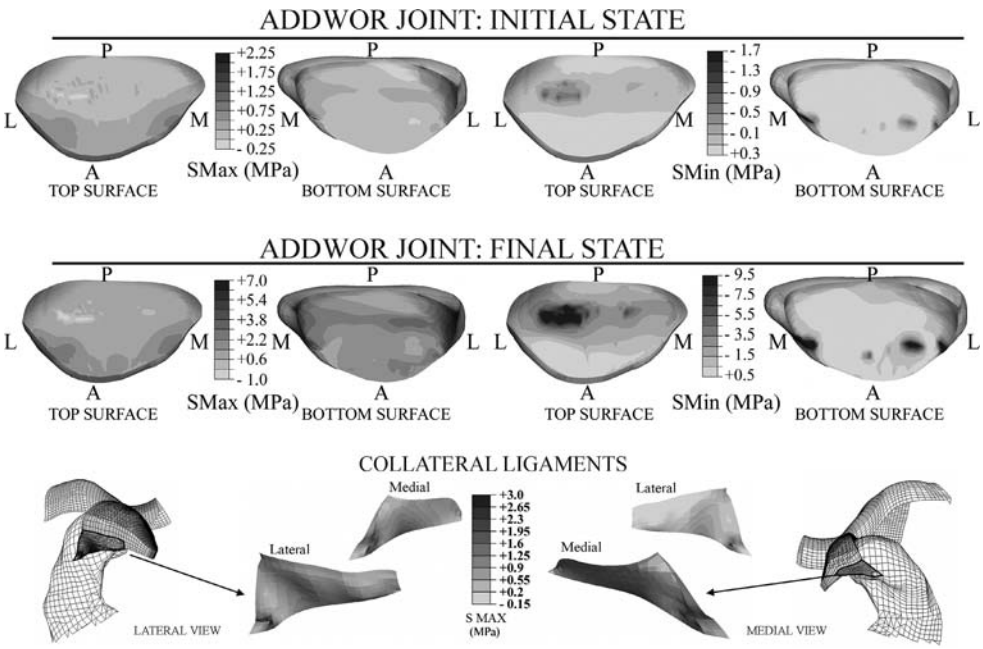

Fig. 36 Maximum Principal Stress (*SMAX*) and Minimum Principal Stress (*SMIN*) distribution in the disc during the opening movement in a TMJ with *ADDWOR* at intermediate and final states of the movement. Top and bottom surfaces of the disc are shown, with the following labels: *A* anterior, *P* Posterior, *L* Lateral and *M* Medial

that both before and after the recapture, there is a stress concentration in the lateral and medial poles of the disc. Besides, the behaviour of the collateral ligaments was also different in this case. The maximum value of the tensile stresses was twice as high as the value in the healthy joint.

The compressive and tensile stresses undergone by the articular disc in the ADDWOR are shown in Fig. 36. Now, during all the opening movement the maximum compressive stresses are located at the posterior band of the disc. In this case, as well as in the ADDWR one, stress concentrations appear in both poles of the disc. With regard to the response of the collateral ligaments, they were practically unloaded during the movement of the condyle because they were unable to reduce the disc to its physiological position.

Joint reconstruction Most symptomatic temporomandibular joint (TMJ) disorders are treated conservatively. However, about 5% of the patients need surgery. Although Annandale et al. [8] first described surgical repositioning of the displaced temporomandibular articular disc in 1887, it was not until Wilkes [207] used arthrography to describe the anatomy, form and function of the TMJ in 1978, that disc repositioning became an accepted surgical technique. The reported clinical results of surgical TMJ disc repositioning procedures (Fig. 37) have been variable and often

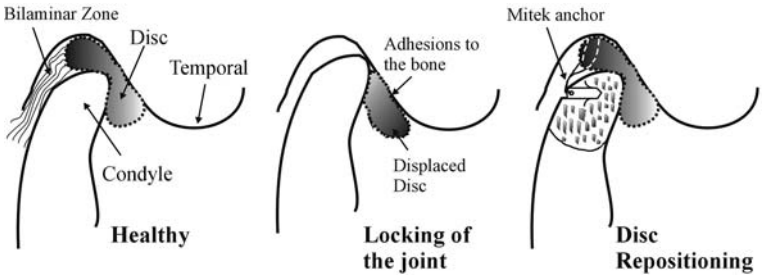

Fig. 37 A healthy joint with the disc located in its physiological position; locking of the joint with the disc permanently displaced; repositioning of the disc with a Mitek anchor to its physiological position

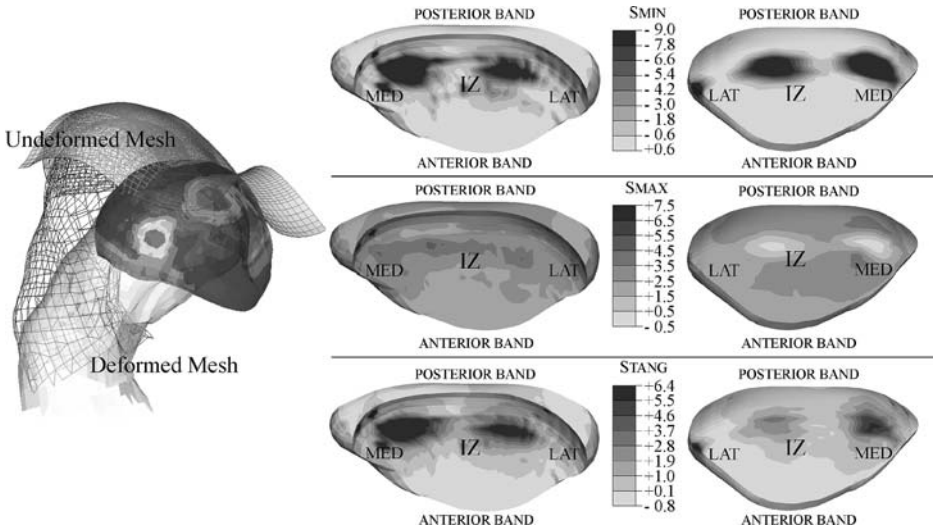

Fig. 38 Repositioning surgery. Compressive, tensile and tangential stresses (MPa) in the disc. *LAT*: lateral, *MED*: Medial, *IZ*: Intermediate Zone

unpredictable, with failures related to a lack of long term stability, indicating the need for improved methods of disc stabilization.

One of the most used techniques to reposition the disc consists in introducing a device to anchor it posteriorly to the condyle of the mandible. One of these devices is called MITEK anchor. It is composed of a titanium piece that is placed inside the condyle and is joined to the disc by means of two sutures. In [152], this system has been modelled with truss elements which represent the sutures attached to the condyle. As bones were considered rigid surfaces, the contribution of the MITEK anchor was neglected and therefore, the truss elements were attached to the condyle directly.

The distribution of stresses on the disc after surgery is shown in Fig. 38. It can be observed that the compressive stresses (SMIN) were located at the intermediate zone of the disc. Besides, the posterior band supported tensile stresses (SMAX) because the repositioning device pulls the disc posteriorly, an effect similar to the force exerted by the bilaminar zone in a healthy joint.

However, the artificial sutures modified the stresses in the posterior band of the disc. The sutures are tied to the disc in two points of the disc medially and laterally. This local application of the pulling forces provokes stress concentrations as shown in Fig. 39. There, a detail of the posterior band

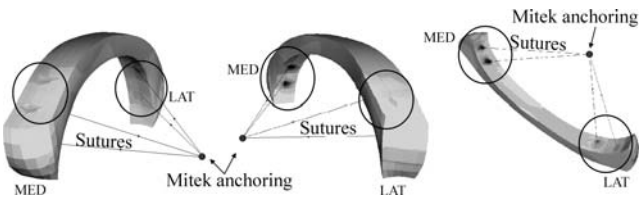

Fig. 39 Repositioning surgery. Stress concentrations around the artificial sutures in the posterior band of the repositioned disc

where the sutures are located is shown. These local concentrations could lead to perforations of the disc in the posterior band as has been detected clinically [213].

Therefore, the biomechanical response of the disc was quite similar in the repositioned joint compared to the healthy one, except for the appearance of local stress concentrations around the sutures that could damage those regions of the posterior band. This effect is also correlated with higher shear stresses in the posterior band in the joint after surgery.

5 Concluding Remarks

A review of the computational models developed to numerically analyzed diarthrodial joints such as the knee, and the

temporomandibular joint has been presented here. A detailed description of the main soft tissues involved, cartilage, ligaments and muscles has been presented. Also, a critical review of the constitutive models that have been developed to represent these tissues has been made. The application of these constitutive relationships in the context of joint modelling has also been reviewed.

The ultimate goal of these modelling efforts is to improve the clinical diagnosis and treatment of different injuries and disorders of diarthrodial joints. The models may also identify means by which to prevent injuries. Despite the significant advances in recent years in both the complexity and accuracy of computational models of soft tissues, current models are still incapable of completely describing and predicting joints behaviour. Improvement in future models will be achieved through research in a number of different areas, in particular, more experimental data, more accurate constitutive models, more precise geometrical models, and better muscles load values are needed.

Acknowledgement The authors gratefully acknowledge the support of the Spanish Education and Science Ministry (CYCIT DPI2003-09110-C02-01 and FIS2005-05020-C03-03) and the Spanish Ministry of Health through the National Network IM3 (Molecular and Multimodal Medical Imaging, Cardiovascular modelling, PI052006).

References

1. Abdel-Rahman E, Hefzy MS (1993) A two-dimensional dynamic anatomical model of the human knee joint. ASME J Biomech Eng 115:357–365
2. Akizuki S, Mow VC, Müller F, Pita JC, Howell DS, Manicourt DH (1986) Tensile properties of human knee joint cartilage: I. Influence of ionic conditions, weight bearing and fibrillation on the tensile modelus. J Orthopaed Res 4:379–392
3. Alastrue V, Calvo B, Peña E, Doblaré M (2006) Biomechanical modelling of refractive corneal surgery. ASME J Biomech Eng 128:150–160
4. Almeida ES, Spilker RL (1997) Mixed and penalty finite element models for the nonlinear behaviour of biphasic soft tissues in finite deformation: Part I alternate formulations. Comput Methods Appl Mech Eng 1:25–46
5. Almeida ES, Spilker RL (1997) Mixed and penalty finite element models for the nonlinear behaviour of biphasic soft tissues in finite deformation: Part II nonlinear examples. Comput Methods Appl Mech Eng 1:151–170
6. Almeida ES, Spilker RL (1998) Finite element formulations for hyperelastic transversely isotropic biphasic soft tissues. Comput Methods Appl Mech Eng 151:513–538
7. Anderson DM, Sinclair PM, McBride KM (1991) A clinical evaluation of temporomandibular joint disk plication surgery. Am J Orthod Dentofac Orthop 100
8. Annandale T (1887) On displacement of intraarticular cartilage of the lower jaw and its treatment by operation. Lancet 1:411–412
9. Arms S, Boyle J, Johnson R, Pope M (1995) Strain in the medial collateral ligament of the human knee: an autopsy study. J Biomech 29:199–206
10. Armstrong CG, Lai WM, Mow VC (1984) An analisysis of the unconfined compression of articular cartilage. ASME J Biomech Eng 106:165–173
11. Au AG, Raso VJ, Liggins AB, Otto DD, Amirfazli A (2005) A three-dimensional finite element stress analysis for the tunnel placement and buttons in anterior cruciate ligament reconstructions. J Biomech 38:827–832
12. Bach JM, Hull ML (1998) Strain inhomogeneity in the anterior cruciate ligament under application of external and muscular loads. ASME J Biomech Eng 120:497–503
13. Barbenel JC, Evans JH, Finlay JB (1973) Stress-strain-time relations for soft connective tissues. In: Kenedi (ed) Perspectives biomed eng. McMillan, New York, pp 165–172
14. Beek M, Koolstra JH, van Ruijven LJ, van Eijden TMGJ (2000) Three-dimensional finite element analysis of the human temporomandibular joint disc. J Biomech 33:307–316
15. Beek M, Koolstra JH, van Eijden TMGJ (2003) Human temporomandibular joint disc cartilage as a poroelastic material. Clin Biomech 18:69–76
16. Beek M, Koolstra JH, van Ruijven LJ, van Eijden TMGJ (2001) Three-dimensional finite element analysis of the cartilaginous structures in the human temporomandibular joint. J Dent Res 80:1913–1918
17. Bendjaballah MZ, Shirazi-adl A, Zukor DJ (1995) Biomechanics of the human knee joint in compression: reconstruction, mesh generation and finite element analysis. Knee 2:69–79
18. Bendjaballah MZ, Shirazi-adl A, Zukor DJ (1998) Biomechanical response of the passive human knee joint under anterior-posterior forces. Clin Biomech 13:625–633
19. Berkovitz BKB (2000) Collagen crimping in the intra-articular disc and articular surfaces of the human temporomandibular joint. Arch Oral Biol 45:749–756
20. Beynnon B, Yu J, Huston D, Fleming B, Johnson R, Haugh L, Pope M (1996) A sagittal plane model of the knee and cruciate ligaments with application of a sensitivity analysis. ASME J Biomech Eng 118:227–239
21. Papadrakakis M, Topping BHV (eds) (1994) Advances in nonlinear finite element methods. Civil-Comp Ltd
22. Blankevoort L, Huiskes R (1991) Ligament-bone interaction in a three-dimensional model of the knee. ASME J Biomech Eng 113:263–269
23. Buschmann MD, Grodzinsky AJ (1995) A molecular model of proteoglycan-associated electrostatic forces in cartilage mechanics. ASME J Biomech Eng 117:179–192
24. Butler DL, Sheh MY, Stouffer DC, Samaranayake VA, Levy MS (1990) Surface strain variation in human patellar tendon and knee cruciate ligaments. ASME J Biomech Eng 39:38–45
25. Carter DR, Hayes WC (1977) The compressive behavior of bone as a two-phase porous structure. J Bone Joint Surg 59:954–962
26. Carter DR, Wong M (1988) The role of mechanical loading histories in the development od diarthrodial joints. J Orthopaed Res 6:804–816
27. Chan SC, Seedhom BB (1995) The effect of the geometry of the tibia on prediction of the cruciate ligament forces: a theoretical analysis. J Eng Med 209:17–30
28. Chaudhry HR, Bukiet, B, Davis A, Ritter AB, Findley T (1997) Residual stress in oscillating thoracic arteries reduce circumferential stresses and stress gradient. J Biomech 30:57–62
29. Chen J, Buckwalter K (1993) Displacement analysis of the temporomandibular condyle from magnetic resonance images. J Biomech 26:1455–1462
30. Chen J, Xu L (1994) A finite element analysis of the human temporomandibular joint. ASME J Biomech Eng 116:401–407
31. Chen Y, Chen X, Hisada T (2006) Non-linear finite element analysis of mechanical electrochemical phenomena in hydrated soft tissues based on triphasic theory. Int J Numer Methods Eng 65:147–173
32. Cohen B, Gardner TR, Ateshian GA (1993) The influence of transverse isotropy on cartilage indentation behaviour: a study of the human humeral head. Trans Orthopaed Res Soc 39:185

33. Cohen B, Lai WM, Chorney GS, Dick HM, Mow VV (1992) Unconfined compression of transversely isotropic biphasic tissues. Trans ASME 22:207–219
34. Coletti JM, Akeson WH, Woo SLY (1972) A comparison of the physical behavior of normal articular cartilage and the arthroplasty surface. J Bone Joint Surg 54A:147–160
35. Cooper B, Oberdorfer M, Rumpf D, Malakhova O, Rudman R, Mariotti A (1999) Trauma modifies strength and composition of retrodiscal tissues of the goat temporomandibular joint. Oral Dis 5(4):329–336
36. Cowin SC, Hegedus DH (1976) Bone remodeling: a theory od adaptative elasticity. J Elasticity 6:313–326
37. Currey JD (2002) Bones. Structure and mechanics. Princeton University Press, Princeton
38. DeVocht JW, Goel VK, Zeitler DL, Lew DA (1996) A study of the control of disc movement within the temporomandibular joint using the finite element technique. J Oral Maxil Surg 54:1431
39. Doblaré M, Cueto E, Calvo B, Martínez MA, García JM, Cegoñino J (2005) On the employ of meshless methods in biomechanics. Comput Methods Appl Mech Eng 194:801–821
40. Doblaré M, Cueto E, Calvo B, Martínez MA, García JM, Peña E (2004) Computational bioengineering. Current trends and applications. In: An analysis of the performance of meshless methods in biomechanics. Imperial College Press, London, pp 69–100
41. Doblaré M, García JM (2001) Application of an anisotropic bone-remodeling model based on a damage-repair theory to the analysis of the proximal femur before and after total hip replacement. J Biomech 34(9):1157–1170
42. Doblaré M, García JM (2002) Anisotropic bone remodelling model based on a continuum damage-repair theory. J Biomech 35:1–17
43. Haut Donahue TL, Hull ML, Rashid MM, Jacobs RC (2002) A finite element model of the human knee joint for the study of tibiofemoral contact. ASME J Biomech Eng 124:273–280
44. Donzelli PS, Gallo LM, Spilker RL, Palla S (2004) Biphasic finite element simulation of the TMJ disc from in vivo kinematic and geometric measurements. J Biomech 37(11):1787–1791
45. Donzelli PS, Spilker RS, Ateshian GA, Van Mow C (1999) Contact analysis of biphasic transversely isotropic cartilage layers and correlation with tissue failure. J Biomech 32:1037–1047
46. Dworkin, SF, Huggins KH, LeResche L, VonKorff M, Howard J, Truelove E, Sommers E (1990) Epidemiology of signs and symptoms in temporomandibular disorders: clinical signs in cases and controls. J Am Dent Assoc 120(3):273–281
47. Eberhardt AW, Lewis JL, Keer LM (1991) Contact layered elastic spheres as a model of joint contact: effect of tangential load and friction. ASME J Biomech Eng 113:107–108
48. Van Eijden TM, Kouwenhoven E, Verbug J, Weijs WA (1986) A mathematical model of the patellofemoral joint. J Biomech 19:219–229
49. Eisenberg SR, Grodzinsky AJ (1985) Swelling of articular cartilage and other connective tissues: electromechanochemical forces. J Orthopaed Res 3:148–159
50. Elmore SM, Sokoloff L, Norris G, Carmeci P (1963) Nature of imperfect elasticity of articular cartilage. J Appl Physiol 18:393–396
51. Essinger JR, Leyvraz PF, Heegaard JH, Robertson DD (1989) A mathematical model for the evaluation of the behavior during flexion of condylar-type knee prostheses. J Biomech 22:1229–1241
52. Fithian DC, Kelly MA, Van Mow C (1990) Material properties and structure-function relationship in the menisci. Clin Orthop Relat R 252:19–31
53. Fletcher R (2001) Practical methods of optimization. Wiley
54. Flory PJ (1961) Thermodynamic relations for high elastic materials. Trans Faraday Soc 57:829–838
55. Fortin M, Glowinski R (1983) Augmented Lagrangian methods: application to the numerical solution of boundary value problems, volume 15. North Holland, Amsterdam
56. Fox RJ, Harner CD, Sakane M, Carlin GJ, Woo SL-Y (1998) Determination of the in situ forces in the human posterior cruciate ligament using robotic technology. Am J Spors Med 26:395–401
57. Frank CB, Jackson DW (1997) Reconstruction of the anterior cruciate ligament. J Bone Joint Surg 79-A:1556–1576
58. Fu FH, Harner C, Vince KG (1994) Knee surgery. Willians and Wilkins, Baltimore
59. Fung YC (1973) Biorheology of soft tissues. Biorheol 10:139–155
60. Fung YC (1993) Biomechanics. Mechanical properties of living tissues. Springer
61. Gabriel MG, Wong EK, Woo SL-Y, Yagi M, Debski RE (2004) Distribution of in situ forces in the anterior cruciate ligament in response to rotatory loads. J Orthopaed Res 22:85–89
62. Gardiner JC, Weiss JA (2003) Subject-specific finite element analysis of the human medial collateral ligament during valgus knee loading. J Orthopaed Res 21:1098–1106
63. Gardiner JC, Weiss JA, Rosenberg TD (2001) Strain in the human medial collateral ligament during valgus lading of the knee. Clin Orthop Relat R 391:266–274
64. Garikipati K, Arruda EM, Grosh K, Narayanan H, Calve S (2004) A continuum treatment of growth in biological tissue: the coupling of mass transport and mechanics. J Mech Phys Solids 52(7):1595–1625
65. Glowinski R, LeTallec P (1989) Augmented Lagrangian and operator-splitting methods in nonlinear mechanics. SIAM Studies in Applied Mathematics, Philadelphia
66. Gray H (1998) Gray's Anatomy: The anatomical basis of medicine and surgery, volume 1, 38 edn. Harcourt
67. Grodzinsky AJ (1973) Electromechanical and physicochemical properties of connective tissue. Crit Rev Biomed Eng 9:133–199
68. Rouviere H, Delmas A (1985) Anatomie humaine, volume 1. Masson
69. Harfe DT, Chuinard CR, Espinoza LM, Thomas KA, Solomonow M (1998) Elongation patterns of the collateral ligamnets of the human knee. Clin Biomech 13:163–175
70. Harner CD, Giffin R, Dunteman RC, Annunziata CC, Friedman MJ (2000) Evaluation and treatment of recurrent instability after anterior cruciate ligament reconstruction. J Bone Joint Surg 82-A:1652–1663
71. Hayes WC, Mockros LF (1971) Viscoelastic constitutive relations for human articular cartilage. J Appl Physiol 18:562–568
72. Heegard J, Leyvraz PF, Curnier A, Rakotomana L, Huiskes R (1995) The biomechanics of the human patella during passive knee flexion. J Biomech 28:1265–1279
73. Hefzy MS, Grood ES (1988) Review of knee models. Appl Mech Rev 41:1–13
74. Hefzy MS, Grood ES (1993) An analytical technique for modelling knee joint stiffness—Part II: Ligamentous geometric nonlinearities. ASME J Biomech Eng 105:143–145
75. Hefzy MS, Yang H (1993) Three-dimensional anatomical model of the human patello-femoral joint to determine patellofemoralmotions and contact characteristics. ASME J Biomech Eng 15:289–302
76. Hernandez CK, Beaupre GS, Keller TS, Carter DR (2001) The influence of bone volume fraction and this fraction on bone strength and modulus. Bone 29(1):74–78
77. Herrmann LR, Peterson FE (1968) A numerical procedure for viscoelastic stress analysis. In: Proceedings of the seventh meeting of ICRPG mechanical behaviour working group, Orlando, 1968
78. Hibbit, Karlsson, Sorensen, Inc (2003) Abaqus user's manual, v. 6.4. HKS inc. Pawtucket, RI, USA

79. Hill AV (1938) The heat of shortening and the dynamic constans of muscle. Proc Roy Soc Lond B 126:136–195
80. Hirokawa S, Tsuruno R (1997) Hyperelastic model analysis of anterior cruciate ligament. Med Eng Phys 19:637–651
81. Hirokawa S, Tsuruno R (2000) Three-dimensional deformation and stress distribution in an analytical/computational model of the anterior cruciate ligament. J Biomech 33:1069–1077
82. Hirsch C (1944) A contribution to the pathogenesis chondromalacia of the patella. Acta Chir Scand 90:1–106
83. Holmes MH (1986) Finite deformation of soft tissue: analysis of a mixture model in uni-axial compression. ASME J Biomech Eng 108:372–381
84. Holzapfel GA (2000) Nonlinear solid mechanics. Wiley, New York
85. Holzapfel GA, Gasser TC, Ogden RW (2000) A new constitutive framework for arterial wall mechanics and a comparative study of material models. J Elasticity 61:1–48
86. Holzapfel GA, Gasser TC (2001) A viscoelastic model for fiber-reinforced composites at finite strains: continuum basis, computational aspects and applications. Comput Methods Appl Mech Eng 190:4379–4403
87. Holzapfel GA, Gasser TC, Stadler M (2002) A structural model for the viscoelastic behaviour of arterial walls: continuum formulation and finite element analysis. Eur J Mech A/Solid 21:441–463
88. Hu K, Qiguo R, Fang J, Mao JJ (2003) Effects of condylar fibrocartilage on the biomechanical loading of the human temporomandibular joint in a three-dimensional, nonlinear finite element model. Med Eng Phys 25:107–113
89. Huberti HH, Hayes WC (1984) Patellofemoral contact pressures. J Bone Joint Surg 66-A:715–724
90. Hughes TJR (2000) The finite element method: linear static and dynamic finite analysis. Dover, New York
91. Hull ML, Berns GS, Varma H, Patterson A (1995) Strain in the medial collateral ligament of the human knee under single and combined loads. J Biomech 29:199–206
92. Humphrey JD (2002) Continuum biomechanics of soft biological tissues. Proc Roy Soc Lond A 175:1–44
93. Huxley AF (1957) Muscle structure and theories of contraction. Prog Biophys Biophysic Chem 173:257–318
94. Jackson JP (1968) Degenerative changes in the knee after meniscectomy. Br Med J 2:525
95. Jacobs CR (1994) Numerical simulation of bone adaption to mechanical loading. PhD thesis, Stanford University, Stanford, California
96. Jalani A, Shirazi-adl A, Bendjaballah MZ (1997) Biomechanics of human tibio-femoral joint in axial rotation. Knee 4:203–213
97. Jurvelin JS, Arokoski JP, Hunziker EB (1997) Optical and mechanical determination of Poisson's ratio of adult bovine articular cartilage. J Biomech 33:235–241
98. Kastelic J, Galeski A (1978) The multicomposite structure of tendon. J Connect Tissue R 6:11–23
99. Kempson GE, Freeman MAR, Swanson SA (1971) The determination of a creep modulus for articular cartilage form indentation tests on the human femoral head. J Biomech 4:239–250
100. Keyac JH (2001) Improved prediction of proximal femoral fracture load using nonlinear finite element models. Med Eng Phys 23:165–173
101. Khalsa PS, Eisenberg SR (1997) Compressive behavior of articular cartilage is not completely explained by proteoglycan osmotic pressure. J Biomech 30:589–594
102. Koolstra JH, van Eijden TMGJ (1995) Biomechanical analysis of Jaw-closing movements. J Dent Res 74:1564–1570
103. Koolstra JH, van Eijden TMGJ (1999) Three-dimensional dynamical capabilities of the human masticatory muscles. J Biomech 32:145–152
104. Koolstra JH, van Eijden TMGJ (2004) Functional significance of the coupling between head and jaw movements. J Biomech 37:1387–1392
105. Korhonen RM, Laasanen MS, Töyräs J, Lappalainen R, Helminen HJ, Jurvelin JS (2003) Fibril reinforced poroelastic model predicts specifically mechanical behavior of normal proteoglycan depleted and collagen degraded articular cartilage. J Biomech 36:1373–1379
106. Kurita H, Ohtsuka A, Kobayashi H, Kurashina K (2001) Resorption of the lateral pole of the mandibular condyle in temporomandibular disc displacement. Dentomaxillofac Rad 30:88–91
107. Lai WM, Mow VC, Roth V (1986) Effects of a nonlinear strain-dependent permeability and rate of compression on the stress behavior of articular cartilage. ASME J Biomech Eng 108:123–130
108. Lanir Y (1979) A structural theory for the homogeneous biaxial stress-strain relationship in flat collageneous tissues. J Biomech 12:423–436
109. Lanir Y (1983) Constitutive equations for fibrous connective tissues. J Biomech 16:1–12
110. LeRoux MA, Setton LA (2002) Experimental and biphasic FEM determinations of the material properties and hydraulic permeability of the meniscus in tension. ASME J Biomech Eng 124:315–321
111. Lewis JL, Lew WD, Hill JA, Hanley P, Ohland K, Kirstukas S, Hunter RE (1989) Knee joint motion and ligament forces before and after ACL reconstruction. ASME J Biomech Eng 111:97–106
112. Li G, Gil J, Kanamori A, Woo SL (1999) A validated three-dimensional computational model of a human joint. ASME J Biomech Eng 121:657–662
113. Li G, Lopez O, Rubash H (2001) Variability of a three-dimensional finite element model constructed using magnetic resonance images of a knee for joint contact stress analysis. ASME J Biomech Eng 123:341–346
114. Limbert G, Middleton J (2004) A tranversely isotropic viscohyperelastic material. Application to the modeling of biological soft connective tissues. Int J Solids Struct 41:4237–4260
115. Limbert G, Middleton J, Taylor M (2004) Finite element analysis of the human ACL subjected to passive anterior tibial loads. Comput Methods Biomech Biomed Eng 7:1–8
116. Linn FC, Sokoloff L (1965) Movement and composition of interstitial fluid of cartilage. Arthritis Rheum 8:481–494
117. Van Loocke M, Lyons CG, Simms C (2004) Stress-strain-time relations for soft connective tissues. In: Prendergast PJ, McHugh PE (eds) Topics in bio-mechanical engineering. Trinity centre for bioengineering & National Centre for Biomedical Engineering Science, pp 216–234
118. Lotz JC, Gerhart TN, Hayes WC (1991) Mechanical properties of metaphyseal bone in the proximal femur. J Biomech 24:317–329
119. Li LP, Bushmann MD, Shirazi-Adl A (2000) A fibril reinforced nonhomogeneous poroelastic model for articular cartilage: inhomogeneous response in unconfined compression. J Biomech 33:1533–1541
120. Li LP, Soulhat J, Bushmann MD, Shirazi-Adl A (1999) Nonlinear analysis of cartilage in unconfined ramp compression using a fibril reinforced poroelastic model. Clin Biomech 14:673–682
121. Luenberger DE (1989) Programacion lineal y no lineal. Addison-Wesley Iberoamericana
122. Macnicol MF, Thomas NP (2000) The knee after menisctomy. J Bone Joint Surg 82-B:157–159
123. Mak A (1986) The apparent viscoelastic behaviour of articular cartilage. The contributions from the intrinsic matrix viscoelastocity and intersticial fluid flows. ASME J Biomech Eng 108:123–130
124. Maroudas A (1976) Balance between swelling pressures and collagen tension in normal and degenerate cartilage. Nature 260:808–809

125. Marsden JE, Hughes TJR (1994) Mathematical foundations of elasticity. Dover, New York
126. Martins JAC, Pires EB, Salvado R, Dinis PB (1998) A numerical model of passive and active behavior of skeletal muscles. Comput Methods Appl Mech Eng 151:419–433
127. Matthews LS, Sonstegard DA, Henke JA (1977) Load bearing characteristics of the patello-femoral joint. Acta Orthop Scand 48:511–516
128. Moeinzadeh M-H, Engin AE, Akkas N (1983) Two-dimensional dynamic modelling of human knee joint. J Biomech 16:253–264
129. Mogo KE, Shirazi-Adl A (2004) Cruciate coupling and screw-home mechanics in passive knee joint during extension-flexion. J Biomech (in press)
130. Mow CV, Kuei SC, Lai WM, Amstrong CG (1980) Biphasic creep and stress relaxation of articular cartilage in compression: theory and experiments. ASME J Biomech Eng 102:73–84
131. Mow VC, Holmes MH, Lai WM (1984) Fluid transport and mechanical properties of articular cartilage: a review. J Biomech 17:377–394
132. Mow VC, Kwan MK, Lai WM, Armstrong CG (1985) A finite deformation theory for nonlinearity permeable soft hydrated biological tissues. In: Frontiers in biomechanics. Springer
133. Mow VC, Guo XE (2003) Mechano-electrochemical properties of articular cartilage: their inhomogeneities and anisotropies. Annu Rev Biomed Eng 4:175–209
134. Mow VC, Ratcliffe A (1997) Structure and function of articular cartilage and meniscus, 2nd edn. Lippincott-Raven, Philadelphia, pp 113–177
135. Mow VC, Soslowsky LJ (1991) Basic orthopeadics biomechanics. In: Friction, lubrication and wear of diarthrodial joints. Raven Press, New York, pp 245–292
136. Murakami T (1990) The lubrication in natural synovial joints and joint protheses. JSME Int J Vib Sys 33:465–474
137. Nagahara K, Murata S, Nakamura S, Tsuchiya T (1999) Displacement and stress distribution in the temporomandibular joint during clenching. Angle Orthod 69:372
138. Nickel JC, McLachlan KR (1994) In vivo measurement of the frictional properties of the temporomandibular joint disc. Arch Oral Biol 39(4)
139. Nitzan DW (2001) The process of lubrication impairment and its involvement in temporomandibular joint disc displacement: a theoretical concept. J Oral Maxil Surg 59:36–45
140. Oomens CWJ, Maenhout M, van Oijen CH, Drost MR, Baaijens FP (2003) Finite element modelling of contracting skeletal muscle. Phil Trans Roy Soc Lond B 358:1453–1460
141. Osborn JW (1993) A model to describe how ligaments may control symmetrical jaw opening movements in man. J Oral Rehabil 20:585–604
142. Park S, Krishnan R, Nicoll SB, Ateshian GA (2003) Cartilage interstitial fluid support in unconfined compression. J Biomech 36:1785–1796
143. Parsons JR, Black J (1977) The viscoelastic shear behavior of normal Rabbit Articular Cartilage. J Biomech 10:21–29
144. Peña E, Calvo B, Martinez MA, Palanca D, Doblaré M (2006) Influence of the tunnel angle in acl reconstructions on the biomechanics of the knee joint. Clin Biomech 21(5):508–516
145. Peña E, Calvo B, Martinez MA, Doblaré M (2006) A three-dimensional finite element analysis of the combined behavior of ligaments and menisci in the healthy human knee joint. J Biomech 39:1686–1701
146. Peña E, Calvo B, Martinez MA, Palanca D, Doblaré M (2005) Finite element analysis of the effect of meniscal tears and meniscectomy on human knee biomechanics. Clin Biomech 20:498–507
147. Peña E, Calvo B, Martinez MA, Palanca D, Doblaré M (2006) Why lateral meniscectomy is more dangerous than medial meniscectomy? a finite element study. J Orthopaed Res 24:1001–1010
148. Peña E, Calvo B, Martínez MA, Doblaré M (2007) An anisotropic visco-hyperelastic model for ligaments at finite strains: formulation and computational aspects. Int J Solid Struct 44:760–778
149. Peña E, Martinez MA, Calvo B, Doblaré M (2006) On the numerical treatment of initial strains in soft biological tissues. Int J Numer Meth Eng 68:836–860
150. Peña E, Martinez MA, Calvo B, Palanca D, Doblaré M (2005) A finite element simulation of the effect of graft stiffness and graft tensioning in ACL reconstruction. Clin Biomech 20:636–644
151. Peck C, Langenbach GEJ, Hannam AG (2000) Dynamic simulation of muscle and articular properties during human wide jaw opening. Arch Oral Biol 45:963–982
152. Pérez-Palomar A (2004) Three dimensional finite element simulation of the temporomandibular joint. PhD thesis, University of Zaragoza, Spain (in Spanish)
153. Pérez-Palomar A, Doblaré M (2006) On the numerical simulation of the mechanical behaviour of articular cartilage. Int J Numer Meth Eng 67:1244–1271
154. Pérez-Palomar A, Doblaré M (2006) 3D Finite Element simulation of the opening movement of the mandible in healthy and pathologic situations. ASME J Biomech Eng 128:242–249
155. Pérez-Palomar A, Doblaré M (2006) Finite Element Analysis of the Temporomandibular Joint during lateral excursions of the mandible. J Biomech 39:1244–1271
156. Pérez-Palomar A, Doblaré M (2006) The effect of collagen reinforcement in the behaviour of the temporomandibular joint disc. J Biomech 39:1075–1085
157. Pioletti D (1997) Viscoelastic properties of soft tissues. PhD thesis, The University of Lausanne
158. Pioletti DP, Rakotomanana L (2000) Finite element model of the anterior cruciate ligament. Eur J Mech A/Solids 19:749–759
159. Pioletti DP, Rakotomanana L, Leyvraz PF, Benvenuti JF (1997) Finite element model of the anterior cruciate ligament. Comput Methods Biomech Biomed Eng
160. Pioletti DP, Rakotomanana LR, Benvenuti J-F, Leyvraz P-F (1998) Viscoelastic constitutive law in large deformations: application to human knee ligaments and tendons. J Biomech 31:753–757
161. Powell MJD (1969) Optimization. In: A method for nonlinear constraints in minimization problems. Academic, New York, pp 283–298
162. Prater ME, Bailey BJ, and Quinn FB (1998) Temporomandibular joint disorders. The University of Texas Medical Branch
163. Périé D, Hobatho MC (1998) In vivo determination of contact areas and pressure of the femorotibial joint using non-linear finite element analysis. Clin Biomech 13:394–402
164. Puso MA, Weiss JA (1998) Finite element implementation of anisotropic quasilinear viscoelasticity. ASME J Biomech Eng 120:162–170
165. Puxkandl R, Zizak I, Paris O, Tesch W, Bernstorff S, Purslow P, Fratzll P (2002) Viscoelastic properties of collagen: synchrotron radiation investigations and structural model. Phil Trans Roy Soc Lond B 357:191–197
166. Rachev A, Hayashi K (1999) Theoretical study of the effects of vascular smooth muscle contraction on strain and stress distributions in arteries. Ann Biomed Eng 27(4):459–468
167. Raminaraka NA, Terrier A, Theumann N, Siegrist O (2005) Effects of the posterior cruciate ligament reconstruction on the biomechanics of the knee joint: a finite element analysis. Clin Biomech 20:434–442
168. Sanjeevi RA (1982) A viscoelastic model for the mechanical properties of biological materials. J Biomech 15:107–109
169. Sasaki N, Odajima S (1996) Stress-strain curve and Young's modulus of a collagen molecule as determined by X-ray diffraction technique. J Biomech 29:655–658

170. Sathasivam S, Walker PS (1997) A computer model with surface friction for the prediction of total knee kinematics. J Biomech 30:177–184
171. Sato H, Ström D, Carlsson GE (1995) Controversies on anatomy and function of the ligaments associated with the temporomandibular joint: a literature survey. J Orofac Pain 9:308–316
172. Scheller G, Sobau C, Bülow JU (2001) Arthroscopic partial lateral meniscectomy in an otherwise normal knee: clinical, functional and radiographic results of a long-term follow-up study. Arthrosc 17:946–952
173. Setton L, Elliott DM, Mow VC (1999) Altered mechanics of cartilage with osteoarthritis: human osteoarthritis and an experimental model of joint degeneration. Osteoarthr Cartilage 7:2–14
174. Shengyi T, Yinghua X (1991) Biomechanical properties and collagen fiber orientation of TMJ discs in dogs: Part I. Gross anatomy and collagen fiber orientation of the discs. J Craniomandib Disord 5:28–34
175. Simmons R, Howell S, Hull ML (2003) Effect of angle of the femoral and tibial tunnels in the coronal plane and incremental excision of the posterior cruciate ligament on tension of an anterior cruciate ligament graft: an in vitro study. J Bone Joint Surg 85-A:1018–1029
176. Simo JC (1987) On a fully three-dimensional finite-strain viscoelastic damage model: Formulation and computational aspects. Comput Methods Appl Mech Eng 60:153–173
177. Simo JC, Hughes TJR (1998) Computational inelasticity. Springer, New York
178. Simo JC, Taylor RL (1985) Consistent tangent operators for rate-independent elastoplasticity. Comput Methods Appl Mech Eng 48:101–118
179. Simo JC, Taylor RL (1991) Quasi-incompresible finite elasticity in principal stretches. Continuum basis and numerical algorithms. Comput Methods Appl Mech Eng 85:273–310
180. Simo JC, Taylor RL, Pister KS (1985) Variational and projection methods for the volume constraint in finite deformation elastoplasticity. Comput Methods Appl Mech Eng 51:177–208
181. Simo JC, Taylor R (1991) Quasi-incompressible finite elasticity in principal stretches. Continuum basis and numerical algorithm. Comput Methods Appl Mech Eng 85(3)
182. Sokoloff L (1963) Elasticity of articular cartilage: effect of ions and viscous solutions. Sci 141:1055–1056
183. Song Y, Debski RE, Musahl V, Thomas M, Woo SL-Y (2004) A three-dimensional finite element model of the human anterior cruciate ligament: a computational analysis with experimental validation. J Biomech 37:383–390
184. Soulhat J, Buschman MD, Shirazi-Adl A (1999) A fibril-network reinforced biphasic model of cartilage in unconfined compression. ASME J Biomech Eng 121:340–347
185. Spencer AJM (1954) Theory of invariants. In: Continuum physics. Academic, New York, pp 239–253
186. Spilker RL, Suh JK (1990) Formulation and evaluation of a finite element model for the biphasic model of hydrated soft tissue. Comput Struct 35(4):425–439
187. Suggs J, Wang C, Li G (2003) The effect of graft stiffnes on knee joint biomechanics after ACL reconstruction: a 3D computational simulation. Clin Biomech 18:35–43
188. Suh JK, Spilker RL, Holmes MR (1991) A penalty finite element analysis for non-linear mechanics of biphasic hydrated soft tissue under large deformation. Int J Numer Methods Eng 32:1411–1439
189. Suh JK, Bai S (1997) Biphasic poroviscoelastic behavior of cartilage in creep indentation test. In: Transactions 43rd annual meeting of the orthopaedic research society, San Francisco, 1997
190. Tanaka E, Rodrigo P, Tanaka M, Kawaguchi A, Shibazaji T, Tanne K (2001) Stress analysis in the TMJ during jaw opening by use of a three dimensional finite element model based on magnetic resonance images. Int J Oral Maxil Surg 30:421–430
191. Tanaka E, Tanne K, Sakuda MA (1994) A three dimensional finite element model of the mandible including the TMJ and its application to stress analysis in the TMJ during clenching. Med Eng Phys 16:316–322
192. Tanne K, Tanaka E, Sakuda M (1991) The elastic modulus of the temporomandibular joint disc from adult dogs. J Dent Res 70:1545
193. Taskaya-Yilmaz N, Ogutcen-Toller M (2001) Magnetic resonance imaging evaluation of temporomandibular joint disc deformities in relation to type of disc displacement. J Oral Maxil Surg 59:860–865
194. Timoshenko S, Goodier JN (1972) Teoría de la elasticidad. Editorial Urmo
195. Mow VC, Hayes WC (1991) Basic orthopaedic biomechanics. Raven Press, New York
196. Vedi V, Williams A, Tennant SJ, Spouse E (1999) Meniscal movement. J Bone Joint Surg 81-B:37–41
197. De Vita R, Slaughter WS (2005) A structural constitutive model for the strain rate-dependent behavior of anterior cruciate ligaments. Int J Solids Struct (in press)
198. Vose GP, Kubala AL (1959) Bone strength, its relationship to x-ray-determined ash content. Human Biol 31:261–270
199. Walker PS, Erkman MJ (1975) The role of the menisci in force transmission across the knee. Clin Orthop Relat R 109:184–192
200. Weinberg S, Lapointe, H (1987) Cervical extension-flexion injury (whiplash) and internal derangement of the temporomandibular joint. J Oral Maxil Surg 45(8):653–656
201. Weiss J, Gardiner JC (2001) Computational modelling of ligament mechanics. Crit Rev Biomed Eng 29:1–70
202. Weiss J, Gardiner JC, Bonifasi-Lista C (2002) Ligament material behavior is nonlinear, viscoelastic and rate-independent under shear loading. J Biomech 35:943–950
203. Weiss JA, Gardiner JC, Ellis BJ, Lujan TJ, Phatak NS (2005) Three-dimensional finite element modeling of ligaments: technical aspects. Med Eng Phys 27:845–861
204. Weiss JA, Maker BN, Govindjee S (1996) Finite element implementation of incompressible, transversely isotropic hyperelasticity. Comput Methods Appl Mech Eng 135:107–128
205. Weiss JA, Maker BN, Schauer DA (1995) Treatment of initial stress in hyperelastic finite element models of soft tissues. In: Beaver Creek CO (ed) ASME summer bioengineering conference, 1995
206. Weiss JA, Maker BN, Govindjee S (1996) Finite element implementation of incompressible, transversely isotropic hyperelasticity. Comput Methods Appl Mech Eng 135:107–128
207. Wilkes CH (1978) Arthrography of the temporomandibular joint in patients with the TMJ pain-dysfunction syndrome. Minn Med 61(11):645–652
208. Wilkes CH (1978) Structural and functional alterations of the temporomandibular joint. Northwest Dent 57(5):287–294
209. Wilson W, van Donkelaar CC, van Rietbergen B, Huiskes R (2003) Pathways of load-induced cartilage damage causing degeneration in the knee after meniscectomy. J Biomech 36:845–851
210. Winters JM (1990) Hill-based muscle models: a system engineering perspective. In: Winters JM, Woo S (eds) Multyple muscle system. Springer, New York, pp 165–172
211. Woo SL, Lubock P, Gómez MA, Jemmott G, Kuei SC, Akeson WH (1979) Large deformation nonhomogeneous and directional properties of articular cartilage in uniaxial tension. J Biomech 12:437–446
212. Wriggers P (1995) Finite element algorithms for contact problems. Arch Comput Methods Eng 2:1–49
213. Yasunaga T, Kimura M, Kikuchi S (2001) Histologic change of the meniscus and cartilage tissue after meniscal suture. Clin Orthop Relat R 387:232–240

214. Yoshiya M, Kurosaka M, Yamada M (1991) Optimal orientation of bone tunnels in the anterior cruciate ligament reconstruction. Trand ORS 16:602
215. Zahalak GI (1981) A distributed moment approximation for kinetic theories of muscular contraction. Math Biosci 55:89–114
216. Zahalak GI, Ma SP (1990) Muscle activation and contraction: constitutive relations based on cross-bridge kinetics. ASME J Biomech Eng 112:52–62
217. Zajac FE (1989) Muscle and tendon: properties, models, scaling and application ti biomechanics and motor control. Crit Rev Biomed Eng 17:359–411
218. Zienkiewicz OC, Taylor RL (1994) The finite element method, volume 1: basic formulation and linear problems. McGraw-Hill